Karlsruhe Institute of Technology

Christian Kern

On the Hall effect in three-dimensional metamaterials

2019
Dissertation

On the Hall effect in three-dimensional metamaterials

Zur Erlangung des akademischen Grades eines
DOKTORS DER NATURWISSENSCHAFTEN
von der KIT-Fakultät für Physik des
Karlsruher Instituts für Technologie (KIT)

genehmigte

DISSERTATION

von

MSc ETH Christian Frederik Kern
geboren in Stuttgart

Tag der mündlichen Prüfung: 8. Februar 2019
Referent: Prof. Dr. Martin Wegener
Korreferent: Prof. Dr. Jörg Schmalian

Contents

Publications

Parts of this thesis have already been published ...
... in scientific journals:

- M. Kadic, R. Schittny, T. Bückmann, C. Kern, and M. Wegener, "Hall-Effect Sign Inversion in a Realizable 3D Metamaterial", *Phys. Rev. X* **5**, 021030 (2015)
- C. Kern, M. Kadic, and M. Wegener, "Parallel Hall effect from three-dimensional single-component metamaterials", *Appl. Phys. Lett.* **107**, 132103 (2015)
- C. Kern, M. Kadic, and M. Wegener, "Experimental Evidence for Sign Reversal of the Hall Coefficient in Three-Dimensional Metamaterials", *Phys. Rev. Lett.* **118**, 016601 (2017)
- C. Kern, V. Schuster, M. Kadic, and M. Wegener, "Experiments on the Parallel Hall Effect in Three-Dimensional Metamaterials", *Phys. Rev. Applied* **7**, 044001 (2017)
- M. Wegener, M. Kadic, and C. Kern, "Hall-effect metamaterials and 'anti-Hall bars'", *Phys. Today* **70**, Issue 10, 14 (2017)
- M. Briane, M. Kadic, C. Kern, G. W. Milton, M. Wegener, and D. Whyte, "Surprises Regarding the Hall Effect: An Extraordinary Story Involving an Artist, Mathematicians, and Physicists", *SIAM Newsjournal* **7**, Issue 10, 1 (2017)
- C. Kern, M. Kadic, M. Wegener, "Kern, Kadic, and Wegener Reply", Reply to a comment by J. Oswald on "Experimental Evidence for Sign Reversal of the Hall Coefficient in Three-Dimensional Metamaterials", *Phys. Rev. Lett.* **120**, 149702 (2018)

- C. Kern, G. W. Milton, M. Kadic, and M. Wegener, "Theory of the Hall effect in three-dimensional metamaterials", *New J. Phys.* **20**, 083034 (2018)
- C. Kern and M. Wegener, "Three-dimensional metamaterial Hall-bar devices", *Phys. Rev. Mater.* **3**, 015204 (2019)

. . . at scientific conferences (only own presentations):

- C. Kern, M. Kadic, and M. Wegener, "Sign reversal of the Hall coefficient in three-dimensional metamaterials" (invited talk), Auxetics 2016, Szymbark, Poland, September 2016
- C. Kern, M. Kadic, G. W. Milton, and M. Wegener, "The Hall effect in composites" (key speaker), ETOPIM11, Krakow, Poland, July 2018
- C. Kern, M. Kadic, and M. Wegener, G. W. Milton, "Hall Effect Metamaterials" (invited talk), Metamaterials 2018, Espoo, Finland, August 2018
- C. Kern, G. W. Milton, M. Kadic, and M. Wegener, "On the integration and characterization of chainmail-inspired Hall effect metamaterials", Metamaterials 2018, Espoo, Finland, August 2018

ADDITIONAL RELATED WORK HAS ALREADY BEEN PUBLISHED . . .
. . . in scientific journals:

- K. Edelmann, L. Gerhard, M. Winkler, L. Wilmes, V. Rai, M. Schumann, C. Kern, M. Meyer, M. Wegener, and W. Wulfhekel, "Light collection from a low-temperature scanning tunneling microscope using integrated mirror tips fabricated by direct laser writing", *Rev. Sci. Instrum.* **89**, 123107 (2018)
- S. Mannherz, A. Niemeyer, F. Mayer, C. Kern, and M. Wegener, "On the limits of laminates in diffusive optics", *Opt. Express* **26**, 34274 (2018)

Chapter 1

1 Introduction

In his 1879 paper on what we today know as the Hall effect [1], or more precisely, the classical Hall effect, Edwin Hall quotes a passage of Maxwell's famous treatise on electricity and magnetism [2]. There, Maxwell states that, "It must be carefully remembered, that the mechanical force which urges a conductor carrying a current across the lines of magnetic force, acts, not on the electric current, but on the conductor which carries it."

Contrary to Maxwell's statement, Hall was able to show that a magnetic field directly affects the current rather than the conductor carrying it [1, 3]. In his experiments, Hall studied samples made from rectangular metal platelets. He imposed an electric current using a battery and a magnetic field using an electromagnet. Using a galvanometer, he was able to measure a transversal voltage, which we today refer to as the Hall voltage.

According to the modern textbook explanation, the effect is caused by the action of the Lorentz force on the charge carriers that leads to a charge accumulation and an opposing electric field, the so-called Hall electric field. The voltage corresponding to this electric field is the Hall voltage, which is proportional to the imposed current and the magnetic induction and inversely proportional to the thickness of the sample. The proportionality constant is the so-called Hall coefficient.

Today, sensors based on the Hall effect are regularly used to measure magnetic fields. Such Hall sensors are employed in many devices that we use in our everyday lives. Most commonly, they are used in combination with a permanent magnet for a variety of sensing applications [4]. In smartphones, they are used to determine whether a flip cover is closed. In every modern car, Hall sensors are employed, for example, in order to measure rotational

speeds [5] or to determine whether a seat belt buckle is latched [6].

A different application of the Hall effect is its use in the characterization of semiconductors. In bulk semiconductors, the sign of the Hall coefficient and, hence, the sign of the Hall voltage is given by the sign of the charge carriers. Therefore, by measuring the Hall voltage, one can identify the predominant type of charge carriers. It turn out that this statement is false if one considers a more general class of materials, so-called metamaterials. For a certain type of structures that were inspired by medieval chainmail, the sign of the effective Hall coefficient is not identical to the sign of the charge carriers.

In general, metamaterials are finely structured materials that are composed of several constituent materials and that, on a larger length scale, effectively act like homogeneous materials with properties that go beyond those of the constituent materials. Their effective properties are determined by their microscopic structure and, therefore, can be tailored to specific needs. Usually, the microscopic structure is a periodic arrangement of certain building blocks very much like a conventional crystal is a periodic arrangement of atoms. Metamaterials vastly extend our set of available material properties. Furthermore, using metamaterials, it is possible to realize a wide variety of effective material properties starting from a relatively small set of constituent materials.

In this thesis, I am studying how one can use three-dimensional metamaterials to tailor the effective conductivity in the limit of weak magnetic fields. I am referring to such metamaterials as Hall metamaterials. As it turns out, very unusual effective properties can be realized. A prime example is the sign-inversion of the effective Hall coefficient mentioned above. Moreover, I will show that it is possible to realize any arbitrary effective Hall coefficient using a single-constituent porous metamaterial. Very interesting effects appear in the anisotropic case. For example, certain anisotropic metamaterials exhibit the parallel Hall effect. In such metamaterials, the Hall electric field is parallel rather than perpendicular to the external magnetic field.

In general, one can show that the influence of a weak magnetic field on the behavior of a conductive material is described by a rank-two tensor, the so-called Hall tensor. Throughout this thesis, I am exploring both theoretically and experimentally how the effective Hall tensor of a metamaterial can be tailored by structure. On the experimental side, I am fabricating

and characterizing Hall metamaterials on the microscale. A main goal is the experimental demonstration of the sign-inversion of the effective Hall coefficient and the parallel Hall effect.

All of these efforts aim at approaching the ultimate goal of Hall metamaterials, that is, to obtain full control over the effective electrical properties of a conductive material in a weak magnetic field by tailoring its microscopic structure.

Outline of this thesis

In chapter 2, I will discuss the fundamentals that serve as a basis for the subsequent discussion of Hall metamaterials.

Theoretical aspects of Hall metamaterials will be discussed in chapter 3. Following a derivation of an equation for the effective Hall tensor, I will present two metamaterials that exhibit a sign-inversion of the effective Hall coefficient and will explain how the different components of the effective Hall tensor can be tailored. Furthermore, bounds on the effective material parameters and an extension of the theory that accounts for nontrivial distributions of the magnetic permeability will be discussed.

In chapter 4, I will introduce the methods used for the fabrication of three-dimensional Hall metamaterials on the microscale.

The corresponding experimental results that were obtained using a magneto-electric probe-station will be discussed in chapter 5. The results comprise an experimental demonstration of the sign-inversion of the effective Hall coefficient and the parallel Hall effect.

In chapter 6, I will present a fabrication technique that allows to permanently contact metamaterial microstructures on printed circuit boards, which simplifies measurements and enables potential applications.

Finally, in chapter 7, I will give a summary of this work as well as a brief outlook.

Chapter 2

2 Fundamentals

In this chapter, I will lay the groundwork for the subsequent discussion of the Hall effect in three-dimensional metamaterials. In the first part of this chapter, I will give an introduction to the classical Hall effect in isotropic homogeneous materials and briefly discuss a selection of related effects. Following a summary of tensorial material properties and corresponding symmetry considerations, I will extend the discussion of the Hall effect, on the basis of fundamental thermodynamical considerations, to anisotropic homogeneous materials. Subsequently, I will introduce the concepts of composites and metamaterials, which are materials that are inhomogeneous on a small length scale, but effectively act like a homogeneous material on a much larger length scale. In the last part of this chapter, I will give an introduction to the Hall effect in metamaterials as well as an overview over a selection of previous results.

2.1 The classical Hall effect

The classical Hall effect describes, in its original and simplest version, the appearance of a transversal voltage in a current-carrying slab of material that is subject to a magnetic field that is perpendicular to the direction of current flow. The transversal voltage is the so-called Hall voltage and the slab of material is referred to as a Hall bar. Typically, the Hall bar is made from a semiconductor and has rectangular shape. Moreover, it is usually thin in the direction of the magnetic field, which leads to a large Hall voltage for a given current.

In order to impose the current and measure the Hall voltage, one has to contact the Hall bar. While the Hall bar itself is made from a semiconductor, the contacts are usually made from a metal. In general, the conductivity of the metal is much higher than the conductivity of the semiconductor, which short-circuits the Hall bar in the vicinity of the contacts.

I my following treatment of the Hall effect, I will assume that the contacts used for measuring the Hall voltage, the sense contacts, are point-like, i.e., that they do not influence the behavior of the Hall bar and, furthermore, that the Hall bar is long, which implies that the effect of the current-injection contacts can be neglected. Moreover, I will assume that the semiconductor is strongly extrinsic, such that its behavior is dictated by one type of charge carriers. The charge carriers might be electrons or holes, which carry negative and positive charge, respectively. Importantly, for ordinary bulk materials, the sign of the Hall voltage is given by the sign of the charge carriers.

The origin of the Hall voltage as well as the dependence of its sign on the sign of the charge carriers can be understood as follows. Consider the two Hall bars corresponding to positive and negative charge carriers shown in Figure 2.1. Assume that the magnetic field[1] is along the z-direction, $\boldsymbol{b} = b\hat{\boldsymbol{z}}$, and that the Hall bars are thin in this direction. An electric current, I, is flowing in the x-direction. Hence, positive charge carries move along $\hat{\boldsymbol{x}}$ while

[1] Regarding notation, it should be mentioned that I am using lower case letters for the electric field, $\boldsymbol{e}$, the magnetic induction, $\boldsymbol{b}$, and the magnetic field, $\boldsymbol{h}$. This notation is consistent with [7]. Bold face letters are used for vectorial and tensorial quantities.

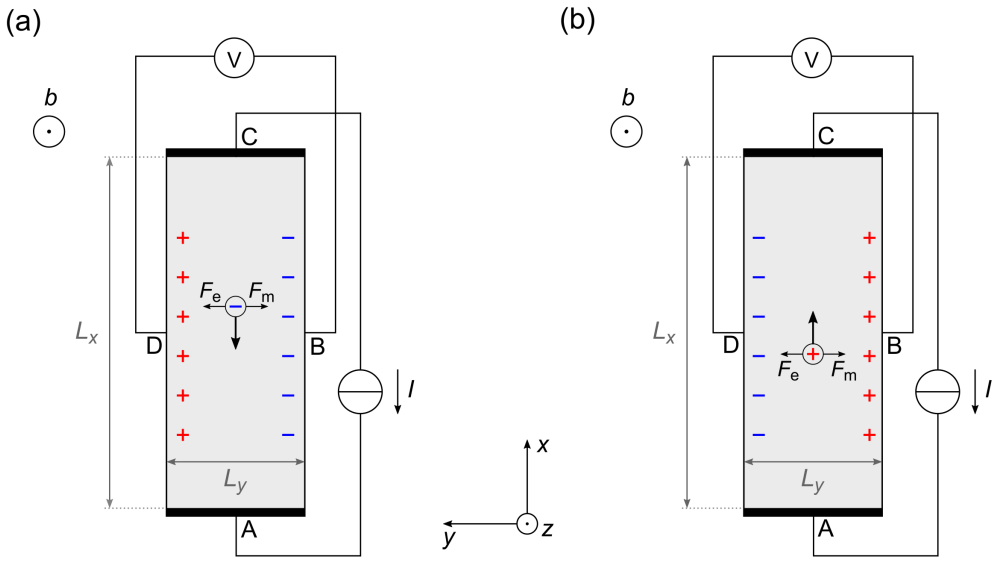

Figure 2.1: Schematic illustration of two Hall bars made from a material with positive, (a), and negative, (b), charge carriers. The magnetic field is along the z-direction. Via the current-injection contacts, A and C, a current flow along the x-direction is imposed. Hence, positive charge carriers move along $\hat{\boldsymbol{x}}$, while negative charge carriers move along $-\hat{\boldsymbol{x}}$. Due to the magnetic force, $\boldsymbol{F}_\mathrm{m}$, which is part of the Lorentz force, both types of charge carriers are initially deflected to the right, where they accumulate. This accumulation leads to a transverse electric field, the Hall electric field, $\boldsymbol{e}_\mathrm{H}$, and a corresponding force, $\boldsymbol{F}_\mathrm{e}$, that balances the magnetic force. The voltage corresponding to the Hall electric field, the Hall voltage, U_H, is measured between the sense contacts, B and D. As positive and negative charge carriers are deflected in the same direction, the corresponding Hall voltages have opposite sign. The dimensions of the Hall bar are L_x, L_y, and L_z. The Hall bars are long, i.e., L_x is much larger than L_y, such that the the influence of the current-injection contacts can be neglected. Furthermore, they are thin in the direction of the magnetic field, i.e., L_z is small as compared to the other dimensions.

negative charge carriers move along $-\hat{\boldsymbol{x}}$. Due to the magnetic force, which is part of the Lorentz force, the charge carriers are initially deflected. Both positive and negative charge carriers are deflected along $-\hat{\boldsymbol{y}}$, i.e., to the right, and accumulate on the boundary. This accumulation leads to an electric

field, the Hall electric field, $\boldsymbol{e}_\mathrm{H}$, that balances the magnetic force. The Hall voltage is the transversal voltage corresponding to the Hall electric field. Since positive and charge carriers are deflected in the same direction, the corresponding Hall voltages have opposite sign.

In the following, I will refine this discussion in order to arrive at expressions for the Hall electric field and the Hall voltage. An introduction to the underlying theory of electrical transport in semiconductors can be found in, e.g., [8]. Here, I am assuming that the semiconductor has isotropic electric properties and that an electric field, $\boldsymbol{e}$, leads to a uniform movement of the charge carriers with a constant velocity, their drift velocity, $\boldsymbol{v}_\mathrm{D}$. The relation between the electric field and the drift velocity is given by

$$\boldsymbol{v}_\mathrm{D} = \lambda \boldsymbol{e}, \tag{2.1}$$

where λ is the mobility of the charge carriers in the semiconductor[2]. This uniform movement of the charge carriers corresponds to a electric current density of

$$\boldsymbol{j} = qn\boldsymbol{v}_\mathrm{D}, \tag{2.2}$$

where q and n are the charge and the density of the charge carriers, respectively. The relation between the electric field and the current density, which is the microscopic version of Ohm's law, reads as

$$\boldsymbol{j} = \sigma_0 \boldsymbol{e} = qn\lambda \boldsymbol{e}, \tag{2.3}$$

where $\sigma_0 = qn\lambda$ is the conductivity of the material in the absence of a magnetic field.

Consider again the Hall effect in a long Hall bar as shown in Figure 2.1. The origin of the effect is action of the Lorentz force on the charge carriers,

$$\boldsymbol{F}_\mathrm{L} = \boldsymbol{F}_\mathrm{e} + \boldsymbol{F}_\mathrm{m} = q\boldsymbol{e} + q(\boldsymbol{v}_\mathrm{D} \times \boldsymbol{b}), \tag{2.4}$$

[2] The mobility is often denoted as μ. Here, I am using λ in order to avoid confusion with the magnetic permeability. Note that I am assuming that the mobility carries the sign of the charge carriers. I am not distinguishing between the drift mobility, which is the quantity defined in Equation 2.1, and the Hall mobility, which is the mobility that is determined in Hall measurements. This approximation is justified for the materials that I am using in the experiments.

where $\boldsymbol{F}_\mathrm{e}$ is the electric force and $\boldsymbol{F}_\mathrm{m}$ is the magnetic force. Due to the magnetic force, the charge carriers are deflected and accumulate on the boundary. As a consequence of this accumulation, the Hall electric field, $\boldsymbol{e}_\mathrm{H}$, builds up that balances the magnetic part of the Lorentz force,

$$0 = q\boldsymbol{e}_\mathrm{H} + q(\boldsymbol{v}_\mathrm{D} \times \boldsymbol{b}), \tag{2.5}$$

which leads to

$$\boldsymbol{e}_\mathrm{H} = -\boldsymbol{v}_\mathrm{D} \times \boldsymbol{b}. \tag{2.6}$$

Using equation 2.2, one obtains the following expression for the Hall electric field,

$$\boldsymbol{e}_\mathrm{H} = -\frac{1}{qn}(\boldsymbol{j} \times \boldsymbol{b}) = -A_\mathrm{H}(\boldsymbol{j} \times \boldsymbol{b}), \tag{2.7}$$

where $A_\mathrm{H} = 1/(qn)$ is the so-called Hall coefficient of the material. Note that the Hall coefficient carries the sign of the charge carriers. The Hall voltage is given by the line integral of the Hall electric field between the two sense contacts,

$$U_\mathrm{H} = \int_\mathrm{B}^\mathrm{D} \boldsymbol{e}_\mathrm{H} \cdot \mathrm{d}\boldsymbol{l} = A_\mathrm{H} \int_\mathrm{B}^\mathrm{D} (\boldsymbol{b} \times \boldsymbol{j}) \cdot \mathrm{d}\boldsymbol{l}. \tag{2.8}$$

Using $\boldsymbol{b} = b\hat{\boldsymbol{z}}$ and $\boldsymbol{j} = j\hat{\boldsymbol{z}}$ as in Figure 2.1 with $j = I/(L_y L_z)$, one obtains

$$U_\mathrm{H} = \frac{A_\mathrm{H}}{L_z} Ib = R_\mathrm{H} I, \tag{2.9}$$

where L_z is the thickness of the Hall bar in the direction of the magnetic field and $R_\mathrm{H} = A_\mathrm{H} b/L_z$ is the Hall resistance.

It should be noted that in the vicinity of the current-injection contacts, no Hall electric field can build up, as this part of the Hall bar is short-circuited by the current-injection contacts. In short Hall bars, i.e., for $L_x \ll L_y$, this influence of the current-injection contacts becomes dominant[3]. Instead of the appearance of a Hall electric field, a transverse current flows, i.e., the current density is tilted with respect to the x-direction.

This tilting of the current density causes longer current paths, which, for a constant imposed voltage, leads to a lower current. This increase in resistance

[3] A well-known realization of an infinitely short Hall bar is the so-called Corbino disk.

is the so-called (geometrical) magnetoresistance [9], which is proportional to $(1 + \lambda^2 b^2)$. As I am considering the limit of weak magnetic fields, I will not treat this effect in further detail.

Nevertheless, it should be emphasized that the Hall effect does not always manifest itself in the appearance of a Hall voltage. In a corresponding more general definition, the Hall effect describes the appearance of an angle between the electric field and the current density due to an external magnetic field [9]. Note that for both long and short Hall bars, such an angle appears upon imposing a magnetic field. For long Hall bars, far away from the current-injection contacts, the electric fields tilts as the Hall electric field appears while the current density is not affected. For short Hall bars, far away from the insulating boundaries, the current density tilts while the electric field does not change. This angle between the electric field and the electric current density is the so-called Hall angle, θ_{H}, which is given by [9],

$$\tan(\theta_{\mathrm{H}}) = \lambda b = \sigma_0 A_{\mathrm{H}} b. \tag{2.10}$$

Note that weak magnetic fields are equivalent to small Hall angles.

So far, I have only considered thin rectangular Hall bars for a specific set of boundary conditions. In order to study the Hall effect for arbitrary geometries[4], boundary conditions, and orientations of the fields, one has to find the constitutive relation, i.e., the general relation between the electric field and the electric current density in the material. Following [9], this relation can be derived starting from the expression for the Lorentz force, i.e., Equation 2.4. The action of this force is studied by considering an equivalent electric field,

$$q\boldsymbol{e}_{\mathrm{L}} = q\boldsymbol{e} + q(\boldsymbol{v}_{\mathrm{D}} \times \boldsymbol{b}). \tag{2.11}$$

The movement of the charge carriers under the electric field $\boldsymbol{e}_{\mathrm{L}}$ is identical to their movement under the Lorentz force. A multiplication with λn yields

$$\boldsymbol{j} = \sigma_0 \boldsymbol{e} + \sigma_0 A_{\mathrm{H}} (\boldsymbol{j} \times \boldsymbol{b}), \tag{2.12}$$

which, using the zero magnetic-field resistivity, $\rho_0 = \sigma_0^{-1}$, can be written as

$$\boldsymbol{e} = \rho_0 \boldsymbol{j} + A_{\mathrm{H}} (\boldsymbol{b} \times \boldsymbol{j}). \tag{2.13}$$

[4] If the geometry is not bar-like, one often uses the term Hall element rather than Hall bar.

Solving this equation for the current density yields[5]

$$\boldsymbol{j} = \frac{1}{1+\sigma_0^2 A_{\mathrm{H}}^2 b^2}\left(\sigma_0 \boldsymbol{e} + \sigma_0^2 A_{\mathrm{H}}(\boldsymbol{e}\times\boldsymbol{b}) + \sigma_0^3 A_{\mathrm{H}}^2 \boldsymbol{b}(\boldsymbol{e}\cdot\boldsymbol{b})\right). \tag{2.14}$$

I am dropping terms higher than first order in the magnetic field, which leads to

$$\boldsymbol{j} = \sigma_0 \boldsymbol{e} - \sigma_0^2 A_{\mathrm{H}}(\boldsymbol{b}\times\boldsymbol{e}). \tag{2.15}$$

One can rewrite these equations as, see section 2.2,

$$\boldsymbol{e} = \boldsymbol{\rho}\boldsymbol{j} \text{ with } \boldsymbol{\rho} = \rho_0 \boldsymbol{I} - A_{\mathrm{H}}\mathscr{E}(\boldsymbol{b}), \tag{2.16}$$

$$\text{and } \boldsymbol{j} = \boldsymbol{\sigma}\boldsymbol{e} \text{ with } \boldsymbol{\sigma} = \sigma_0 \boldsymbol{I} + \sigma_0^2 A_{\mathrm{H}}\mathscr{E}(\boldsymbol{b}), \tag{2.17}$$

where $\boldsymbol{I}$ is the identity, $\boldsymbol{\sigma} = \boldsymbol{\sigma}(\boldsymbol{b})$ is the magnetic-field dependent conductivity tensor, $\boldsymbol{\rho} = \boldsymbol{\rho}(\boldsymbol{b})$ is the magnetic-field dependent resistivity tensor, and $\mathscr{E} : \mathbb{R}^3 \to \mathbb{R}^{3\times 3}$ is the Levi-Civita tensor,

$$(\mathscr{E}(\boldsymbol{x}))_{ij} = \epsilon_{ijk} x_k, \tag{2.18}$$

$$\epsilon_{ijk} = \begin{cases} 1 & \text{if } (i,j,k) \text{ is an even permutation of } (1,2,3) \\ -1 & \text{if } (i,j,k) \text{ is an odd permutation of } (1,2,3) \\ 0 & \text{otherwise.} \end{cases} \tag{2.19}$$

Note that, throughout this thesis, I am using the Einstein summation convention and Latin indices take values 1, 2, or 3. In components, using the Kronecker delta, δ_{ij}, the resisitivity and conducitivity tensors are given by

$$\rho_{ij} = \rho_0 \delta_{ij} - A_{\mathrm{H}} \epsilon_{ijk} b_k \tag{2.20}$$

$$\text{and } \sigma_{ij} = \sigma_0 \delta_{ij} + \sigma_0^2 A_{\mathrm{H}} \epsilon_{ijk} b_k. \tag{2.21}$$

On this basis, one can solve the continuity equation for the electric current density,

$$\nabla \cdot \boldsymbol{j} = 0, \quad \boldsymbol{j} = \boldsymbol{\sigma}(\boldsymbol{b})\boldsymbol{e}, \quad \nabla \times \boldsymbol{e} = 0, \tag{2.22}$$

where I have assumed that the magnetic field varies slowly, $\frac{\partial \boldsymbol{b}}{\partial t} \approx 0$. One can express the problem via the electric potential, ϕ, using $-\nabla\phi = \boldsymbol{e}$, which leads to

$$\nabla \cdot (\boldsymbol{\sigma}(\boldsymbol{b})\,(\nabla\phi)) = 0. \tag{2.23}$$

[5] Note that a more thorough analysis on the basis of the Boltzmann equation, see, e.g., [8], leads to a very similar expression [9].

This problem can be solved using, for example, numerical methods such as the finite element method. In order to solve the differential equation, appropriate boundary conditions have to be imposed. For a Hall element, usually two types of boundary conditions are considered. First, for an insulating boundary, the component of the current density normal to the boundary is zero, $\boldsymbol{j} \cdot \boldsymbol{n}_{\text{bound.}} = 0$. Second, metal contacts have to be considered. As the conductivity of the metal is very high as compared to the conductivity of the semiconductor, metal contacts correspond to a constant potential on the boundary.

Subsequently, on the basis of the numerical solution, one can find the Hall voltage or other quantities of interest.

Very often, thin Hall elements, which are often referred to as Hall plates, are considered and the problem is essentially two-dimensional. In this case, instead of using numerical methods, the concept of conformal mapping can be applied, which has been used to study a vast number of geometries [9]. If the geometry is singly-connected but otherwise arbitrary, one calls it a van-der-Pauw geometry and the corresponding measurements are van-der-Pauw measurements [10, 11].

The influence of the geometry of the Hall plate, including the contacts, on the measured Hall voltage is usually described via a correction factor, G_{H},

$$U_{\text{H}} = G_{\text{H}} \frac{A_{\text{H}}}{L_z} I b, \tag{2.24}$$

with $0 < G_{\text{H}} < 1$. Certain geometries such as clover-leaf shaped Hall plates and cross-like Hall plates which leads to a large value of the correction factor, even for large contacts, are used preferentially.

Results for the geometrical correction factor of rectangular Hall plates can be found in [9, 12, 13]. For relatively long rectangular Hall plates, $L_y/L_x > 1.5$, weak magnetic fields, and a negligible size of the sense contacts, the correction factor is approximately given by [13],

$$G_{\text{H}} = 1 - \frac{16}{\pi^2} \exp\left(-\frac{\pi}{2}\frac{L_x}{L_y}\right). \tag{2.25}$$

For $L_y/L_x = 2$ and $L_y/L_x = 3$, one obtains $G_{\text{H}} \approx 0.93$ and $G_{\text{H}} \approx 0.985$,

respectively. A Hall plate with $L_y/L_x > 3$ is typically considered to act like an infinitely long Hall plate.

For point-like contacts, the treatment becomes quite simple, as the current density is independent of the magnetic field. Following some general considerations on sensitivity and noise of Hall-element based devices, I will consider point-like contacts in my subsequent treatment of a specific type of Hall elements, so-called anti-Hall bars.

Sensitivity and noise

Hall elements are commonly used for two purposes, first, in order to characterize the magnetotransport properties of a certain material and, second, for the measurement of magnetic fields. In the latter case, the Hall elements are employed as Hall sensors. Consider a long rectangular Hall bar with dimensions $L_x \times L_y \times L_z$ that is used as a Hall sensor. The measured quantity is the Hall voltage, which, for a certain magnetic field, b, and current, I, is given by Equation 2.8. The sensitivity of the Hall sensor is the ratio of the Hall voltage to the magnetic field [9]. It is often defined with respect to the imposed current. This quantity is the so-called current-related sensitivity, which, neglecting the geometrical correction factor, is given by [9],

$$S_{\text{Curr.}} = \left| \frac{U_{\text{H}}}{Ib} \right| = |A_{\text{H}}| \frac{1}{L_z}. \tag{2.26}$$

In terms of an imposed voltage, U, the Hall voltage reads as

$$U_{\text{H}} = \lambda \frac{L_y}{L_x} Ub, \tag{2.27}$$

and the sensitivity with respect to the imposed voltage, i.e., the voltage-related sensitivity, is given by [9],

$$S_{\text{Volt.}} = \left| \frac{U_{\text{H}}}{Ub} \right| = |\lambda| \frac{L_y}{L_x}. \tag{2.28}$$

Hence, in order to obtain Hall sensors with large current- and voltage-related sensitivities, one needs materials with large Hall coefficients and mobilities, respectively.

Typically, the voltage measured between the sense contacts of a Hall bar, which is referred to as the transversal voltage, U_y, is not identical to the Hall voltage. Rather, the transversal voltage is the sum of the Hall voltage and an additional magnetic-field independent contribution, the so-called offset voltage, $U_{\text{off.}}$. The offset voltage arises due to asymmetries and imperfections of the Hall bar and asymmetrically placed sense contacts. As the offset voltage is independent of the magnetic-field, it can be subtracted by measuring the transversal voltage at two different values of the magnetic field. The most common procedure is an inversion of the magnetic field [11], compare chapter 5.

For asymmetrically placed sense contacts and a rectangular Hall bar, the offset voltage can be calculated easily [9]. Assume that the sense contacts are shifted by a distance δl with respect to each other along the x-direction, i.e., along the direction of current flow. The corresponding offset voltage is given by

$$U_{\text{off}} = U\frac{\delta l}{L_x}, \tag{2.29}$$

and the ratio of the Hall voltage to the offset voltage reads as

$$\frac{U_{\text{H}}}{U_{\text{off}}} = \lambda\frac{L_y}{\delta l}b. \tag{2.30}$$

Hence, materials with high mobilities lead to Hall voltages that are large as compared to the offset voltage. Regarding the characterization of materials, a reliable subtraction of the offset voltage becomes especially important if these materials have low mobilities.

Furthermore, the measured voltage is affected by noise. The prevailing type of noise depends on the frequency [9]. Typically, at low frequencies, $1/f$-noise dominates. At high frequencies, the dominant contribution is due to thermal noise. Expressions for the corresponding signal-to-noise ratios can be found in [9]. In both cases, a larger mobility leads to larger signal-to-noise ratios.

Anti-Hall bars

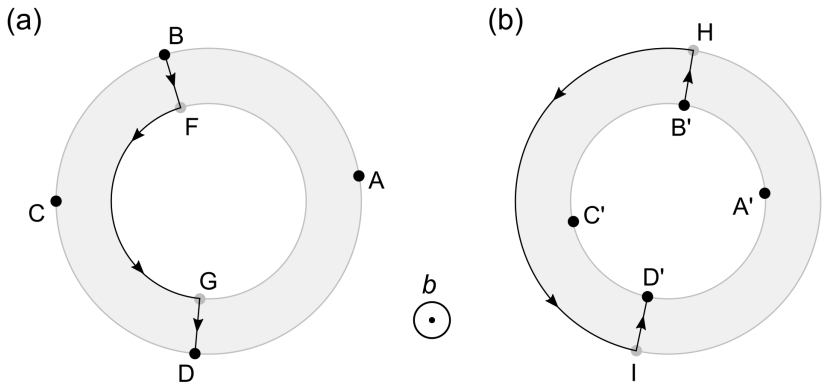

Figure 2.2: Schematic illustration of an anti-Hall bar for point-like contacts on the outer boundary (a) and inner boundary (b). The Hall bar is made from an electrically isotropic material and thin in the direction of the magnetic field. In (a), the current flows from A to C and the voltage is measured between B and D. In (b), the current flows from A′ to C′ and the voltage is measured between B′ and D′. The Hall voltages corresponding to the two configurations have the same magnitude but opposite sign. Notably, the Hall voltage is independent of the precise shape of the Hall bar. In both cases, the path of integration, which is chosen such that the integration is performed either perpendicular to the current density or along a boundary, is schematically indicated. Adapted from [14].

As a side remark, following a previous publication of mine [14], I will briefly consider the doubly-connected geometry shown in Figure 2.2. Such geometries have originally been studied in the 1990s and are called anti-Hall bars [15]. Essentially, an anti-Hall bar is a Hall plate with a hole. Upon moving all contacts from the outer to the inner boundary of the anti-Hall bar, the measured Hall voltage changes sign. Interestingly, this effect is related to the sign-inversion of the effective Hall coefficient in chainmail-inspired metamaterials, which is discussed in section 3.2.

In the following, I will discuss the origin of the sign-inversion of the Hall voltage. Consider a thin anti-Hall bar made from a material with isotropic electrical properties, zero magnetic-field resistivity ρ_0 and Hall coefficient

A_H, with point-like contacts on the outer boundary. Such a Hall bar is schematically shown in Figure 2.2(a). Assume that a current I is flowing from A to C. The voltage U_BD, which is measured between the two sense contacts, B and D, reads as

$$U_\mathrm{BD} = \rho_0 \int_\mathrm{B}^\mathrm{D} \boldsymbol{j}\,\mathrm{d}\boldsymbol{l} + A_\mathrm{H} \int_\mathrm{B}^\mathrm{D} (\boldsymbol{b} \times \boldsymbol{j})\,\mathrm{d}\boldsymbol{l}. \tag{2.31}$$

The Hall voltage, U_H, is given by the difference in U_BD caused by the magnetic field. Due to the point-like contacts, the current density, $\boldsymbol{j}$, is independent of the magnetic field. Hence, the Hall voltage is given by

$$U_\mathrm{H} = A_\mathrm{H} \int_\mathrm{B}^\mathrm{D} (\boldsymbol{b} \times \boldsymbol{j})\,\mathrm{d}\boldsymbol{l}. \tag{2.32}$$

The path of integration is split into several parts, such that for each of these parts, the integration is performed either perpendicular to the current density or along a boundary. Clearly, no current is flowing through the boundaries, i.e., at each boundary, the component of the current density normal to the boundary is zero. As a consequence, if one keeps the same sequence, the position of the contacts on the boundary is irrelevant. Only the parts of the path corresponding to an integration perpendicular to the direction of current flow contribute to the Hall voltage, which is, therefore, given by

$$U_\mathrm{H} = A_\mathrm{H} \int_\mathrm{B}^\mathrm{F} (\boldsymbol{b} \times \boldsymbol{j})\,\mathrm{d}\boldsymbol{l} + A_\mathrm{H} \int_\mathrm{G}^\mathrm{D} (\boldsymbol{b} \times \boldsymbol{j})\,\mathrm{d}\boldsymbol{l} = \frac{A_\mathrm{H}}{L_z} I b, \tag{2.33}$$

where L_z is the thickness of the Hall bar in the direction of the magnetic field.

Assume that the sense contacts are moved to the inner boundary while the current-injection contacts remain on the outer boundary or vice versa. Using the same reasoning as above, it follows immediately that the Hall voltage is zero. The Hall voltage only depends on the current that is injected in between the sense contacts on the boundary on which it is measured, compare [15].

Assume now that all of the contacts, i.e., the current-injection contacts and the sense contacts, are moved to the inner boundary. This configuration is schematically shown in Figure 2.2(b). The current is flowing from A′ to C′. The voltage is measured between B′ and D′. Using the same reasoning as above, one finds

$$U_{\mathrm{H}} = A_{\mathrm{H}} \int_{\mathrm{B}'}^{\mathrm{H}} (\boldsymbol{b} \times \boldsymbol{j})\, \mathrm{d}\boldsymbol{l} + A_{\mathrm{H}} \int_{\mathrm{I}}^{\mathrm{D}'} (\boldsymbol{b} \times \boldsymbol{j})\, \mathrm{d}\boldsymbol{l} = -\frac{A_{\mathrm{H}}}{L_z} I b. \tag{2.34}$$

Hence, as stated above, moving all contacts to the inner boundary results in a sign-inversion of the Hall voltage.

In alternative to this discussion, the problem can be approached using the concept of conformal mapping. In this formalism, the sign-inversion of the Hall voltage is related to the fact that the two configurations are connected via a so-called anti-conformal map. An anti-conformal map preserves angles but reverses their orientation.

Related effects

Since the discovery of the classical Hall effect in 1879 [1], a plethora of related effects has been studied. While a detailed discussion is beyond the scope of this thesis, I will, in the following, give a brief summary of a small selection of such effects.

Photon drag effect

The photon drag effect [16–18], which can be seen as a dynamic version of the Hall effect [19], describes the appearance of an electric field in a semiconductor on which an electromagnetic wave is impinging. Depending on the boundary conditions, instead of an electric field, an electric current may appear.

A simple explanation of the effect, in which free charge-carriers are considered only, is as follows [18, 19]. Assume that an electromagnetic wave is impinging on a semiconducting slab of material. Due to the electric field of the wave, the charge carriers are forced into an oscillatory motion. Due to the magnetic field of the wave and their motion, a Lorentz force acts on the

charge carriers, which deflects them in the direction perpendicular to both the electric and the magnetic field. Hence, the electromagnetic wave drags the charge carriers along its direction of propagation. An application of the photon drag effect is its use in detectors for electromagnetic waves. Such detectors are typically used at the wavelength of CO_2-lasers [17], i.e., at a wavelength of about 10 µm.

Thermogalvanomagnetic effects

In the discussion of the classical Hall effect, I have not considered any thermal currents or temperature gradients. However, charge carriers do not only carry charge, but also kinetic energy. In a more general discussion of electrical and thermal transport, which are closely interlinked, a variety of effects appears in the presence of a magnetic field, additionally to the Hall effect [9, 20, 21]. Usually, a distinction between galvanomagnetic and thermomagnetic effects is made.

Galvanomagnetic effects are caused by electric currents. Assume that an electric current is flowing through a long Hall-bar like sample that is subject to a perpendicular magnetic field. In addition to the Hall voltage, a transversal temperature gradient will appear, which is the so-called Ettingshausen effect. It is caused by the variation of the kinetic energy of the charge carriers. Faster charge carriers are more strongly affected by the magnetic part of the Lorentz force. Hence, the charge carriers are separated according to their kinetic energy, which causes the transversal temperature gradient [9].

Thermomagnetic effects, on the other hand, are caused by thermal currents. Assume that a thermal current is flowing through a long Hall-bar like sample that is subject to a perpendicular magnetic field. The appearance of a transversal electric voltage is the so-called Nernst effect [22]. Furthermore, the thermal current can cause a transversal temperature gradient, which is the so-called Righi-Leduc effect.

Quantum Hall effect

The quantum mechanical version of the Hall effect was discovered in 1980 by Klaus von Klitzing [23]. A brief introduction can be found in, e.g., [8]. The effect appears for a gas of free electrons that is constrained to two dimensions

at low temperatures and at strong magnetic fields in very pure samples, such that $\lambda b \gg 1$. Under these conditions, the Hall resistance exhibits plateaus in dependence of the magnetic field which are given by integer fractions of the von Klitzing constant, R_K,

$$R_H = -R_K \frac{1}{\nu} = -\frac{h}{e^2}\frac{1}{\nu} \text{ with } \nu = 1, 2, 3, \ldots \tag{2.35}$$

where h is Planck's constant and e is the elementary charge [24]. Notably, the quantum Hall effect and the constant R_K are used as a standard of the electrical resistance [25]. For his discovery, von Klitzing received the Nobel Prize in Physics in 1985.

Shortly after the discovery of the quantum Hall effect, Horst Störmer and Daniel Tsui discovered that additional plateaus appear for non-integer values of ν [26]. This is the so-called fractional quantum Hall effect. For their discovery, they received the Nobel Prize in Physics in 1998.

2.2 Tensorial properties and symmetry

In this section, I will, following [27], discuss the relation between the tensorial properties of a crystal and its symmetry. In chapter 3, I will use these considerations in the design and analysis of metamaterials, which can be seen as artificial crystals.

A tensor is a physical quantity that has, in a generalization of vectors and scalars, an arbitrary number of indices and certain transformational properties. I will limit the complexity of the treatment in the sense that I will refrain from discussing mathematical details. Furthermore, I will not discuss aspects of the theory that arise in the case of curvilinear coordinate systems, which are, e.g., encountered in the general theory of relativity.

Following an introduction to the concept of tensors, I will elaborate on the role of symmetry. The tensorial material properties of an (artificial) crystal are constrained by its symmetry. This proves most useful in two ways. First, by examining the symmetry of a given crystal, one can make a statement about its tensorial properties. Second, in aiming for certain properties, one can identify compatible symmetries, which aids in the design of a corresponding crystal.

In the description of the physical world, one makes a distinction between scalar quantities, such as temperature, pressure, or charge density, and vectorial quantities, such as the electric current density or the electric field. Vectors are quantities which are defined by a magnitude and a direction. Upon choosing a set of three axes (a coordinate system or basis), a vector is defined by its magnitude along each of the three axes, i.e., its components. Typically, the axes are mutually orthogonal and have the same normalized scaling, i.e., one chooses an orthonormal basis. The components of a vector depend on the choice of coordinate system while the vector itself is the same independently of this choice. As the coordinates of a point, the components of a vector, $\boldsymbol{v}$, transform according to

$$v_i' = a_{ij} v_j, \tag{2.36}$$

where a_{ij} are the components of a transformation matrix. I will only consider orthogonal transformation matrices, i.e., $a_{ij} a_{kj} = \delta_{ik}$ or equivalently $\boldsymbol{a}^\intercal \boldsymbol{a} = \boldsymbol{I}$,

which preserve angles and lengths and constitute the transformations between different orthonormal coordinate systems with the same origin. It follows immediately that the determinant of an orthogonal matrix can only take two values, $\det(\boldsymbol{a}) = |a_{ij}| = \pm 1$.

An orthogonal transformation matrix with determinant $|a_{ij}| = 1$ corresponds to a (proper) rotation and leaves the handedness of a coordinate system unchanged. On the other hand, an orthogonal transformation with determinant $|a_{ij}| = -1$ changes the handedness of a coordinate system, i.e., a right-handed coordinate system becomes left-handed and vice versa. It corresponds to an improper rotation, i.e., an inversion of an odd number of axes followed by a rotation.

Very often, one finds linear relations between vectorial physical quantities that are physical quantities themselves. An example is the electric conductivity tensor, $\boldsymbol{\sigma}$, which relates the electric field, $\boldsymbol{e}$, to the electric current density, $\boldsymbol{j}$. Such quantities are so-called rank-two tensors. In components, such a linear relation between two vectors, $\boldsymbol{v}$ and $\boldsymbol{w}$, is given by

$$v_i = T_{ij} w_j, \tag{2.37}$$

where T_{ij} are the components of a rank-two tensor $\boldsymbol{T}$. A tensor itself is, as it is a physical quantity, independent of the coordinate system chosen. However, as in the case of a vector, its components depend on this choice. In order to determine how the components of a rank-two tensor transform, one can use that the relation between the two vectors is independent of the coordinate system, i.e, $v_i = T_{ij} w_j$ and $v'_i = T'_{ij} w'_j$, in the original and new (primed) coordinates, respectively. These considerations lead to the following expression for the components in the primed coordinate system,

$$T'_{ij} = a_{ik} a_{jl} T_{kl}. \tag{2.38}$$

Alternatively, one can use this equation as a starting point for the definition of a rank-two tensor, i.e., a rank-two tensor is a physical quantity with components transforming according to Equation 2.38. This definition can be generalized to tensors of arbitrary rank, i.e., to an arbitrary number of indices, in which case the transformation is given by [27],

$$T'_{i_1 i_2 \ldots i_n} = a_{i_1 j_1} a_{i_2 j_2} \ldots a_{i_n j_n} T_{j_1 j_2 \ldots j_n}. \tag{2.39}$$

Vectors and scalars are two special cases, i.e., a vector is a rank-one tensor, while a scalar is a rank-zero tensor.

There are, however, quantities with a magnitude and a direction that do not transform according to Equation 2.36. Consider the cross product of two vectors, $\boldsymbol{v}$ and $\boldsymbol{w}$,

$$u_i = \varepsilon_{ijk} v_j w_k, \tag{2.40}$$

which is here expressed using the Levi-Civita tensor, see Equation 2.19, under the transformation $a_{ij} = -\delta_{ij}$, i.e., under a space-inversion. One obtains for the transformed components

$$u'_i = \varepsilon_{ijk} v'_j w'_k = \varepsilon_{ijk} a_{jl} v_l a_{km} v_m = \varepsilon_{ijk} v_j v_k = u_i = -a_{ij} u_j. \tag{2.41}$$

Clearly, equation 2.36 does not hold, but there is an additional minus sign. It can be shown that the cross product of two vectors, $\boldsymbol{u} = \boldsymbol{v} \times \boldsymbol{w}$, transforms according to

$$u'_i = \left|a_{ij}\right| a_{ij} u_j, \tag{2.42}$$

which is obviously in agreement with Equation 2.41. Quantities that transform according to Equation 2.42 are called *axial vectors* or *pseudo vectors*. Examples for axial vectors include angular momentum and magnetic field. Consider for example the magnetic field generated by a current in a circular wire-loop centered at the origin of a coordinate system. A space-inversion does not change the sense of the circular motion of the charge carriers, i.e., the magnetic field is invariant with respect to a space inversion, $\boldsymbol{b} \mapsto \boldsymbol{b}$. On the contrary, vectors, which are also called *polar vectors*, are inverted under a space inversion, $\boldsymbol{v} \mapsto -\boldsymbol{v}$.

As in the case of polar vectors, the definition of an axial vector can be generalized to objects of arbitrary rank: An axial tensor of rank n is a quantity that transforms according to [27],

$$T'_{i_1 i_2 \ldots i_n} = \left|a_{ij}\right| a_{i_1 j_1} a_{i_2 j_2} \ldots a_{i_n j_n} T_{j_1 j_2 \ldots j_n}. \tag{2.43}$$

One should note that an axial vector, i.e., an axial rank-one tensor, $\boldsymbol{v}$, can be seen as a polar rank-two tensor, $\mathscr{E}(\boldsymbol{v})$ with components $\varepsilon_{ijk} v_k$, and vice versa, as they have the same transformational properties. The cross product $\boldsymbol{v} \times \boldsymbol{w}$, where $\boldsymbol{w}$ is a vector, can be written as $-\mathscr{E}(\boldsymbol{v})\boldsymbol{w}$.

In the following, I will introduce the concept of crystals and discuss how the symmetry of a crystal influences its tensorial material parameters. The description of a crystals starts with a lattice: "A lattice is a set of points such that each point has the same environment in the same orientation" [28] or equivalently, a (three-dimensional) lattice is a set of points such that the position vector of any lattice point is given by

$$\boldsymbol{t}_n = n_1\boldsymbol{t}_1 + n_2\boldsymbol{t}_2 + n_3\boldsymbol{t}_3, \tag{2.44}$$

where n_1, n_2, and n_3 are integers. The translations $\boldsymbol{t}_n$ are called primitive translations and $\boldsymbol{t}_1$, $\boldsymbol{t}_2$, and $\boldsymbol{t}_3$ are the basic primitive translations [29]. In classifying lattices according to their symmetry, i.e., by considering two lattices to be equivalent if their symmetry groups are isomorphic, one finds that there are 14 different types of lattices, so-called Bravais lattices, in three dimensions.

In order to obtain a crystal, one has to define an arrangement of atoms relatively to all points of a lattice, called basis. A crystal is then given by the combination of a lattice and a basis.

In order to represent a crystal, it is useful to introduce the concept of unit cells. Following [30], a unit cell is a region that fills up all space in a non-overlapping way when translated via primitive translations. Other definitions that are more restrictive are used as well [31].

The symmetry group of a crystal is referred to as its space group. It is convenient to start from a more general type of length-preserving transformations, more precisely, from the transformations that are composed of an orthogonal transformation followed by a translation. Using Seitz notation [29, 32], such transformations are written as

$$\{\boldsymbol{a}|\boldsymbol{t}\}, \tag{2.45}$$

and act on a vector, $\boldsymbol{x}$, as

$$\boldsymbol{x}' = \{\boldsymbol{a}|\boldsymbol{t}\}\,\boldsymbol{x} = \boldsymbol{a}\boldsymbol{x} + \boldsymbol{t}. \tag{2.46}$$

The operations $\{\boldsymbol{I}|\boldsymbol{t}\}$, $\{\boldsymbol{a}|0\}$, and $\{\boldsymbol{I}|0\}$ correspond to pure translations, pure rotations, and the identity, respectively. A space group is a group of such symmetry operations, such that all of the pure translations of the group,

$\{\boldsymbol{I}|\boldsymbol{t}\}$, are primitive translations of a lattice. In three dimensions, there are 230 different space groups. It can be shown that any space group element can be written as [29],

$$\{\boldsymbol{a}|\boldsymbol{t}_n + \boldsymbol{\tau}(\boldsymbol{a})\}\,, \tag{2.47}$$

where $\boldsymbol{\tau}(\boldsymbol{a})$ is a translation associated with the rotation $\boldsymbol{a}$, corresponding to screw axes and glide planes, and $\boldsymbol{t}_n$ is a primitive lattice translation. Space groups containing only elements with $\boldsymbol{\tau} = 0$ are called symmorphic. All other space groups are non-symmorphic.

The rotational part of the elements of the space group of a crystal form its crystallographic point group. Furthermore, one can define the factor group of the space group with respect to the subgroup of primitive translations. The point group and the factor group of a crystal are isomorphic. The point group of a crystal is a subgroup of its space group if and only if the space group is symmorphic. In three dimensions, there are 32 different crystallographic point groups.

Furthermore, crystals can be classified according to their crystal system. In three dimensions, there are seven crystal systems, namely the triclinic, monoclinic, orthorhombic, tetragonal, trigonal, hexagonal, and cubic crystal system. Each of the space/point groups can be assigned to one of these systems. The details of this classification can be found in [31].

Having introduced the fundamental concepts of the description of crystals, I will, in the following, discuss the relation between the physical properties of an crystal and its symmetry. This link can be made via the following general statement:

> "If a system has a certain group of symmetry operations, then any physical observable of that system must also possess these symmetry operations." [28]

In the context of crystals, this principle, known as Neumann's principle, is usually stated in the following way:

> "The symmetry elements of any physical property of a crystal must include the symmetry elements of the point group of the crystal." [27]

Hence, in order to find the symmetry restrictions on a tensor describing a material property of a crystal, one has to determine the point group of the crystal. Often, it is sufficient to consider the crystal system. The symmetry of the tensor can be higher than the symmetry of the crystal, it just has to include all symmetry operations of the crystal. For example, a cubic crystal has four three-fold axes of symmetry. A rank-two tensor describing a material property of this crystal, however, is isotropic [27]. Hence, in a cubic crystal, the conductivity tensor is isotropic in the absence of a magnetic field, i.e., the crystal has isotropic electrical properties.

Starting from the point group, the symmetry restrictions on a tensor can be derived using different methods [33]. For example, for a rank-two tensor with components T_{ij}, one can evaluate

$$T_{ij} = a_{ik} a_{jl} T_{kl}, \tag{2.48}$$

for all symmetry operations. Here, it was used that the components are invariant under the symmetry operations of the crystal. This procedure results in the symmetry restrictions listed in Table 2.1. Corresponding tables for rank-two axial tensors and higher rank polar/axial tensors can be found in, e.g., [33]. In general, the higher the symmetry, the fewer components are independent and the more components vanish. Certain effects are only present if the symmetry is low enough. For example, only crystals lacking inversion symmetry can exhibit piezoelectricity.

crystal system	point groups	(polar) tensor
triclinic	1, $\bar{1}$	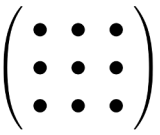
monoclinic	2, m, 2/m	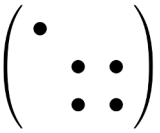
orthorhombic	2 2 2, m m 2, 2/m 2/m 2/m	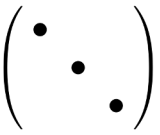
tetragonal, trigonal, hexagonal	3, $\bar{3}$, 4, $\bar{4}$, 4/m, 6, $\bar{6}$, 6/m	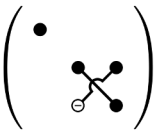
	3 2, 3 m, $\bar{3}$ 2/m, 4 2 2, 4 m m, $\bar{4}$ 2 m, 4/m 2/m 2/m, 6 2 2, 6 m m, 6 2 m, 6/m 2/m 2/m	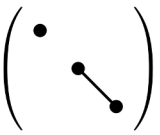
cubic	2 3, 2/m $\bar{3}$, 4 3 2, $\bar{4}$ 3 m, 4/m $\bar{3}$ 2/m	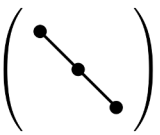

Table 2.1: The effect of different crystal symmetries on a polar rank-two tensor. The notation is as in [27]. The twofold, threefold, fourfold, and sixfold axis in the monoclinic, trigonal, tetragonal, and hexagonal system, respectively, are along the x-direction. The symmetry restrictions were adapted from [33].

2.3 The Hall effect in anisotropic materials

In my discussion of the Hall effect, I have, so far, only considered isotropic materials. The electrical properties of such materials in the presence of a magnetic field are described by two scalar quantities, the zero magnetic-field conductivity, σ_0, and the Hall coefficient, A_H. In the following, I will extend the discussion to anisotropic materials. Starting from Onsager's principle [34–36], which makes a statement about the symmetry of the kinetic coefficients of a thermodynamical system that is close to equilibrium, I will derive a general expression for the relation between the electric field and the electric current density in a weak magnetic field. The discussion follows one of my own publications [14], which summarizes previous results [36, 37].

When applied to magnetotransport, Onsager's principle implies that the magnetic-field dependent conductivity tensor, $\boldsymbol{\sigma} = \boldsymbol{\sigma}(\boldsymbol{b})$, is symmetric, if, at the same time, the magnetic field is reversed [36],

$$\boldsymbol{\sigma}(\boldsymbol{b}) = \boldsymbol{\sigma}(-\boldsymbol{b})^\mathsf{T}. \tag{2.49}$$

As stated above, I am restricting my analysis to the regime of weak magnetic fields, i.e., I will consider contributions to the conductivity tensor up to the first order in the magnetic field. The corresponding expansion reads as

$$\boldsymbol{\sigma}(\boldsymbol{b}) = \boldsymbol{\sigma}_0 + \boldsymbol{\sigma}_1(\boldsymbol{b}). \tag{2.50}$$

Applying equation 2.49 yields

$$\boldsymbol{\sigma}_0^\mathsf{T} = \boldsymbol{\sigma}_0 \text{ and } \boldsymbol{\sigma}_1(\boldsymbol{b})^\mathsf{T} = -\boldsymbol{\sigma}_1(\boldsymbol{b}). \tag{2.51}$$

Since the first-order contribution to the conductivity tensor, $\boldsymbol{\sigma}_1(\boldsymbol{b})$, is anti-symmetric and linear in $\boldsymbol{b}$, it can be written as

$$\boldsymbol{\sigma}_1 = -\mathscr{E}(\boldsymbol{S}\boldsymbol{b}), \tag{2.52}$$

where $\boldsymbol{S}$ is a rank-two tensor specifying the properties of the material in a weak magnetic field and $\mathscr{E}$ is the Levi-Civita tensor, see Equation 2.19. Hence, one obtains the following expression for the conductivity tensor in weak magnetic fields,

$$\boldsymbol{\sigma}(\boldsymbol{b}) = \boldsymbol{\sigma}_0 - \mathscr{E}(\boldsymbol{S}\boldsymbol{b}). \tag{2.53}$$

In components, this expression reads as

$$\sigma_{ij}(\boldsymbol{b}) = (\sigma_0)_{ij} - \varepsilon_{ijk} S_{kl} b_l. \tag{2.54}$$

Hence, the electrical properties of a three-dimensional material in the presence of a magnetic field are, up to the first order, specified by two rank-two tensors: The zero magnetic-field conductivity tensor, $\boldsymbol{\sigma}_0$, which is a symmetric tensor with three independent components that describes the electrical properties in the absence of a magnetic field, and a second tensor, $\boldsymbol{S}$, that accounts for contributions of the first order in the magnetic field. This second tensor, $\boldsymbol{S}$, has, in general, nine independent components.

Using the same approach for the resistivity tensor, $\boldsymbol{\rho}$, in which case, Onsager's principle implies that $\boldsymbol{\rho}(\boldsymbol{b}) = \boldsymbol{\rho}(-\boldsymbol{b})^\intercal$, yields

$$\boldsymbol{\rho}(\boldsymbol{b}) = \boldsymbol{\rho}_0 + \boldsymbol{\rho}_1(\boldsymbol{b}) = \boldsymbol{\rho}_0 - \mathscr{E}(\boldsymbol{A}_\mathrm{H}\boldsymbol{b}), \tag{2.55}$$

where $\boldsymbol{A}_\mathrm{H}$ is another rank-two tensor, the so-called Hall tensor. The choice of name becomes obvious, if one considers an isotropic conductor, $\boldsymbol{\rho}_0 = \rho_0 \boldsymbol{I}$ and $\boldsymbol{A}_\mathrm{H} = A_\mathrm{H} \boldsymbol{I}$, yielding

$$\boldsymbol{\rho}(\boldsymbol{b}) = \rho_0 \boldsymbol{I} + A_\mathrm{H} \mathscr{E}(\boldsymbol{b}), \tag{2.56}$$

which is identical to Equation 2.16. Hence, the Hall tensor, $\boldsymbol{A}_\mathrm{H}$, can be seen as a generalization of the scalar Hall coefficient, A_H, to anisotropic materials.

In summary, this treatment yields the following relations between the electric current density and the electric field,

$$\boldsymbol{e} = (\boldsymbol{\rho}_0 - \mathscr{E}(\boldsymbol{A}_\mathrm{H}\boldsymbol{b}))\boldsymbol{j} \tag{2.57}$$

$$\text{and } \boldsymbol{j} = (\boldsymbol{\sigma}_0 - \mathscr{E}(\boldsymbol{S}\boldsymbol{b}))\boldsymbol{e}. \tag{2.58}$$

Using the cross product, these relations can be expressed as

$$\boldsymbol{e} = \boldsymbol{\rho}_0 \boldsymbol{j} + (\boldsymbol{A}_\mathrm{H}\boldsymbol{b}) \times \boldsymbol{j} \tag{2.59}$$

$$\text{and } \boldsymbol{j} = \boldsymbol{\sigma}_0 \boldsymbol{e} + (\boldsymbol{S}\boldsymbol{b}) \times \boldsymbol{e}, \tag{2.60}$$

and the generalized expression for the Hall electric field reads as

$$\boldsymbol{e}_\mathrm{H} = (\boldsymbol{A}_\mathrm{H}\boldsymbol{b}) \times \boldsymbol{j}. \tag{2.61}$$

Notably, in the anisotropic case, components of the Hall electric field parallel to the magnetic field, $\boldsymbol{b}$, may arise. In contrast, in the isotropic case, the Hall electric field is always perpendicular to the magnetic field. In both cases, the Hall electric field is perpendicular to the direction of current flow. These aspects are further discussed in section 3.3.

In order to apply the symmetry considerations outlined in section 2.2, one has to show that the quantity $\boldsymbol{A}_\mathrm{H}$ is indeed a tensor. Note that the resistivity tensor and, hence, $-\mathscr{E}(\boldsymbol{A}_\mathrm{H}\boldsymbol{b})$ are polar rank-two tensors. Furthermore, $-\mathscr{E}(\boldsymbol{A}_\mathrm{H}\boldsymbol{b})$ is antisymmetric with $\boldsymbol{A}_\mathrm{H}\boldsymbol{b}$ being the corresponding axial vector, compare section 2.2. Therefore, since the magnetic induction, $\boldsymbol{b}$, is an axial vector, it follows that $\boldsymbol{A}_\mathrm{H}$ is a polar tensor [14, 36]. The corresponding considerations for the tensor $\boldsymbol{S}$ are analogous.

The contribution of a weak magnetic field to the conductivity tensor is now alternatively defined by two tensors, $\boldsymbol{A}_\mathrm{H}$ and $\boldsymbol{S}$. From $\boldsymbol{\rho} = \boldsymbol{\sigma}^{-1}$, using $\boldsymbol{M}^\intercal\mathscr{E}(\boldsymbol{x})\boldsymbol{M} = \mathscr{E}(\mathrm{Cof}(\boldsymbol{M})^\intercal\boldsymbol{x})$ for any $\boldsymbol{x} \in \mathbb{R}^3$ and $\boldsymbol{M} \in \mathbb{R}^{3\times3}$, one obtains the following relation between these two tensors [37],

$$\boldsymbol{S} = -\mathrm{Cof}(\boldsymbol{\sigma}_0)\boldsymbol{A}_\mathrm{H}, \tag{2.62}$$

which holds up to the first order in the magnetic field. Here, $\mathrm{Cof}(\boldsymbol{\sigma}_0)$ is the cofactor of the zero magnetic-field conductivity tensor, $\boldsymbol{\sigma}_0$. The cofactor of a matrix $\boldsymbol{A}$ is defined as

$$(\mathrm{Cof}(\boldsymbol{A}))_{ij} = (-1)^{(i+j)}\boldsymbol{M}(i,j), \tag{2.63}$$

where $\boldsymbol{M}(i,j)$ is the (i,j)-minor of $\boldsymbol{A}$, i.e., the determinant of the submatrix formed by deleting the i-th row and j-th column. Notably, the transpose of the cofactor, the adjugate, appears in the following well-known expression for the inverse matrix,

$$\boldsymbol{A}^{-1} = \frac{1}{\det(\boldsymbol{A})}\mathrm{Cof}(\boldsymbol{A})^\intercal, \tag{2.64}$$

where $\det(\boldsymbol{A})$ is the determinant of $\boldsymbol{A}$. In the isotropic case, Equation 2.62 reduces to $\boldsymbol{S} = \sigma_0^2 A_\mathrm{H}\boldsymbol{I}$, which yields Equation 2.17.

2.4 Metamaterials

In the following, I will introduce the concepts of composites and metamaterials. Composites are materials that are structured on a small length scale and that are composed of a single porous or two or more constituent materials. On a much larger length scale, a composite acts like a homogeneous material with certain properties, its so-called effective properties. It is assumed that the small length scale is still large as compared to the size of an atom and that the laws of classical physics can be applied.

Examples for composites that can be found in nature are wood and bone. Well-known examples for artificial composites are reinforced concrete and fiber-reinforced polymers [7]. Often, composites are used to combine certain properties of two or more constituent materials. However, one can go far beyond that. The effective properties of a composite do not need to lie in between the properties of the constituent materials but can be very different. One can even obtain properties that are usually not found in nature. The key to this unusual effective behavior is the microscopic structure of the composite. If this microscopic structure is artificially tailored in order to obtain such unusual effective properties, one typically refers to the material as a metamaterial.

Notably, the field of metamaterials has a long history, while the term itself is relatively new [38, 39]. For example, metamaterials with a refractive index less than one that are composed of conducting rods have been studied in the 1950s [40].

While there is no generally accepted definition, metamaterials are usually seen as a specific type of composites. Throughout this thesis, I am using the term metamaterial for artificial composites with effective properties that go beyond the properties of the constituent materials and that are determined by a specifically chosen structure. However, more restrictive definitions are sometimes used as well [38, 39]. In the following, I will only discuss periodic metamaterials that can be seen as artificial crystals in the sense that they are periodic arrangements of certain building blocks.

As stated above, the effective properties of a metamaterial can be very different from the properties of the constituent materials. Especially interesting are sign-inversions of effective parameters with respect to the parameters

of the constituent materials. For example, the effective thermal expansion coefficient of a material made from two constituent materials with positive thermal expansion coefficients and voids can be negative [41–43]. This behavior is closely connected to a negative poroelastic compressibility [7, 42, 44, 45]. Notably, these are two examples for the sign-inversion of an effective material parameter in static problems. In the dynamic case, based on resonances, many more sign-inversions have been realized. Examples include the magnetic permeability [46, 47] and the mass density [48]. Note that in the dynamic case, the wavelength imposes an upper limit on the scale on which the metamaterial is structured, i.e., on the size of the unit cell of the metamaterial.

Metamaterials are useful for a number of reasons. First, using metamaterials, it is possible to realize material properties or combinations of material properties that are not available otherwise and that are not normally found in nature. Second, even if certain material properties are available otherwise, it is often possible to realize those properties starting from very few constituent materials, or even a single one. Third, using metamaterials, it is possible to realize property gradients or spatially varying distributions of material properties that can be tailored to specific needs.

In the following, I will consider the problem of electric conduction in a composite or metamaterial [7]. As stated above, one has to distinguish between different length scales. The microscopic scale is the scale on which the material is structured and, hence, the scale on which the microscopic conductivity tensor, σ, varies. The corresponding quantities are the microscopic electric field, $\boldsymbol{e}$, and the microscopic current density, $\boldsymbol{j}$. On the microscopic scale, the conductivity equations read as

$$\nabla \cdot \boldsymbol{j} = 0, \quad \boldsymbol{j} = \sigma \boldsymbol{e}, \quad \nabla \times \boldsymbol{e} = 0. \tag{2.65}$$

On the macroscopic scale, the corresponding equations read as

$$\nabla \cdot \langle \boldsymbol{j} \rangle = 0, \quad \langle \boldsymbol{j} \rangle = \sigma^* \langle \boldsymbol{e} \rangle, \quad \nabla \times \langle \boldsymbol{e} \rangle = 0. \tag{2.66}$$

Here, $\langle \boldsymbol{e} \rangle$ and $\langle \boldsymbol{j} \rangle$ are the macroscopic electric field and the macroscopic current density, respectively, which are related to the corresponding microscopic quantities via an average on an intermediate length scale. Furthermore, σ^* is the effective conductivity tensor, which is constant or varies slowly. Usually,

the goal is to find the effective conductivity tensor of a given structure or, in the inverse case, to find a structure that exhibits a given effective conductivity tensor. In general, the effective conductivity depends on the microscopic conductivity in a very complicated way and is not given by an average.

An example of a simple application is the realization an anisotropic effective conductivity tensor from isotropic constituent materials. Consider a material composed of alternating layers of two isotropic constituent materials, i.e., a laminate. On the macroscopic length scale, the laminate effectively acts like a homogeneous medium with anisotropic properties. Assume that one of the constituent materials is highly conducting while the second constituent material is weakly conducting. Perpendicular to the layers, the behavior can be described via a network of resistors that are connected in series. Along this direction, the effective behavior is determined by the weakly conducting material and the corresponding component of the effective conductivity tensor is small. Parallel to the layers, the behavior can be described via a network of resistors that are connected in parallel. Along this direction, the effective behavior is determined by the highly conducting material and the corresponding component of the effective conductivity tensor is large.

It should be noted that the problem of electric conduction is mathematically equivalent to a large number of problems [7, 49], including the problems of magnetostatics, antiplane elasticity, thermal conduction, and particle or light diffusion. All of these problems are described by Equation 2.65, by assigning different meaning to the quantities appearing there. For example, in magnetostatics, the magnetic field, $\boldsymbol{h}$, and the magnetic induction, $\boldsymbol{b}$, correspond to the electric field, $\boldsymbol{e}$, and the electric current density, $\boldsymbol{j}$, respectively, while the magnetic permeability tensor, $\boldsymbol{\mu}$, plays the role of the electric conductivity tensor, $\boldsymbol{\sigma}$.

As the theoretical description is not constrained to a specific problem, it is possible to apply ideas and concepts across a wide range of fields, which has proven immensely fruitful, see, e.g., [7, 39, 50].

Nevertheless, in the application and transfer of concepts to a specific field, care has to be taken for a number of reasons. First, the description of a physical system via a differential equation is based on certain assumptions. For example, the mean free path has to be small compared to the feature size of the microscopic structure. Typical values of the mean free path depend

on the problem and differ by orders of magnitude. Second, the range of properties of available constituent materials heavily depends on the problem considered. In general, the values of the corresponding quantities of the same material might be different for each problem. For example, the electric conductivity of vacuum is zero while the magnetic permeability is not. Third, the typically encountered boundary conditions might be very different. For example, if one places an electric conductor in vacuum or air, the surrounding medium is an insulator and one obtains insulating boundary conditions. The situation is different for the problem of diffusive light transport [51]. Assume that a light-scattering diffusive medium is placed in vacuum or air, which are media that are not diffusive. One typically assumes that all photons that leave the diffusive medium are lost, i.e., that no light will enter the diffusive medium from outside. These considerations lead to a rather unusual and very different boundary condition [52].

Following this short discussion, it becomes clear that, while many ideas can be transfered across a wide range of fields, the peculiarities of each problem have to be considered.

Bounds

Bounds are a central aspect of the theory of composites and metamaterials. In general, bounds are inequalities that relate different microscopic and macroscopic physical quantities [7]. Typically, a bound limits the range of effective properties of a composite that are accessible – by tuning its microscopic structure – as a function of the constituent material's properties. In general, a bound should be as tight as possible. Ideally, one can find a composite that attains a certain bound, in which case the bound is optimal.

The importance of bounds has a number of reasons. First, bounds allow to make a statement whether there is hope to obtain certain effective properties or whether a certain strategy is worth pursuing. For example, in thermoelectric composites, the dimensionless figure of merit, the ZT value, cannot be larger than its largest value among the constituent materials [53]. Hence, trying to find a composite exhibiting a larger ZT value under the assumptions underlying the bound is a fruitless endeavor.

Second, bounds provide a reference scale. An engineer optimizing a

composite can compare its effective properties to the corresponding bound(s) and see whether there is room for improvement. Of course, in practice, it is often not sufficient to find a composite that is optimal in the sense that its effective properties attain a certain bound, but other considerations such as cost-efficiency and whether it can be fabricated easily play an important role as well.

Third, bounds are crucial for inferring information about a system, i.e., for inverse problems. If the effective properties of a composite are bounded as a function of the microscopic properties of the composite, such as the number or properties of the constituent material(s) or their volume fractions, measuring the effective properties will yield information about the microscopic properties. For example, in two-dimensional composites, the effective Hall coefficient cannot be sign-inverted, see chapter 3, which means that if one measures a positive (negative) effective Hall coefficient for a two-dimensional composite, at least one of the constituent materials must have a positive (negative) Hall coefficient. Notably, this is not true for three-dimensional composites.

Fourth, a bound is based on certain assumptions and, hence, by dropping one of these assumptions, one might be able to exceed it. Therefore, a bound provides information on how to overcome it.

It should be noted that these considerations are not limited to bounds on effective parameters but can be applied to more general bounds as well. An example of such a bound is the Shockley-Queisser limit, which gives an upper bound to the efficiency of a single-junction solar cell using the spectrum of the sun as a function of the bandgap of the material [54].

In section 3.4, I will discuss certain bounds that are relevant in the context of the Hall effect in composites and metamaterials.

2.5 The Hall effect in composites and metamaterials

Having introduced the classical Hall effect and the concept of metamaterials, I will in the subsequent chapters discuss how one can use metamaterials in order to obtain control over the effective properties that are relevant in the context of the Hall effect.

As mentioned above, the effective conductivity tensor, σ^*, relates the macroscopic electric field, $\langle \boldsymbol{e} \rangle$, to the macroscopic current density, $\langle \boldsymbol{j} \rangle$. In the limit of weak magnetic fields, the effective conductivity tensor is determined by the zero magnetic-field conductivity tensor, σ_0^*, and the tensor $\boldsymbol{S}^*$,

$$\sigma^* = \sigma_0^* - \mathscr{E}(\boldsymbol{S}^* \boldsymbol{b}). \tag{2.67}$$

Instead of the tensor $\boldsymbol{S}^*$, I am usually considering the effective Hall tensor, $\boldsymbol{A}_{\mathrm{H}}^*$, that is given by

$$\boldsymbol{S}^* = -\mathrm{Cof}(\sigma_0^*) \boldsymbol{A}_{\mathrm{H}}^*. \tag{2.68}$$

Hence, the electrical properties of a metamaterial in a weak magnetic field can be tailored by adjusting the components of the effective Hall tensor. Two cases can be distinguished: In the isotropic case, the effective Hall tensor reduces to the scalar effective Hall coefficient. As it turns out, one has quite a lot of freedom in tailoring the effective Hall coefficient of a three-dimensional metamaterial. Most interestingly, in three dimensions, the effective Hall coefficient can be sign-inverted. In the anisotropic case, one can, for example, realize antisymmetric Hall tensors and tailor the angle between the magnetic field and the macroscopic Hall electric field.

My own results are based on the seminal work of Briane and Milton, who designed the first metamaterial with a sign-inverted effective Hall coefficient [55] as well as the first metamaterial with an antisymmetric Hall tensor [37]. A number of further theoretical results can be found in the books of Milton [7] and Grabovsky [56].

Before discussing the theoretical description of the Hall effect in metamaterials in detail in the next chapter, it is worth mentioning that the Hall effect in composites has been studied for more than half a century. In the following, I will give an overview over a selection of these results.

Already in 1956, Juretschke, Landauer, and Swanson studied the effect of voids in an isotropic conductive medium at weak magnetic fields [57]. Under

the assumption that the voids are completely surrounded by the conductive medium and sufficiently far apart, the authors derived explicit expressions for the effective Hall coefficient for cylindrical and spherical voids.

A number of later publications was dedicated to percolation theory, see [58–60] and references therein. For three-dimensional metal-insulator composites and weak magnetic fields, Bergman *et al.* showed, using a random-resistor-network model, that the Hall coefficient diverges at the percolation threshold [60]. More precisely, close to the percolation threshold, the effective Hall coefficient exhibits a power law behavior, $A_{\mathrm{H}}^{*} \propto (p - p_{\mathrm{c}})^{-g}$, where p is the metal fraction, p_{c} is the percolation threshold, and $g > 0$ is the corresponding critical exponent. Note that the effective conductivity follows a power law as well, $\sigma^{*} \propto (p - p_{\mathrm{c}})^{t}$ with $t > 0$, and that it vanishes at the percolation threshold. In section 3.4, I will discuss that the effective conductivity has to vanish if the effective Hall coefficient diverges, see also [61]. In two dimensions, the effective Hall coefficient does not diverge at the percolation threshold [59], which becomes clear if one considers the corresponding bound, see [62].

The results obtained from percolation theory were later confirmed experimentally. Rohde and Micklitz studied the Hall effect in a rare-gas metal mixture and found that the effective Hall coefficient exhibits the expected critical behavior [63]. Dai, Palevski, and Deutscher confirmed the behavior for random composites composed of aluminum and germanium that were fabricated by vacuum coevaporation [64]. While these systems are very interesting, it should be mentioned that I would refrain from referring to such composites as metamaterials, since one has only very limited control over the microscopic structure, which is the result of a random process.

Theoretical results for the Hall effect in periodic composites for strong magnetic fields can be found in [65] and [66]. In [65], Bergman and Strelniker studied simple cubic arrangements of spherical and cylindrical inclusions in a conducting medium. Interestingly, at high magnetic fields, the magnetoresistance exhibits a very strong anisotropy. Corresponding experiments were carried out by Tornow *et al.* [67]. The authors studied the effect in Hall bars made from thin GaAs films with a periodic arrangement of cylindrical voids. The experiments clearly showed the expected strong anisotropy of the magnetoresistance in dependence of the angle between the direction of current flow

and the magnetic field. The mobility of the films was $\lambda = 2500\,\mathrm{cm^2\,V^{-1}\,s^{-1}}$ and a magnetic induction, lying in the plane of the films, of up to 12 T was used, which led to $\lambda b > 1$. The mean free path was much smaller than the diameter of the cylindrical inclusions and, hence, the transport was still diffusive.

Chapter 3

3 Theory of Hall metamaterials

In this chapter, I will introduce the theory of three-dimensional Hall metamaterials. First, I will discuss the fundamentals, derive an equation for the effective Hall tensor, and briefly summarize the corresponding numerical methods. Thereafter, I will discuss two types of isotropic metamaterials that exhibit a sign-inversion of the effective Hall coefficient. The first such type consists of interlinked tori and was inspired by Japanese chainmail. The second type is based on the inversion of a local Hall voltage. Subsequently, I will summarize the theoretical results on Hall metamaterials with lower symmetry, which allow to realize anisotropic effective Hall tensors. Such metamaterials can exhibit the parallel Hall effect and give control over the orientation of the Hall electric field. Following a brief discussion of bounds on the effective properties, I will, in the last part of this chapter, consider a generalized version of Hall metamaterials that accounts for distributions of the magnetic permeability within the unit cell. Two examples of such metamaterials will be given, which employ such distributions to invert the sign of the effective Hall coefficient and to extend the range of accessible effective parameters.

3.1 Fundamentals

In the following, I will discuss the theory of three-dimensional Hall metamaterials in the limit of weak magnetic fields. Throughout this chapter, I will follow one of my previous publications [14]. In detail, the underlying theory and the derivation of the corresponding equations are discussed in the publications of Marc Briane and Graeme Milton, see [7, 37, 55] and references therein. In several of these publications, the problem is treated in a mathematically much more thorough way using the concept of H-convergence [68].

In this section, I will derive expressions for the effective properties of three-dimensional Hall metamaterials, i.e., the effective zero magnetic-field conductivity tensor, $\boldsymbol{\sigma}_0^*$, and the effective Hall tensor, $\boldsymbol{A}_\mathrm{H}^*$, based on the corresponding microscopically varying properties, $\boldsymbol{\sigma}_0$ and $\boldsymbol{A}_\mathrm{H}$, respectively. I am assuming that the metamaterial is a periodic arrangement of cubic unit cells with lattice constant a. The relevant physical quantities on the scale of the unit cell of the metamaterial are the microscopic electric field, $\boldsymbol{e}$, and the microscopic electric current density, $\boldsymbol{j}$. The corresponding macroscopic quantities are the macroscopic electric field, $\langle \boldsymbol{e} \rangle$, and the macroscopic electric current density, $\langle \boldsymbol{j} \rangle$, which are defined as the average of the microscopic quantities, where the average is taken over a region that is large compared to one unit cell and small compared to the macroscopic object and the scale of variations of the applied boundary conditions [7, 14].

The regime in which the microstructure effectively acts like a material, i.e., the effectively homogeneous case, is approached by making the unit cell smaller and smaller. If the unit cell is small enough, one can assume that the macroscopic electric field is constant on its scale. Then, the microscopic electric field is given by the sum of two contributions [7]. The first contribution has a vanishing average. The second contribution has a constant average that is given by the macroscopic electric field. For each of the three axes, one can now solve the conductivity problem for a normalized macroscopic electric field pointing along the axis, which leads to three solutions of the microscopic electric field and the corresponding potential, Φ_1, Φ_2, and Φ_3. These potentials can be written in the form of a vector, the vector-valued electric potential, $\boldsymbol{\Phi} = (\Phi_1, \Phi_2, \Phi_3)^\mathsf{T}$. Then, for an arbitrary macroscopic

electric field, the microscopic electric field is given by the linear combination

$$\boldsymbol{e} = -\left(\nabla \boldsymbol{\Phi}\right) \langle \boldsymbol{e} \rangle, \ \left(\nabla \boldsymbol{\Phi}\right)_{ij} = \frac{\partial \phi_j}{\partial x_i}, \tag{3.1}$$

and the vector-valued potential, $\boldsymbol{\Phi}$, solves

$$\nabla \cdot (\sigma \nabla \boldsymbol{\Phi}) = 0. \tag{3.2}$$

In terms of the vector-valued electric potential, the aforementioned conditions on the electric field translate to an invariance of $\boldsymbol{\Phi}(\boldsymbol{x}) + \boldsymbol{x}$ with respect to primitive translations of the metamaterial crystal. The electric field associated with the vector-valued potential is matrix-valued,

$$\boldsymbol{E} = -\nabla \boldsymbol{\Phi} \text{ or } E_{ij} = -\frac{\partial \Phi_j}{\partial x_i}, \tag{3.3}$$

and normalized, $\langle \boldsymbol{E} \rangle = \boldsymbol{I}$.

Based on these results, the effective conductivity of the metamaterial can be obtained by considering the constitutive equation on the macroscopic scale, which is given by

$$\langle \boldsymbol{j} \rangle = \sigma^* \langle \boldsymbol{e} \rangle . \tag{3.4}$$

Hence, it follows that

$$\sigma^* = \sigma^* \langle \boldsymbol{E} \rangle = -\langle \sigma \nabla \boldsymbol{\Phi} \rangle . \tag{3.5}$$

Here and in the following, the average is taken over a single unit cell. In the following, I will assume that $\boldsymbol{\Phi}$ solves Equation 3.2 for zero magnetic field, i.e., $\sigma = \sigma_0$. In this case, Equation 3.5 yields the effective zero magnetic-field conductivity, σ_0^*.

In order to obtain an expression for the effective Hall tensor, I am assuming that the magnetic field is weak ($\lambda b \ll 1$), which implies that the Hall effect is a small perturbation to the conductivity tensor, $\sigma = \sigma_0 + \delta\sigma$ and $\sigma^* = \sigma_0^* + \delta\sigma^*$ with $\delta\sigma = -\mathscr{E}(\boldsymbol{S}\boldsymbol{b})$ and $\delta\sigma^* = -\mathscr{E}(\boldsymbol{S}^*\boldsymbol{b})$. The key idea is that, in this case, one can obtain the effective Hall tensor from a solution of the problem for zero magnetic field [69]. The corresponding treatment of such perturbations is described in [7]. Let $\boldsymbol{e}$ be a solution to

$$\nabla \cdot \boldsymbol{j} = 0, \quad \boldsymbol{j} = \sigma_0 \boldsymbol{e}, \quad \nabla \times \boldsymbol{e} = 0. \tag{3.6}$$

Then, one has the following identity [7],

$$\langle \boldsymbol{e} \rangle \cdot \delta\boldsymbol{\sigma}^* \langle \boldsymbol{e} \rangle = \langle \boldsymbol{e} \cdot (\delta\boldsymbol{\sigma})\, \boldsymbol{e} \rangle. \tag{3.7}$$

One can now insert the three electric fields corresponding to the three axes,

$$\langle \boldsymbol{E} \rangle^\intercal \delta\boldsymbol{\sigma}^* \langle \boldsymbol{E} \rangle = \langle \boldsymbol{E}^\intercal\, (\delta\boldsymbol{\sigma})\, \boldsymbol{E} \rangle. \tag{3.8}$$

Using $\langle \boldsymbol{E} \rangle = \boldsymbol{I}$ and $\boldsymbol{M}^\intercal \mathscr{E}(\boldsymbol{x}) \boldsymbol{M} = \mathscr{E}(\mathrm{Cof}(\boldsymbol{M})^\intercal \boldsymbol{x})$ for any $\boldsymbol{x} \in \mathbb{R}^3$ and $\boldsymbol{M} \in \mathbb{R}^{3\times 3}$, gives

$$\mathscr{E}\left(\boldsymbol{S}^* \boldsymbol{b}\right) = \left\langle \mathscr{E}\left(\mathrm{Cof}\left(\nabla\boldsymbol{\Phi}\right)^\intercal \boldsymbol{S}\boldsymbol{b}\right)\right\rangle, \tag{3.9}$$

which leads to

$$\boldsymbol{S}^* = \left\langle \mathrm{Cof}\left(\nabla\boldsymbol{\Phi}\right)^\intercal \boldsymbol{S}\right\rangle. \tag{3.10}$$

Typically, instead of $\boldsymbol{S}^*$, one rather considers the effective Hall tensor, for which, using Equation 2.62, one obtains [37],

$$\mathrm{Cof}\left(\boldsymbol{\sigma}_0^*\right) \boldsymbol{A}_\mathrm{H}^* = \left\langle \mathrm{Cof}\left(\boldsymbol{\sigma}_0 \nabla\boldsymbol{\Phi}\right)^\intercal \boldsymbol{A}_\mathrm{H}\right\rangle, \tag{3.11}$$

which is an extension of the results derived by David Bergman [69]. This expression represents a weighted volume average of the microscopic Hall tensor of the structure. The weights are given by the cofactor of the matrix-valued current density, $\boldsymbol{C} = \mathrm{Cof}\left(\boldsymbol{\sigma}_0 \nabla\boldsymbol{\Phi}\right)$. The cofactor, therefore, determines if and how the microscopic Hall tensor at a certain location within the unit cell enters into the effective Hall tensor of the metamaterial.

Intuitively, the cofactor of the matrix-valued current density, which appears in the equation for the effective Hall tensor, can be understood as follows. First, note that each cofactor corresponds to a specific direction of the magnetic field. More precisely, assuming isotropic constituent materials, the first index of C_{ij} corresponds to the direction of the magnetic field. In the following, I will only consider C_{33}, which is given by $C_{33} = J_{11}J_{22} - J_{12}J_{21}$ with $\boldsymbol{J} = \boldsymbol{\sigma}_0 \boldsymbol{E}$. This cofactor corresponds to a magnetic field in the z-direction. Hence, it only depends on microscopic current flows in the x- and y-direction, i.e., it is independent of J_{31}, J_{32}, and J_{33}. Due to the action of the Lorentz-force, a microscopic current flow in the x- or y-direction leads to corresponding perpendicular microscopic current flow. In order for this perpendicular microscopic current flow to be measurable, it has to lead to a macroscopic

current flow. Furthermore, it is irrelevant whether a microscopic current flow in the xy-plane is related to a macroscopic current flow in the x- or the y-direction. Hence, it is the products $J_{11}J_{22}$ and $-J_{12}J_{21}$ that determine the effective behavior of the material. The minus sign of the second product can be understood, e.g., by considering a spiral-like structure that translates macroscopic current flows along $\hat{\boldsymbol{x}}$ and $\hat{\boldsymbol{y}}$ to microscopic current flows along $\hat{\boldsymbol{y}}$ and $-\hat{\boldsymbol{x}}$, respectively.

In the case of isotropic structures, Equation 3.11 reduces to an expression for the effective Hall coefficient. Note that such an isotropic behavior is implied by cubic crystal symmetry. Aside from using Equation 3.11 to calculate the effective Hall tensor of a metamaterial, it was used in an inverse sense, in order to design metamaterials with targeted effective Hall tensors, which I will elaborate on in the following sections. Before that, I will summarize the corresponding numerical methods.

Two types of numerical calculations were carried out using the finite element method, see, e.g., [70]. Calculations for infinitely extended crystals, compare [14], were used to determine the effective properties of Hall metamaterials by evaluating Equation 3.5 and Equation 3.11. Further insight was obtained by plotting the cofactor of the matrix-valued current density. Second, additional calculations were performed for finite structures [14, 71–73]. In both cases, the electric current module of the commercial software package COMSOL Multiphysics (COMSOL Inc.) was used.

The calculations for infinitely extended crystals were performed by solving Equation 3.2 for $\boldsymbol{\sigma} = \boldsymbol{\sigma}_0$. More precisely the conductivity problem was solved separately for each of the three electric potentials, Φ_1, Φ_2, and Φ_3. The boundary conditions, i.e., the invariance of $\boldsymbol{\Phi}(\boldsymbol{x}) + \boldsymbol{x}$ with respect to primitive lattice translations, are implemented as follows.

The first component of the vector-valued electric potential, Φ_1, is periodic along the y- and z-direction, which is implemented using the corresponding built-in functionality of the software. Along the x-direction, Φ_1 is the sum of a periodic contribution and a potential drop that is chosen such that the corresponding electric field is normalized, which is implemented using a weak contribution and the linear extrusion feature of the software. For Φ_2 and Φ_3, the procedure is analogous.

For structures with a certain symmetry, the boundary conditions can be

simplified [14]. If the unit cell has mirror symmetry with respect to the three planes that pass through its center and that are perpendicular to each of the three axes, it follows that each of the three potentials is constant on two of the outer boundaries, while all other boundaries are insulating [14]. More precisely, one obtains $\Phi_1(-\frac{a}{2}, x, y) = c$ and $\Phi_1(\frac{a}{2}, x, y) = c + a$ and analogous conditions for Φ_2 and Φ_3, which can be directly implemented using the corresponding functionality of the software[1]. Here, c is a constant that can be chosen arbitrarily.

Once the vector-valued electric potential, $\boldsymbol{\Phi}$, is known, the evaluation of Equation 3.5 and Equation 3.11 and the calculation of the cofactor of the matrix-valued electric current density, $\boldsymbol{C}$, are straightforward.

It should be pointed out that, while it is possible to calculate the effective properties using this specific type of periodic boundary conditions, calculations for finite structures are still important. These calculations were performed by solving the continuity equation,

$$\nabla \cdot (\boldsymbol{\sigma} \nabla \phi) = 0, \tag{3.12}$$

with the conductivity tensor,

$$\boldsymbol{\sigma} = \sigma_0 \begin{pmatrix} 1 & \sigma_0 A_{\mathrm{H}} b_z & 0 \\ -\sigma_0 A_{\mathrm{H}} b_z & 1 & 0 \\ 0 & 0 & 1 \end{pmatrix}, \tag{3.13}$$

thereby prescribing a magnetic field, $b_z \hat{\boldsymbol{z}}$, along the z-direction. I am assuming that the structures are made from isotropic materials, i.e., that the (microscopic) properties are the spatially varying scalar zero magnetic-field conductivity, σ_0, and Hall coefficient, A_{H}^0. In the calculations, a current flow is imposed by prescribing a constant potential on the corresponding boundaries while all other boundaries are insulating. The calculations are carried out for two types of structures.

First, the calculations are carried out for metamaterial Hall bars composed of a finite numbers of unit cells. Here, a current, I, is prescribed and the corresponding Hall voltage, U_H, is determined. From the Hall voltage, one

[1] I am assuming that the unit cell is centered around the origin, i.e., that it is given by $\left[-\frac{a}{2}, \frac{a}{2}\right)^3$.

can, for a long metamaterial Hall bar, estimate the effective Hall coefficient, A_{H}^{*}, assuming an isotropic metamaterial, as

$$A_{\mathrm{H}}^{*} = \frac{U_{\mathrm{H}} L_z}{I b_z}, \tag{3.14}$$

where L_z is the thickness of the Hall bar. Hence, these calculations allow to make a statement whether a certain number of unit cells is sufficient to approach the continuous case. This aspect will not be discussed much further, as in general, the results for finite structures and periodic boundary conditions are in very good agreement already for relatively small numbers of unit cells, and certainly for the typical numbers considered in the subsequent chapters.

Second, such calculations are performed for the parts of the unit cell that are crucial for obtaining the desired effective properties. Such calculations are an important tool for understanding the underlying mechanisms and for creating novel structures. In particular, it is often instructive to look at the perturbation in the electric potential that is caused by the magnetic field, i.e., to consider the quantity $\phi(b_z = b_0) - \phi(b_z = 0)$, which I am referring to as the Hall potential.

3.2 Sign-inversion of the effective Hall coefficient

In order to calculate the effective electrical properties of a given microstructure, one could, in principle, solve Equation 3.2 for two values of the magnetic field and extract the effective zero magnetic-field conductivity tensor and the effective Hall tensor. However, this is unsatisfactory as it does not offer insight into the underlying physical mechanisms, which makes it very hard to solve the inverse problem, i.e., to come up with a microstructure for a given set of effective parameters. Instead, a simple and intuitive description is required.

In the following, I will introduce two different types of metamaterials exhibiting a sign inversion of the effective Hall coefficient. These two metamaterials correspond to two such ways of approaching the problem. The first approach is based on Equation 3.11, which is the result of a perturbative treatment of the problem and led to a chainmail-like metamaterial design. The second approach is based on describing the metamaterial as a set of local Hall elements that are connected in a specific way. Both approaches are closely connected. For example, I have used Equation 3.11 to conceptually decompose metamaterials into sets of local Hall elements.

3.2.1 The two-dimensional problem

Before considering three-dimensional Hall metamaterials, I will briefly discuss the two-dimensional problem, in which case the effective properties are heavily restricted.

It was shown by Briane and Milton that the effective Hall coefficient of a two-dimensional metamaterial cannot be sign-inverted [62]. More precisely, in two dimensions, the effective Hall coefficient lies within the range of Hall coefficients of the constituent materials [62]. This result is based on an earlier result by Alessandrini and Nesi, who showed that, in two dimensions, the determinant of the matrix-valued electric field (the corrector), $\det(\boldsymbol{E})$, is positive almost everywhere [74].

Furthermore, it should be noted that it was also shown that the positivity of the determinant holds for laminates in any dimension [75], which implies that the effective Hall coefficient of a laminate cannot be sign-inverted,

independently of the dimension. In any attempt to find a structure exhibiting a sign-inversion, one has to consider more general geometries. The three-dimensional metamaterial structures exhibiting a sign-inversion of the effective Hall coefficient, which will be introduced in the following sections, are indeed far more complicated than laminates.

Intuitively, Hall metamaterials can be seen as periodic networks of resistors and Hall elements. Whether the effective Hall coefficient can be sign-inverted becomes a question of whether the elements can be connected in a corresponding way. In two dimensions, the number of possible connections is heavily restricted, as they have to be made in plane and are not allowed to cross. In three dimensions, this restriction is lifted and out-of-plane connections can be made. This additional freedom is crucial for the sign-inversion of the effective Hall coefficient.

These considerations are in interesting analogy to the four color map theorem, which states that, in two dimensions, every map can be colored with four colors such that no two regions sharing a boundary have the same color [76]. The problem is usually translated to graph theory. Each region is represented by a vertex. An edge between two vertices corresponds to a boundary between two regions. Obviously, the vertices can not be arbitrary, but are not allowed to cross. This restriction ultimately leads to the result that four colors suffice. Interestingly, in three dimensions, infinitely many different colors are needed. For every integer number n, one can give an example of n regions with each of the regions sharing a boundary with all other regions. Again, it is the additional freedom in making connections in the higher dimension that leads to a drastically different result.

3.2.2 Chainmail-like metamaterials

In the following, I will discuss the sign-inversion of the effective Hall coefficient in three-dimensional chainmail-like metamaterials. A brief history of these metamaterials, including my own work, is given in [77]. The first such metamaterial was studied by Marc Briane and Graeme Milton [55]. Their structure originated from an earlier design, a three-dimensional metamaterial composed of chains of interlinked electrically-conducting tori [75]. These chains have the property that the determinant of the matrix-valued

electric field, $\det(\boldsymbol{E})$, turns negative in between the intertwined tori. This determinant is closely linked to the cofactor of the matrix valued current density, which appears in the expression for the effective Hall coefficient, Equation 3.11. As mentioned above, the positivity of the determinant in two dimensions as well as in laminates is the reason why the corresponding effective Hall coefficients cannot be sign-inverted.

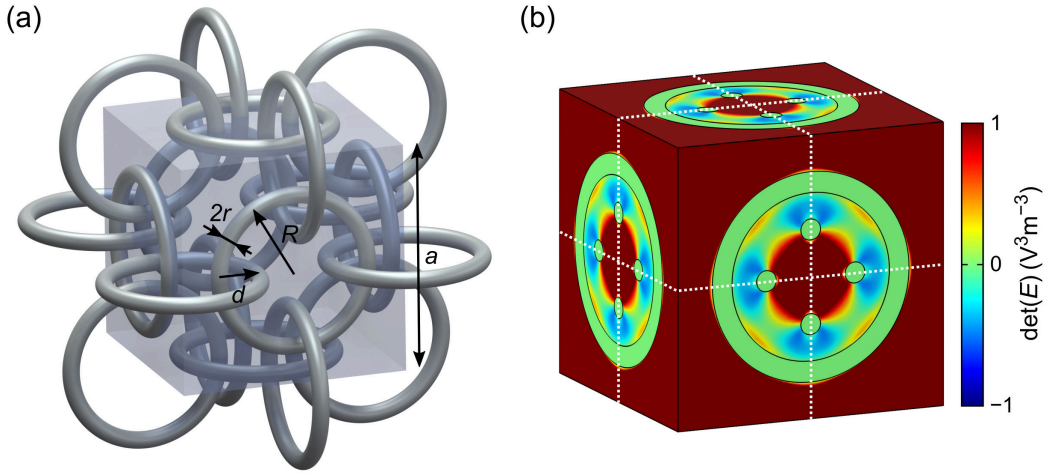

Figure 3.1: (a) Illustration of an extended unit cell of the three-dimensional version of the metamaterial introduced in [75]. The structure is composed of interlinked electrically-conducting tori embedded in a weakly conducting surrounding medium. (b) Corresponding numerical calculation of the determinant of the matrix-valued electric field. In between the interlinked tori, the determinant turns negative, which is a key step towards a sign-inversion of the effective Hall coefficient. On the white dashed lines, the sign of the determinant is identical to the sign of the corresponding diagonal cofactor. Parameters are $R = 36\,\mu\text{m}$, $r = 4\,\mu\text{m}$, $d = -18\,\mu\text{m}$, $\sigma_0^{\text{Tor.}} = 200\,\text{S}\,\text{m}^{-1}$, and $\sigma_0^{\text{Surr.}} = 0.2\,\mu\text{m}$. Adapted from [14].

A unit cell of the three-dimensional version of the metamaterial is shown in Figure 3.1. The tori and the surrounding material have zero magnetic-field conductivity $\sigma_0^{\text{Tor.}}$ and $\sigma_0^{\text{Surr.}}$, respectively. Interestingly, the three-dimensional version was suggested by a chainmail artist, Dylon Whyte [77]. The specific arrangement of tori corresponds to a Japanese chainmail pattern. Alterna-

tively, one can think of the structure as a crystal with a body-centered cubic lattice and the three-atomic basis [14],

$$\mathrm{T}_x : (a/2, 0, 0)^\mathsf{T}\,,\ \mathrm{T}_y : (0, a/2, 0)^\mathsf{T}\,,\ \mathrm{T}_z : (0, 0, a/2)^\mathsf{T}\,. \tag{3.15}$$

Here, a is the lattice constant and T_x, T_y, and T_z are tori with the subscript indicating the corresponding axis.

A corresponding numerical calculation of the determinant of the matrix-valued electric field, $\det(\boldsymbol{E})$, is shown in Figure 3.1. Clearly, in between the intertwined tori, the determinant is negative. For all points on certain lines, schematically indicated in Figure 3.1(b) and Figure 3.2(a), using symmetry considerations, it can be shown that the sign of $\det(\boldsymbol{E})$ is identical to the sign of the corresponding diagonal cofactor [14, 55].

Hence, it is not only $\det(\boldsymbol{E})$ that turns negative in between the interlinked tori, but also the corresponding cofactor. A numerical calculation of the cofactor trace, $C_{11} + C_{22} + C_{33}$, is shown in Figure 3.2. The three components, C_{11}, C_{22}, and C_{33} correspond to magnetic fields along the x-, y-, and z-direction, respectively. The trace, therefore, reflects the cubic symmetry of the structure. As expected, the cofactor trace is negative in between the interlinked tori.

One can now assign different Hall coefficients to different parts of the structure. If this assignment is performed such that the cubic symmetry of the material is preserved, it follows that the effective Hall tensor is isotropic, i.e., it reduces to an effective Hall coefficient, compare section 2.2. Furthermore, if one chooses the microscopic Hall coefficient such that it is nonzero only in the regions of negative cofactor trace, it follows from Equation 3.11, which represents a weighted average of the microscopic Hall coefficient, that the effective Hall coefficient of the metamaterial is sign-inverted. An illustration of a corresponding unit cell is shown in Figure 3.2. Small black spheres are placed in between the interlinked tori, where the cofactor trace turns negative. These spheres have the same zero-magnetic field conductivity as the surrounding material and nonzero Hall coefficient. Hence, one obtains a three-constituent metamaterial with a sign-inverted effective Hall coefficient.

Realizing such complicated microstructures would be extremely challenging, especially on the microscale. It is, however, possible to vastly simplify

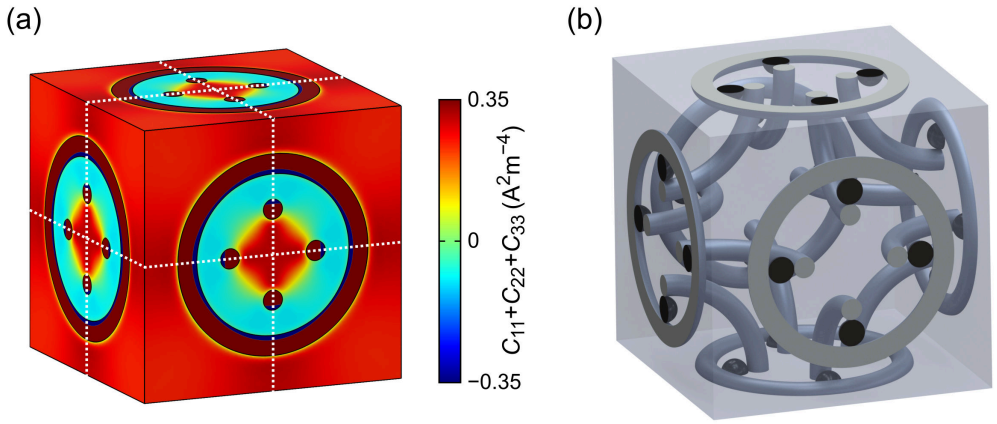

Figure 3.2: (a) Numerical calculation of the cofactor trace, $C_{11} + C_{22} + C_{33}$, for the unit cell of the metamaterial shown in Figure 3.1. In between the interlinked tori, the cofactor trace is negative. This property is connected to the change of sign of the determinant of the matrix-valued electric field, see Figure 3.1. For all points on the white dashed lines, it can be shown that the sign of $\det(\boldsymbol{E})$ is identical to the sign of the corresponding diagonal cofactor. Parameters are as in Figure 3.1. (b) Illustration of a unit cell of the three constituent metamaterial introduced in [55]. Small semiconducting spheres, shown in black, are placed in between the interlinked tori. These spheres have the same conductivity as the surrounding material. Furthermore, they are the only parts of the structure with nonzero Hall coefficient. As the spheres are placed in regions of negative cofactor trace, the effective Hall coefficient of the metamaterial is sign-inverted. Adapted from [14, 71].

the structure, which led to single-constituent porous metamaterials that show the same effect [71]. A drawback of these simplified structures is that they are not amenable to the mathematical treatment used in the original publication [55]. Instead, they were studied using numerical calculations for finite metamaterial Hall bars [71], which were initially performed by Muamer Kadic. Later, I have carried out calculations for finite structures as well as for infinitely extended crystals. Two simplifications were made: First, the surrounding material was replaced by an insulator, which might be, e.g., vacuum or air. Additionally, the semiconducting spheres were replaced by cylinder segments. The cylinder segments and the tori are made from the same material with finite Hall coefficient A_{H}^0. As a result, one obtains a

single-constituent porous metamaterial[2]. An illustration of a unit cell of this metamaterial is shown in Figure 3.3. The distance parameter, d, controls the relative positions of the tori. A negative value of d corresponds to interlinked tori while a positive value of d corresponds to non-interlinked tori.

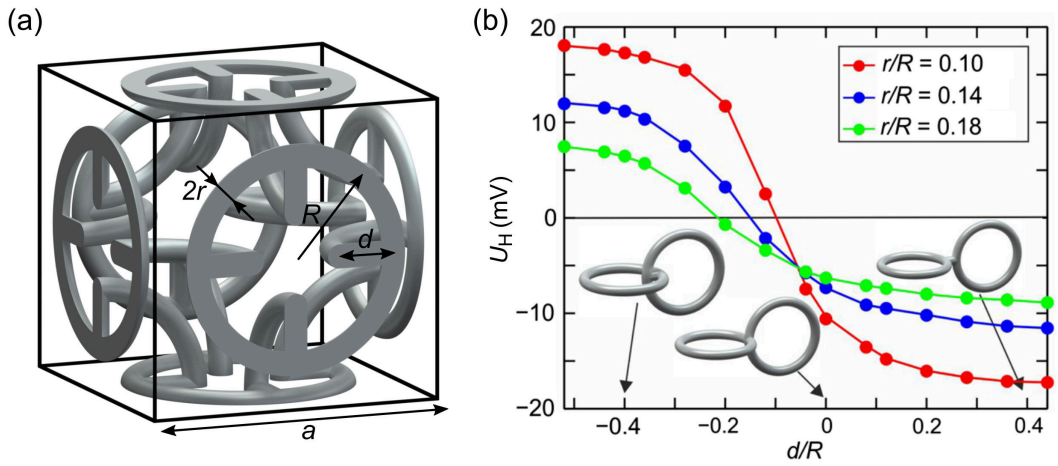

Figure 3.3: (a) Schematic illustration of a unit cell of the single-constituent porous metamaterial introduced in [71], which is based on the three-constituent design shown in Figure 3.2(b). The distance parameter, d, can take positive and negative values. The configuration of interlinked tori shown here corresponds to a negative value of d. (b) Numerical calculation of the Hall voltage for a metamaterial Hall bar composed of $11 \times 5 \times 1$ of such unit cells. Results for three different values of r/R are shown. The Hall coefficient of the constituent material is negative, $A_H^0 = -624 \cdot 10^{-6}\,\mathrm{m^3\,A^{-1}\,s^{-1}}$. For negative values of d with large enough modulus, the Hall voltage and, hence, the effective Hall coefficient is positive and, therefore, sign-inverted. The zero crossing depends on the value of r/R. Parameters are $R = 10\,\mu\mathrm{m}$, $\sigma_0 = 200\,\mathrm{S\,m^{-1}}$, and $b_z = 1\,\mathrm{T}$. Adapted from [71].

Consider a metamaterial Hall bar composed of $N_x \times N_y \times N_z = 11 \times 5 \times 1$ of these unit cells. Numerical calculations for such Hall bars were carried out as described in section 3.1. The resulting Hall voltage, U_H, versus distance

[2] In principle, one could assign different Hall coefficients to different parts of the structure, which would lead to a structure with several constituent materials, see [14].

parameter, d, is shown in Figure 3.3(b). By adjusting the distance parameter, the Hall voltage and, hence, the effective Hall coefficient can be tuned. For negative values of d with large enough modulus, the effective Hall coefficient is sign-inverted. The zero crossing shifts depending on the radius r. Furthermore, for smaller values of r, the effective Hall coefficient becomes larger.

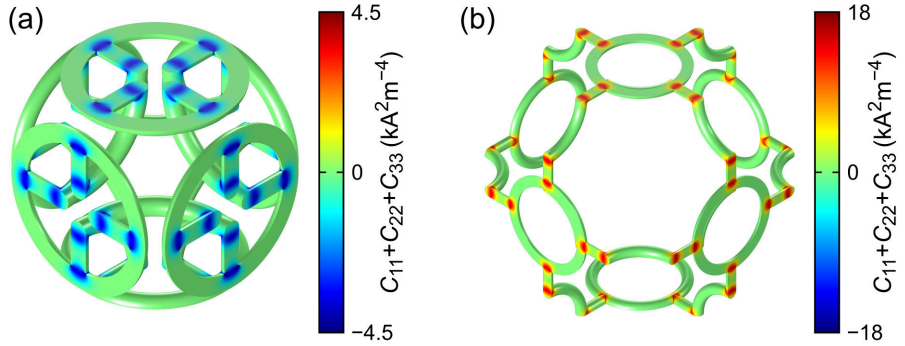

Figure 3.4: Numerical calculation of the cofactor trace, $C_{11} + C_{22} + C_{33}$, for two different values of the distance parameter. (a) Unit cell corresponding to $d = -34\,\mu\text{m}$. The volume average of the cofactor trace is negative. The corresponding effective Hall coefficient is sign-inverted. (b) Unit cell corresponding to $d = 34\,\mu\text{m}$. The volume average of the cofactor is positive. The corresponding effective Hall coefficient is not sign-inverted. Parameters are $R = 48\,\mu\text{m}$, $r = 6\,\mu\text{m}$, and $\sigma_0 = 200\,\text{S}\,\text{m}^{-1}$. Adapted from [14].

Numerical calculations for periodic boundary conditions are shown in Figure 3.4. Results for the cofactor trace, $C_{11} + C_{22} + C_{33}$, corresponding to two values of the distance parameter, $d = -34\,\mu\text{m}$ and $d = 34\,\mu\text{m}$, are depicted. For the structure corresponding to $d = -34\,\mu\text{m}$, the volume average is negative and, hence, the effective Hall coefficient is sign-inverted. More precisely, one obtains $A_{\text{H}}^{*} = -5.73 A_{\text{H}}^{0}$ [14]. For the structure corresponding to $d = 34\,\mu\text{m}$, the volume average is positive which implies that the effective Hall coefficient is not sign-inverted. In both cases, the cofactor is significantly larger than zero only in the regions where the cylinder and tori cross. While local Hall voltages appear in all parts of the structure in which a current flows, these are the only regions that contribute to the macroscopically mea-

surable Hall voltage and, hence, to the effective Hall coefficient. Therefore, these regions might be seen as local Hall elements that connected in a specific way. As I will show in the subsequent sections, this interpretation proves most useful in the design and analysis of Hall metamaterials.

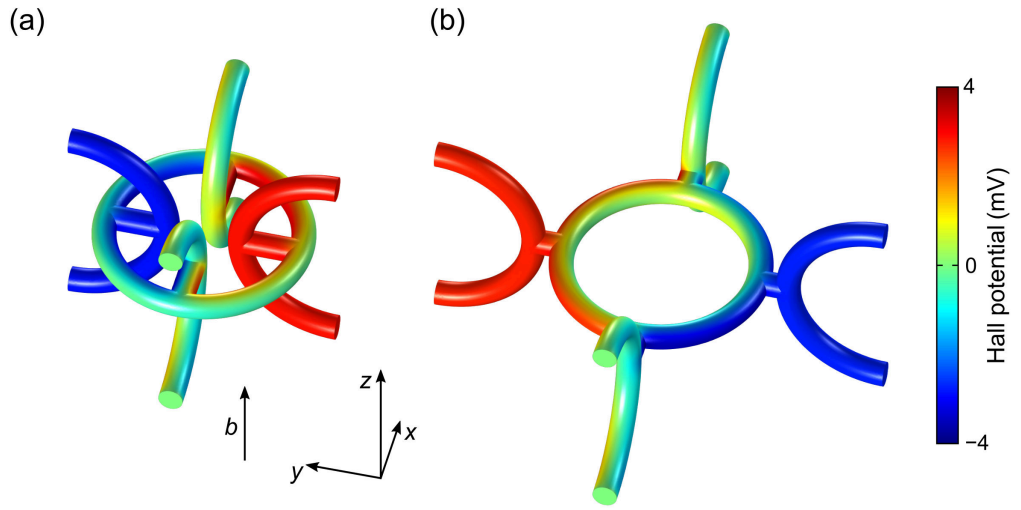

Figure 3.5: Numerical calculations of the Hall potential, i.e., the perturbation in the electric potential due to a magnetic field, for a unit cell of a single layer of the chainmail-inspired metamaterial and two different values of the distance parameter, d. Results for $d = 12\,\mu\text{m}$ and $d = -20\,\mu\text{m}$ are shown in (a) and (b), respectively. A current along $\hat{\boldsymbol{x}}$ of $I_x = 100\,\mu\text{A}$ was imposed using a constant potential on the corresponding boundaries. The magnetic field is along $\hat{\boldsymbol{z}}$. Parameters are $R = 36\,\mu\text{m}$, $r = 6\,\mu\text{m}$, $\sigma_0 = 200\,\text{S}\,\text{m}^{-1}$, $A_\text{H}^0 = -624 \cdot 10^{-6}\,\text{m}^3\,\text{A}^{-1}\,\text{s}^{-1}$, and $b_z = 1\,\text{T}$. Adapted from [14].

For certain directions of the magnetic field and current flow, one can give an intuitive description of the mechanism underlying the sign-inversion [73]. Consider a single layer of the chainmail-inspired metamaterial. Corresponding numerical calculations for a unit cell of such a structure and two different values of the distance parameter are shown in Figure 3.5. Assume that the magnetic field is pointing in the z-direction and a current is flowing in the x-direction. Via the tori in the xz-plane, the current is injected into the torus in the xy-plane. In this torus, local Hall voltages appear. These are picked-up

by the tori in the yz-plane. For a negative value of d (with large enough modulus), the potential is picked-up on the inner boundary of the torus, which leads to an inversion of the Hall voltage. For a positive value of d, the electric potential is picked-up on the outer boundary, and the Hall voltage is not inverted. Interestingly, in order to obtain a sign-inversion, both the injection of the current and the pick-up of the potential has to be performed via the inner boundary of the torus. If the current was injected on the outer boundary and the potential was picked-up on the inner boundary or vice versa, the picked-up Hall voltage and, hence, the effective Hall coefficient would be zero. While this interpretation nicely explains the sign-inversion of the effective Hall coefficient, the situation can be much more complex for other directions of current flow and magnetic field.

It should be mentioned that this intuitive discussion shows a relation of the sign-inversion of the effective Hall coefficient in chainmail-like metamaterials to the sign-inversion of the Hall voltage in so-called anti-Hall bars [15], which were discussed in section 2.1. This relation led to a series of comments [78, 79] and replies [80, 81], see also [14]. In some sense, the tori can be seen as three-dimensional versions of anti-Hall bars. However, it should be emphasized that my work is concerned with effective materials. While the structures presented in this thesis strictly qualify as effective materials, this is certainly not the case for anti-Hall bars. Nevertheless, the sign-inversion of a (local) Hall voltage can serve as a basis for a material with a sign-inverted effective Hall coefficient.

One of the goals of my thesis was the experimental confirmation of the sign-inversion of the effective Hall coefficient in chainmail-like metamaterials. In the experiments, see chapters 5 and 6, a structure that is slightly different was realized on the microscale. In a first step, insulating polymer scaffolds were fabricated. In a second step, these structures were conformally coated with a thin semiconducting layer. Such a fabrication process leads to structures that are hollow from the viewpoint of electrical conductivity. In order to determine whether this change in geometry has an influence on the effect, corresponding numerical calculations were carried out, for both finite [71] and infinitely-extended [14] crystals. The main result of these calculations is that the qualitative behavior of the structure is not affected. The modulus of the effective Hall coefficient, however, does change. A numerical calculation

of the cofactor trace for the hollow version of the single-constituent porous chainmail-like metamaterial is shown in Figure 3.6(a).

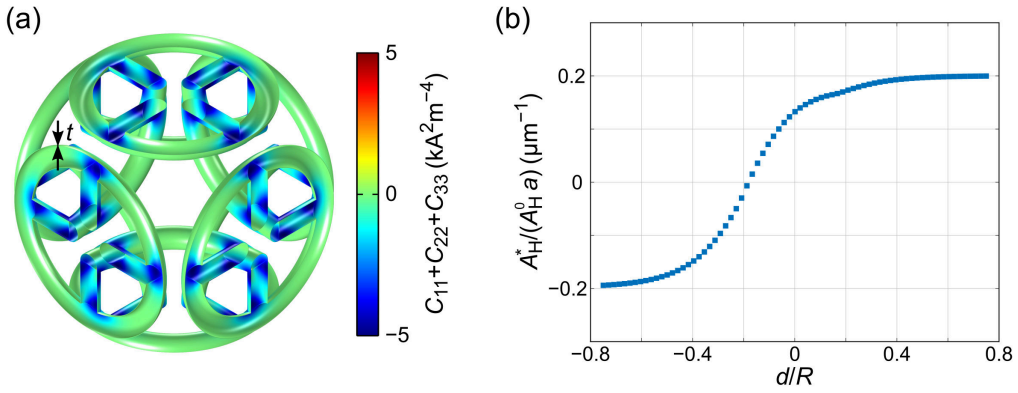

Figure 3.6: (a) Numerical calculation of the cofactor trace, $C_{11} + C_{22} + C_{33}$, for the hollow version of the chainmail-inspired metamaterial. Corresponding structures were realized experimentally by fabricating insulating polymer templates and coating them conformally with a semiconducting layer. The volume average is negative which leads to a sign-inverted effective Hall coefficient. The thickness of the coating layer is $t = 185\,\text{nm}$. The distance parameter is $d = -34\,\mu\text{m}$. The other parameters are $r = 6\,\mu\text{m}$, $R = 48\,\mu\text{m}$, and $\sigma_0^0 = 200\,\text{S}\,\text{m}^{-1}$. (b) Numerical calculation of the effective Hall coefficient versus d/R. By adjusting the distance parameter, the effective Hall coefficient can be tuned. For large values of $|d/R|$, the effective Hall coefficient saturates. The thickness of the coating layer is $t = 1\,\mu\text{m}$. The other parameters are as in (a). Adapted from [14].

For this choice of parameters, the average of the cofactor trace is negative and, hence, the effective Hall coefficient of the metamaterial is sign-inverted. As for the non-hollow version, the main contribution to the sign-inversion is due to the regions where the cylinders and tori intersect. However, the effective Hall coefficient is much larger than the one obtained for the non-hollow case, which is due to the confinement of the current to a thinner layer. By varying the distance parameter, the effective Hall coefficient can be continuously tuned from positive to negative values, compare Figure 3.6(b). As for the non-hollow structures, the zero crossing shifts towards the left for larger values of the minor radius, r, not depicted. As long as r is comparably

small, the effective Hall coefficient saturates for distance parameters with large modulus.

An empirical estimate of the effective Hall coefficient of the hollow structure can be derived from further numerical calculations [14]. It is given by

$$|A_{\mathrm{H}}^{*}| \approx 0.2\frac{a}{t}\left|A_{\mathrm{H}}^{0}\right|, \tag{3.16}$$

where I am assuming that the minor radius, r, is small and that the modulus of the distance parameter, d, is large, i.e., that the effective Hall coefficient is in the saturated regime, compare Figure 3.6. Instead of using a fit to the numerical results, one can alternatively model the structure as a network of Hall voltage sources [14], which results in similar estimates. This procedure is analogous to the one I have used for estimating the effective Hall coefficient of certain anisotropic structures, see section 3.3.

By reducing the thickness t, the Hall coefficient can be made arbitrarily large. Equation 3.16 implies that $A_{\mathrm{H}} \to \infty$ as $\frac{t}{a} \to 0$, which means that the effective Hall coefficient becomes unbounded. This property of the metamaterial is related to the fact that it is porous, i.e., that one of the constituent materials is an insulator, which is further discussed in section 3.4, in which I am elaborating on bounds on the effective Hall coefficient and related parameters.

This increase in effective Hall coefficient can be understood intuitively. A reduction of the thickness t leads to a confinement of the electric current to a thinner layer within the unit cell. As a consequence, a corresponding metamaterial Hall bar effectively acts like a much thinner Hall bar and the effective Hall coefficient become larger. Furthermore, as discussed above, the sign of the Hall coefficient can be chosen by adjusting d. Hence, by varying d and t simultaneously, the chainmail-like hollow metamaterial allows to realize any arbitrary value of the effective Hall coefficient.

3.2.3 A different way of inverting the effective Hall coefficient

As already discussed, Hall metamaterials may be seen as networks of resistors and Hall elements. In this sense, the realization of an effective Hall tensor corresponds to the choice of a specific connection of Hall elements.

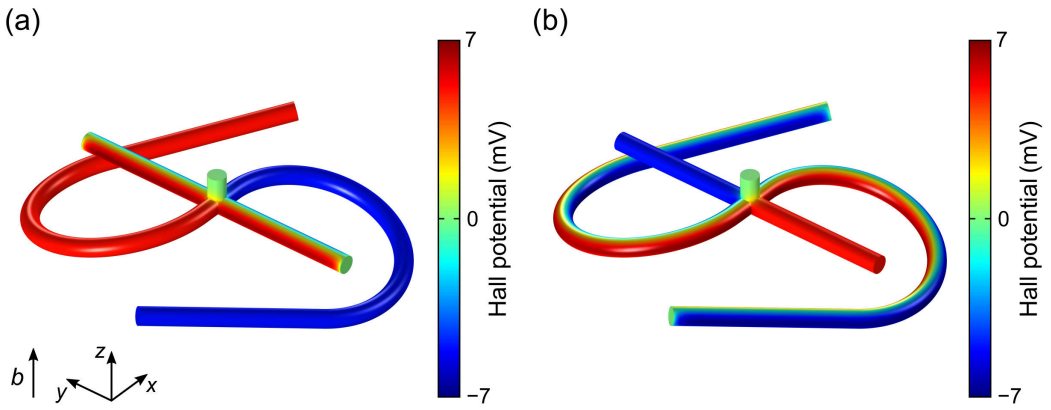

Figure 3.7: Numerical calculation of the Hall potential, i.e., the perturbation in the electric potential due to a magnetic field, for a structure inverting a local Hall voltage. This inversion is independent of the orientation of current flow in the xy-plane. (a) Current flow along $\hat{\boldsymbol{y}}$. The inversion of the Hall voltage is due to a inversion of the pick-up. (b) Current flow along $\hat{\boldsymbol{x}}$. The inversion of the Hall voltage is due to a local inversion of the current flow direction. The current flow of $I = 100\,\mu\text{A}$ is imposed by a constant potential, all other boundaries are insulating. Parameters are, compare Figure 3.8, $R_1 = 30\,\mu\text{m}$, $r = 3\,\mu\text{m}$, $\alpha = 15°$, $\beta = 220°$, $A_\text{H}^0 = -624 \cdot 10^{-6}\,\text{m}^3\,\text{A}^{-1}\,\text{s}^{-1}$, and $b = 1\,\text{T}$. Adapted from [14].

Based on this concept, a sign-inversion of the effective Hall coefficient can be achieved by connecting Hall elements in such a way that the corresponding local Hall voltages are inverted [14]. Numerical calculations for a structure accomplishing such an inversion of a local Hall voltage are shown in Figure 3.7. The constituent material is isotropic with zero magnetic-field conductivity σ_0^0 and Hall coefficient A_H^0. The inversion can be understood intuitively and is independent of the direction of current flow in the xy-plane. Assume that the magnetic field is along $\hat{\boldsymbol{z}}$. A current flowing in the y-direction generates a local Hall voltage in the straight cylinder. The electric potential is picked up at the cross and guided by the bent segments, resulting in an inverted Hall voltage. A current flowing in the x-direction on the other hand, is locally inverted, i.e., flowing in the $-\hat{\boldsymbol{x}}$ direction through the cross, leading again to an inverted Hall voltage. As mentioned above, one can use this behavior as a starting point for a metamaterial with a sign-inverted

effective Hall coefficient. Arranging six such structures on the faces of a cube and connecting them via torus segments leads to the metamaterial unit cell shown in Figure 3.8, which was introduced in [14]. The structure has the cubic crystallographic point group 32 and, hence, the effective zero magnetic-field conductivity tensor and the effective Hall tensor are isotropic by symmetry, compare section 2.2.

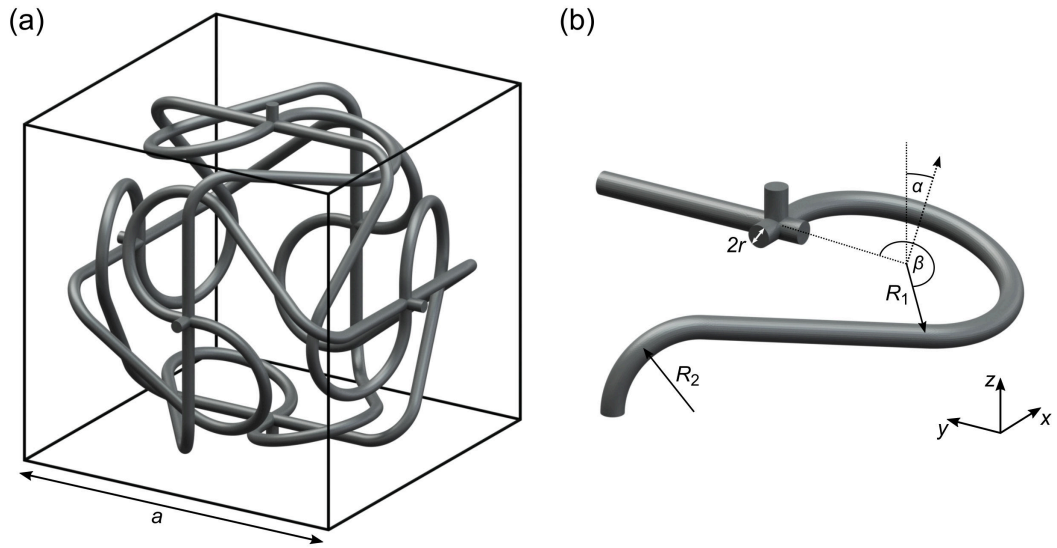

Figure 3.8: (a) Illustration of a unit cell of a metamaterial exhibiting a sign-inversion of the effective Hall coefficient that is conceptually based on the inversion of local Hall voltages. The metamaterial is composed of six elements as the one shown in Figure 3.7, which are arranged on the faces of a cube. (b) Parametrization of the structure. Adapted from [14].

A numerical calculation of the cofactor C_{33}, corresponding to a magnetic field along the z-direction, for this structure is shown in Figure 3.9. Details of the numerical calculation procedure were given in section 3.1. The cofactor is significantly different from zero only in and close to the crosses, which can, therefore, in agreement with our previous considerations, be seen as local Hall elements. All other parts of the structure, where C_{33} is close to zero, can be seen as a specific connection of these elements. Only four of the six crosses actually contribute to the sign-inversion. For the crosses on the

top and the bottom face (parallel to the xy-plane), which contribute to the effect, the corresponding interpretation was already given above, compare Figure 3.7.

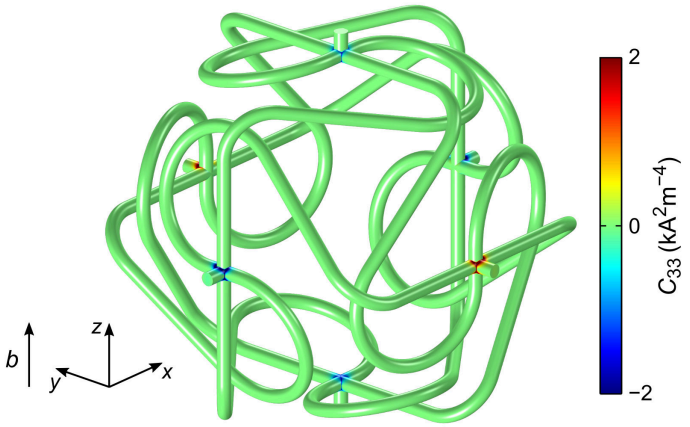

Figure 3.9: Numerical calculation of the cofactor C_{33}, corresponding to a magnetic field along $\hat{z}$, for the metamaterial unit cell shown in Figure 3.9. The cofactor is significantly different from zero only at the six crosses. Not all of the crosses contribute to the sign-inversion. The effective electrical properties of the structure are isotropic by symmetry. Parameters are $R_2 = 20\,\mu\text{m}$, $a = 170\,\mu\text{m}$, and $\sigma_0^0 = 200\,\text{S}\,\text{m}^{-1}$. All other parameters are as in Figure 3.7. Adapted from [14].

For the crosses on the vertical faces, the interpretation is more difficult. Assume that the current flows in the x-direction. Local Hall voltages appear in the crosses. The pick-up of these voltages is reversed for the crosses parallel to the yz-plane, where the cofactor is negative, but not for those parallel to the xz-plane, where the cofactor is positive. A similar consideration can be made for a current flow along $\hat{y}$. In spite of this counteracting effect, the volume average of the cofactor is negative, which leads to a sign-inverted effective Hall coefficient. More precisely, a numerical evaluation of Equation 3.11 yields $A_\text{H}^* = -3.43 A_\text{H}^0$ [14].

3.3 Anisotropic structures

Fundamentals

So far, I have considered isotropic materials, in which case, the material is characterized by a scalar Hall coefficient. In general, however, the material may be anisotropic, being characterized by the nine independent components of the Hall tensor. Such anisotropic effective properties lead to very interesting effects. For example, depending on the direction of current flow, they lead to components of the Hall electric field parallel to the magnetic field[3]. Consider for example the following Hall tensor,

$$\boldsymbol{A}_{\mathrm{H}} = \begin{pmatrix} 0 & 0 & 0 \\ 0 & 0 & A_{23} \\ 0 & 0 & 0 \end{pmatrix}, \tag{3.17}$$

for a current $\boldsymbol{j} = j_x \hat{\boldsymbol{x}}$ and magnetic field $\boldsymbol{b} = b_z \hat{\boldsymbol{z}}$. Using Equation 2.61, one obtains for the Hall electric field,

$$\boldsymbol{e}_{\mathrm{H}} = -A_{23} j_x b_z \hat{\boldsymbol{z}}. \tag{3.18}$$

The Hall electric field is along $\hat{\boldsymbol{z}}$, i.e., parallel to the magnetic field. This appearance of a component of the Hall electric field parallel to $\boldsymbol{b}$ is the so-called parallel Hall effect [72]. In sharp contrast, in isotropic materials, the Hall electric field is always perpendicular to the magnetic field.

In the following, I will try to develop a systematic understanding of the anisotropic problem. As any tensor, the Hall tensor can be written as the sum of a symmetric and an anti-symmetric tensor. A (real) symmetric rank-two tensor is diagonizable via an orthogonal transformation, i.e., one can find a set of orthogonal axes, the so called principal axes, regarding to which it is diagonal. Its components with regard to these axes are referred to as its

[3] As a clarification, it should be mentioned that I am using the word parallel in the sense that two nonzero vectors, $\boldsymbol{a}$ and $\boldsymbol{b}$, are parallel iff their cross product is equal to zero, $\boldsymbol{a} \times \boldsymbol{b} = 0$. This includes the case of $\boldsymbol{a}$ and $\boldsymbol{b}$ pointing in opposite directions.

principal values. For a diagonal Hall tensor, Equation 2.61 becomes

$$\boldsymbol{e}_{\mathrm{H}} = \begin{pmatrix} A_{11} b_x \\ A_{22} b_y \\ A_{33} b_z \end{pmatrix} \times \begin{pmatrix} j_x \\ j_y \\ j_z \end{pmatrix}, \tag{3.19}$$

which implies that the principal components can be seen as weights to the corresponding components of the magnetic field.

Symmetric rank-two tensors can be visualized as a quadric [27]. In the case of a positive definite rank-two tensor, i.e., in the case of all principal values being positive, the quadric is an ellipsoid, with a well-known example being the moment of inertia tensor. Some or all of the principal components of the symmetric part of the Hall tensor might be negative and, therefore, the corresponding quadric is not necessarily an ellipsoid, but might be, e.g., an hyperboloid.

Any antisymmetric rank-two tensor, and therefore, the antisymmetric part of the Hall tensor, can be seen as an axial vector, compare section 2.2. The correspondence is given by

$$\begin{pmatrix} a_1 \\ a_2 \\ a_3 \end{pmatrix} \longleftrightarrow \begin{pmatrix} 0 & a_3 & -a_2 \\ -a_3 & 0 & a_1 \\ a_2 & -a_1 & 0 \end{pmatrix}. \tag{3.20}$$

Hence, the Hall electric field is given by, using Graßmann's identity,

$$\boldsymbol{e}_{\mathrm{H}} = (\boldsymbol{A}_{\mathrm{H}} \boldsymbol{b}) \times \boldsymbol{j} = -(\boldsymbol{a}_{\mathrm{H}} \times \boldsymbol{b}) \times \boldsymbol{j} = -\boldsymbol{b}(\boldsymbol{a}_{\mathrm{H}} \cdot \boldsymbol{j}) + \boldsymbol{a}_{\mathrm{H}}(\boldsymbol{b} \cdot \boldsymbol{j}), \tag{3.21}$$

where $\boldsymbol{a}_{\mathrm{H}}$ is the axial vector corresponding to the antisymmetric part of the Hall tensor.

The component of the magnetic field collinear with $\boldsymbol{a}_{\mathrm{H}}$ lead to a zero Hall electric field. Therefore, I will in the following, without loss of generality, assume that $\boldsymbol{b}$ lies in the plane perpendicular to $\boldsymbol{a}_{\mathrm{H}}$. Regarding the orientation of the current density, two cases can be distinguished. In the first case, the current density is parallel to $\boldsymbol{a}_{\mathrm{H}}$, leading to

$$\boldsymbol{e}_{\mathrm{H}} = \pm \boldsymbol{b} a_{\mathrm{H}} j, \tag{3.22}$$

where the sign depends on whether $\boldsymbol{j}$ points in the same (minus) or opposite (plus) direction as $\boldsymbol{a}_\mathrm{H}$. In this case, the Hall electric field is parallel to the magnetic field.

In the second case, the current density lies in the plane perpendicular to $\boldsymbol{a}_\mathrm{H}$, leading to

$$\boldsymbol{e}_\mathrm{H} = \boldsymbol{a}_\mathrm{H}(\boldsymbol{b} \cdot \boldsymbol{j}). \tag{3.23}$$

Here, the Hall electric field is parallel to $\boldsymbol{a}_\mathrm{H}$ with a maximum of the magnitude for $\boldsymbol{j}$ parallel to $\boldsymbol{b}$. All other orientations of the current density can be treated as a superposition.

Following these general considerations, I will come back to metamaterials, which make it possible to tailor the components of the Hall tensor by structure. In particular, it is possible to realize antisymmetric effective Hall tensors. For practical reasons, one usually starts from isotropic constituent materials.

Anisotropic Hall metamaterials

The first metamaterial with an anti-symmetric effective Hall tensor was proposed by Marc Briane and Graeme Milton [37]. A unit cell of their design is shown in Figure 3.10. It has three components: A highly conducting square cylinder, which is the only part of the structure with nonzero Hall coefficient, a spirally shaped part with a high conductivity in the yz-plane and a low conductivity in the x-direction, and a weakly conducting surrounding material. The anisotropic conductivity of the spirally shaped part can be mimicked by a laminate with isotropic components, in which case, the metamaterial would have four constituent materials.

In their analysis [37], Briane and Milton have shown that the effective Hall tensor of this metamaterial is asymptotically given by

$$\boldsymbol{A}^*_\mathrm{H} = \begin{pmatrix} 0 & 0 & 0 \\ 0 & 0 & A^*_{23} \\ 0 & -A^*_{23} & 0 \end{pmatrix}. \tag{3.24}$$

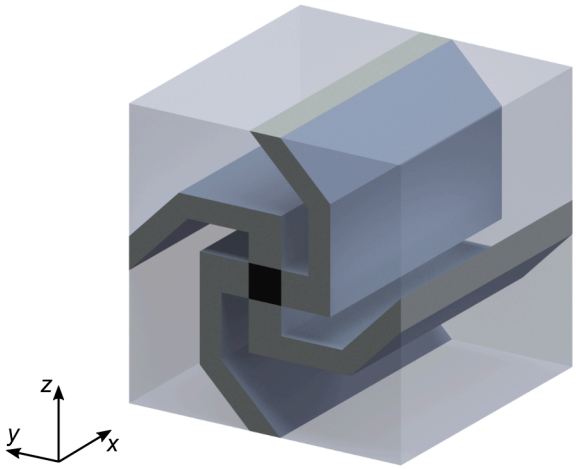

Figure 3.10: Illustration of a unit cell of the three-component metamaterial introduced in [37], the first metamaterial exhibiting an anti-symmetric effective Hall tensor. The structure consists of the following parts. A square cylinder made from a highly conducting material with nonzero Hall coefficient, shown in black. An spirally-shaped part made from an anisotropic material with a high conductivity in the yz-plane and a low conductivity in the x-direction, shown in grey, and a weakly-conducting surrounding. Reproduced from [14].

The corresponding axial vector is $\boldsymbol{a}_{\mathrm{H}}^{*} = (A_{23}^{*}, 0, 0)^{\intercal}$[4]. For a macroscopic current flow in the x-direction, i.e., along $\boldsymbol{a}_{\mathrm{H}}^{*}$, this effective Hall tensor corresponds to the following Hall electric field,

$$\boldsymbol{e}_{\mathrm{H}} = -A_{23}^{*} j_x \left(b_y \hat{\boldsymbol{y}} + b_z \hat{\boldsymbol{z}} \right). \tag{3.25}$$

Hence, the Hall electric field is parallel to the magnetic field as long as the magnetic field lies in the yz-plane.

The appearance of this effect can be understood intuitively. Assume that the current is flowing in the x-direction and the magnetic field points in the z-direction. Due to the choice of conductivities, the current will mainly flow through the square cylinder, where, as it has nonzero Hall coefficient a Hall voltage appears. The spirally shaped structure can be seen as pick-up wires,

[4] In [37], the authors have chosen the Hall coefficient of the square cylinder such that the effective Hall tensor is normalized, $A_{23}^{*} = 1$.

which guide the electric potential, such that the corresponding macroscopic Hall electric field is along the z-direction, i.e., parallel to the magnetic field.

Further insight can be gained via symmetry considerations. The structure has four-fold rotational symmetry about the x-axis. Its crystallographic point group is 4/m. As it turns out, this symmetry is ideally suited for the realization of antisymmetric effective Hall tensors. According to Table 2.1, it implies the following form of the effective Hall tensor (or any other rank-two tensor),

$$\boldsymbol{A}_{\mathrm{H}}^{*} = \begin{pmatrix} A_{11}^{*} & 0 & 0 \\ 0 & A_{22}^{*} & A_{23}^{*} \\ 0 & -A_{23}^{*} & A_{33}^{*} \end{pmatrix}. \tag{3.26}$$

Hence, it follows from symmetry that the off-diagonal part is anti-symmetric. However, symmetry makes no statement about the values of the remaining four components. To determine the actual values, one has to evaluate Equation 3.11. In order to obtain an anti-symmetric effective Hall tensor, the diagonal components must vanish, i.e., $A_{11}^{*} = A_{22}^{*} = A_{33}^{*} = 0$, which is not implied by symmetry but a result of a careful choice of structure.

While this three-constituent metamaterial is well-understood mathematically, the fabrication of such a structure seems to be out of reach. There are, however, similar single-constituent porous metamaterials with (almost) anti-symmetric effective Hall tensors that can actually be realized. A unit cell of such a metamaterial, which is based on the three-constituent design, is shown in Figure 3.11. It consists of a straight cylinder and two S-shaped elements, all made from the same isotropic material with nonzero Hall coefficient A_{H}^{0}. Again, one can consider the symmetry of the structure. Its crystallographic point group is the same as the one of the three-constituent structure, 4/m, which, therefore, leads to the same form of the effective Hall tensor, Equation 3.26. A numerical evaluation of Equation 3.11 yields [14], for the parameters given in Figure 3.11,

$$\boldsymbol{A}_{\mathrm{H}}^{*} = \begin{pmatrix} 0 & 0 & 0 \\ 0 & 0.05 & 8.81 \\ 0 & -8.81 & 0.05 \end{pmatrix} A_{\mathrm{H}}^{0}. \tag{3.27}$$

The underlying mechanism of the structure is very similar to the three-constituent case. Corresponding to the general discussion of antisymmetric

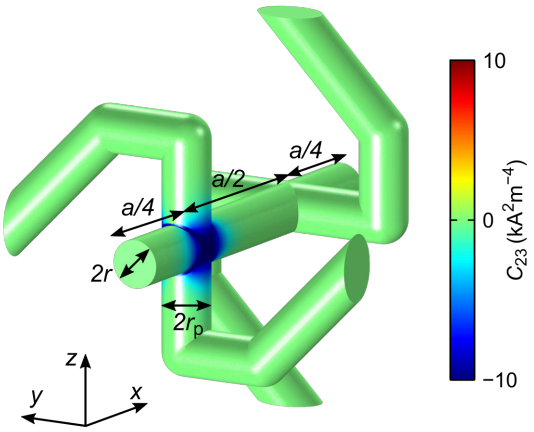

Figure 3.11: Numerical calculation of the cofactor C_{23} of the matrix-valued current density for a single-constituent metamaterial exhibiting an (almost) anti-symmetric Hall tensor. Assume that the magnetic field points in the y-direction. The Hall tensor component, A^*_{32}, which corresponds to C_{23}, relates a macroscopic current flow along the x- and y-direction to macroscopic Hall electric fields parallel to the y- and x-direction, respectively. The blue region indicates where the corresponding local Hall voltage is generated. Parameters are $a = 40\,\mu\text{m}$, $r = 2.5\,\mu\text{m}$, $b = 11\,\mu\text{m}$, and $c = 9\,\mu\text{m}$. Adapted from [14].

Hall tensors in the beginning of this section, one can distinguish two different cases of macroscopic current flow. Assume that the magnetic field points in the z-direction. A macroscopic current flow in the x-direction, i.e., parallel to $\boldsymbol{a}_\text{H}$, leads to an axial current flow through the straight cylinder in the center. Due to the magnetic field, a local Hall voltage, appears. The corresponding electric potential is picked-up by one of the two S-shaped structures and is guided such that it leads to a macroscopic Hall electric field in the z-direction, i.e., parallel to $\boldsymbol{b}$, compare Equation 3.22. An overall current flow in the z-direction, on the other hand, leads to a local current in the y-direction where it passes through the straight cylinder. There, a local Hall voltage appears. The straight cylinder picks-up the corresponding electric potential, which leads to a Hall electric field in the x-direction, i.e., parallel to $\boldsymbol{a}_\text{H}$, compare Equation 3.23. Note that I have assumed that the directions of macroscopic current flow and the magnetic field are parallel. If

the macroscopic current flow was along $\hat{\boldsymbol{y}}$, the current would flow through the other S-shaped element. The local direction of current flow in the straight cylinder would be parallel to $\boldsymbol{b}$ and, hence, there would be no macroscopic Hall electric field. Note that this intuitive discussion is in excellent agreement with the general treatment in the beginning of this section.

Controlling the orientation of the Hall electric field

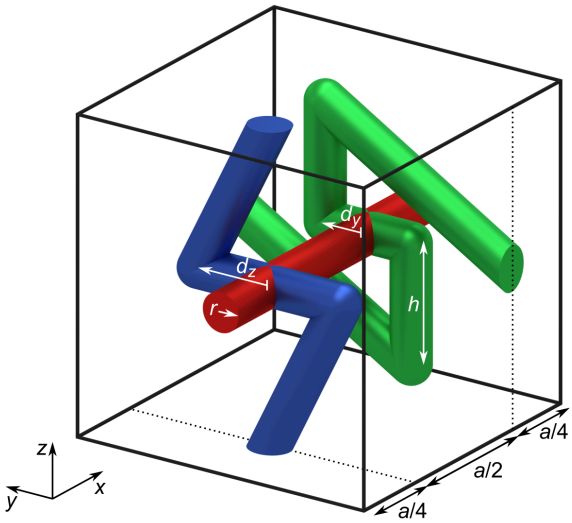

Figure 3.12: Illustration of the metamaterial unit cell introduced in [72]. The different parts of the structure, which are made from the same material with conductivity σ_0 and nonzero Hall coefficient A_{H}^0, are colored for clarity. The structure consists of a cylinder, shown in red, and two pick-up structures. The pick-up structure shown in blue corresponds to the parallel Hall voltage. The pick-up structure shown in green corresponds to the orthogonal Hall voltage. The material allows to tune the two Hall voltages by adjusting the parameters d_y and d_z. Adapted from [14].

Following three of my previous publications [14, 72, 82], I will now discuss a related metamaterial that, for given orientations of the magnetic field and current flow, allows to tune the angle between the macroscopic Hall

electric field and the magnetic field. I am assuming that the magnetic field is along $\hat{z}$ and the macroscopic current density is along $\hat{x}$. A unit cell of the metamaterial is shown in Figure 3.12. The single-constituent porous structure is quite similar to the one shown in Figure 3.11. The current is flowing through the cylinder shown in red, where it leads to a local Hall voltage. This voltage is picked-up by two structures. The first structure, shown in blue, leads to a macroscopic Hall electric field along the z-direction. The second structure, shown in green, leads to a Hall electric field along the y-direction. By adjusting the geometry parameters d_y and d_z, one can adjust this pick-up and, thereby, tune the two components of the macroscopic Hall electric field. These components, are experimentally accessible via the corresponding Hall voltages, U_{H}^{y} and U_{H}^{z}. Here, U_{H}^{y}, which corresponds to a Hall electric field that is orthogonal to $\boldsymbol{b}$, is the conventional "orthogonal" Hall voltage. On the other hand, U_{H}^{z}, which is zero for isotropic materials, corresponds to a macroscopic electric field parallel to $\boldsymbol{b}$ and I will therefore refer to it as the "parallel" Hall voltage.

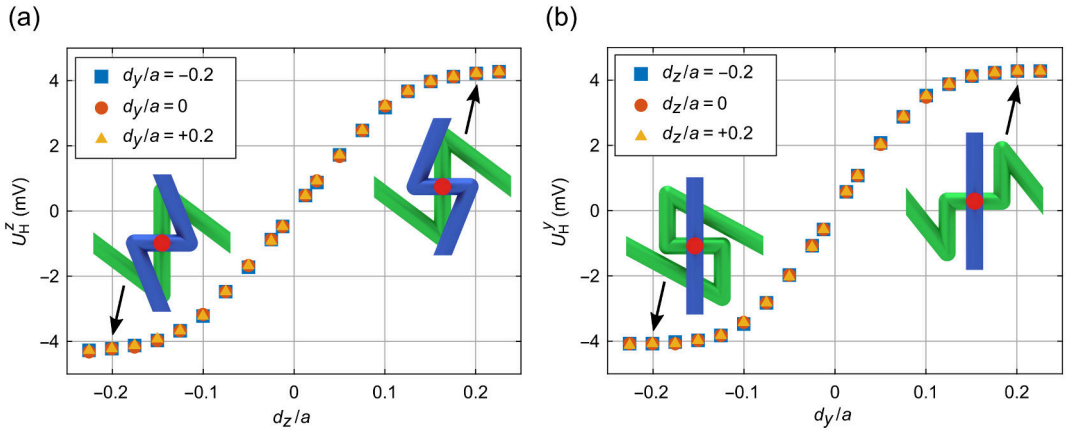

Figure 3.13: Numerical calculation of the parallel, U_{H}^{z}, and orthogonal, U_{H}^{y}, Hall voltage for a metamaterial Hall bar composed of $9 \times 3 \times 3$ unit cells as the one shown in Figure 3.12. A current flow of $I = 0.1\,\mathrm{mA}$ was imposed using constant potentials. All other boundaries are insulating. Parameters are $\sigma_0 = 200\,\mathrm{A\,V^{-1}\,m^{-1}}$, $A_{\mathrm{H}}^{0} = -624 \times 10^{-6}\,\mathrm{m^3\,A^{-1}\,s^{-1}}$, $b_z = 1\,\mathrm{T}$, $h = 15\,\mu\mathrm{m}$, $r = 2.5\,\mu\mathrm{m}$ and $a = 40\,\mu\mathrm{m}$. Adapted from [14].

For a metamaterial Hall bar made from $N_x \times N_y \times N_z = 9 \times 3 \times 3$ unit cells, the results of a numerical calculation of U_{H}^y and U_{H}^z in dependence of d_y and d_z are shown in Figure 3.13. The numerical calculations were performed as described in section 3.1. The results show that, within some range, U_{H}^y and U_{H}^z can be tuned continuously by adjusting d_y and d_z. For large values of $|d_y/a|$ and $|d_z/a|$, the Hall voltages saturate. Importantly, one can not only tune their magnitude but also their sign. As a result, any orientation of the macroscopic Hall electric field in the yz-plane can be realized. Furthermore, one has the convenient property that U_{H}^y (U_{H}^z) is independent of d_z (d_y). This makes sense, as the pick-up of the Hall voltage via each of the two structures is independent of the other one.

The two Hall voltages are directly connected to the two corresponding components of the Hall tensor. Using the constitutive relation, one obtains for a long Hall bar with dimensions L_x, L_y, and L_z,

$$U_{\mathrm{H}}^y = A_{33}^* \frac{b_z I}{L_z} \text{ and } U_{\mathrm{H}}^z = -A_{23}^* \frac{b_z I}{L_y}, \tag{3.28}$$

where I is the current flowing through the Hall bar along the x-direction.

The crystallographic point group of the structure is 2/m, which leads to the following form of the Hall tensor,

$$\boldsymbol{A}_{\mathrm{H}}^* = \begin{pmatrix} A_{11}^* & 0 & 0 \\ 0 & A_{22}^* & A_{23}^* \\ 0 & A_{32}^* & A_{33}^* \end{pmatrix}. \tag{3.29}$$

As described in section 5.1, see also [82], I have fabricated corresponding metamaterial Hall bars on the microscale and characterized them experimentally. As for the fabrication of the chainmail-inspired structures, I have employed a combination of three-dimensional laser lithography, which was used to fabricate electrically insulating polymer templates, and atomic-layer deposition, which was used to coat these templates with a thin semiconducting layer. This strategy inherently leads to structures that are hollow in an electrical sense. It should be emphasized that, as in the case of the chainmail-inspired structures, see section 3.2, this modification of the design does not change the qualitative behavior of the metamaterial.

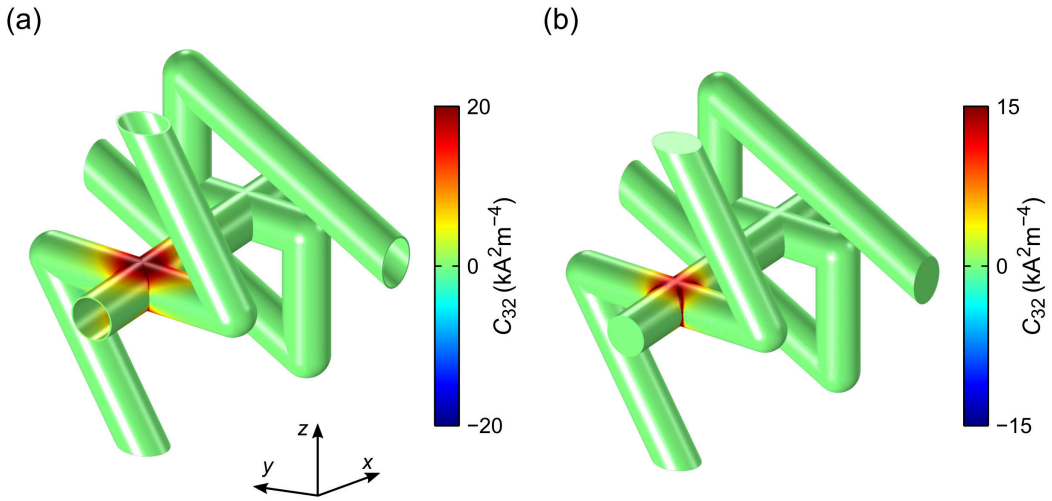

Figure 3.14: Numerical calculation of the cofactor C_{32} for the hollow (a) and non-hollow (b) version of the metamaterial shown in Figure 3.12. The hollow version is the one that was realized experimentally, see section 5.4. The inner radius of the hollow cylinders is r and the coating thickness is t, which results in an outer radius of $r + t$. Parameters are $r = 2.5\,\mu\text{m}$, $t = 0.2\,\mu\text{m}$, $d_z = -12\,\mu\text{m}$, $d_y = -8\,\mu\text{m}$, $h = 15\,\mu\text{m}$, and lattice constant $a = 40\,\mu\text{m}$. Panel (b) adapted from [14].

A numerical calculation of the cofactor C_{32}, corresponding to the Hall tensor component A^*_{23}, for the hollow and non-hollow version of the structure is shown in Figure 3.14(a) and (b), respectively. For the given directions of macroscopic current flow ($\hat{x}$) and magnetic field ($\hat{z}$), this component corresponds to a Hall electric field in the z-direction. For both structures, in agreement with the intuitive interpretation, the cofactor is significantly larger than zero only in a small region close to the corresponding pick-up structure.

The components of the effective Hall tensor can be derived from a volume average, i.e., by evaluating Equation 3.11. For the parameters given in Figure 3.14, the effective Hall tensor of the hollow structure is given by

$$\boldsymbol{A}_{\mathrm{H}}^{(\mathrm{hollow})*} = \begin{pmatrix} 0.01 & 0 & 0 \\ 0 & 3.31 & 76.85 \\ 0 & 7.89 & -74.45 \end{pmatrix} A_{\mathrm{H}}^{0}, \tag{3.30}$$

while the effective Hall tensor of the non-hollow structure is given by

$$\boldsymbol{A}_{\mathrm{H}}^{(\text{non-hollow})*} = \begin{pmatrix} 0 & 0 & 0 \\ 0 & 0.08 & 8.80 \\ 0 & 0.31 & -8.73 \end{pmatrix} A_{\mathrm{H}}^{0}. \tag{3.31}$$

The only relevant components are A_{23}^{*} and A_{33}^{*}. In both cases, these components have opposite sign and almost the same modulus. However, the magnitude of these components is much larger for the hollow structure. As for the chainmail-inspired structure, I am attributing this effect to the confinement of the current to a thinner layer. As the effective Hall coefficient, compare section 3.2, these components can, in principle, be made arbitrarily large by reducing the coating thickness, t.

In the saturated regime, i.e., for $|d_y/a|$ and $|d_z/a|$ large enough, compare Figure 3.13, one can find simple expressions for U_{H}^{y} and U_{H}^{z} [82]. I will only treat the hollow case. The procedure for the non-hollow case is analogous. Again, I will consider a long Hall bar made from $N_x \times N_y \times N_z$ unit cells. The straight hollow cylinders, which carry the current, can be seen as local Hall voltage sources. In [82], I have derived the Hall voltage of a hollow cylinder, which, for $t \ll r$, is given by

$$U_{\mathrm{H}}^{\text{cyl.}} = A_{\mathrm{H}}^{0} b_z \frac{1}{t\pi} I^{\text{cyl.}}. \tag{3.32}$$

Here, $I^{\text{cyl.}}$ is the current flowing through one of the hollow cylinders. In terms of the total current, I, it is given by $I^{\text{cyl.}} = I/(N_y N_z)$. Via the two pick-up structures, the voltage sources are connected in series along the y- and z-direction resulting in an orthogonal and parallel Hall voltage, respectively. These considerations yield the following expressions [82],

$$U_{\mathrm{H}}^{y} = \left(\operatorname{sgn}(d_y) \frac{1}{N_z} A_{\mathrm{H}}^{0} b_z \frac{1}{t\pi} \right) I = R_{\mathrm{H}}^{y} I \tag{3.33}$$

and

$$U_{\mathrm{H}}^{z} = \left(\operatorname{sgn}(d_z) \frac{1}{N_y} A_{\mathrm{H}}^{0} b_z \frac{1}{t\pi} \right) I = R_{\mathrm{H}}^{z} I, \tag{3.34}$$

where I have introduced the corresponding Hall resistances, R_{H}^{y} and R_{H}^{z}. Alternatively, one can give the corresponding components of the effective

Hall tensor,

$$A^*_{33} = \mathrm{sgn}\,(d_y)\,\frac{1}{\pi}\frac{a}{t}A^0_{\mathrm{H}} \tag{3.35}$$

and

$$A^*_{23} = -\mathrm{sgn}\,(d_z)\,\frac{1}{\pi}\frac{a}{t}A^0_{\mathrm{H}}. \tag{3.36}$$

The connection between Equations 3.33 and 3.35 on the one hand and Equations 3.34 and 3.36 on the other hand is made via Equation 3.28. For the parameters given in Figure 3.14, one obtains $A^*_{23} = -A^*_{33} = 63.7A^0_{\mathrm{H}}$, which is in good agreement with the full numerical calculation, compare Equation 3.30.

Potential applications

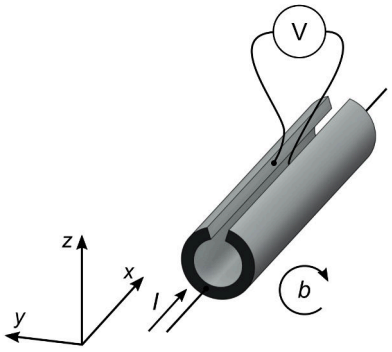

Figure 3.15: Illustration of a split-ring like metamaterial Hall element made from a metamaterial with an antisymmetric effective Hall tensor. The measured Hall voltage is proportional to the circulation of the magnetic field in the yz-plane. Adapted from [82].

A potential application of anisotropic structures is their use in sensors for the circulation of a magnetic field [82]. Consider the Hall element shown in Figure 3.15. It is made from a metamaterial with an antisymmetric effective Hall tensor. More precisely, the effective Hall tensor is chosen such that $A^*_{23} = -A^*_{32} \neq 0$ and all other components are equal to zero. The Hall element has the shape of an almost-closed split ring. Assume that the magnetic field is in the yz-plane and a current is flowing in the x-direction. A Hall voltage will be measurable between the two almost-touching ends of the split ring. This voltage is given by the line integral of the Hall electric field along the split ring. As the Hall electric field is, due to the choice of $\boldsymbol{A}^*_{\mathrm{H}}$,

proportional to the magnetic field, the measured Hall voltage is proportional to the circulation of the magnetic field. Similarly, one could think of sensors for the magnetic field integrated along an arbitrary two-dimensional path.

3.4 Bounds on the effective parameters

In the following, I will discuss bounds on the effective parameters of Hall metamaterials, i.e., on the effective Hall tensor and the effective Hall mobility.

As mentioned previously, in two dimensions, the effective Hall coefficient of a metamaterial lies in between the Hall coefficients of the constituent materials. For the three-dimensional case, a bound on the effective Hall tensor was derived by Briane and Milton [61]. Let α be a lower bound to the conductivity of the constituent materials, β_{H} be an upper bound to the conductivity of the constituent materials with nonzero Hall coefficient, and a_{H} be an upper bound to the Hall tensor of the constituent materials. Then, the bound on the effective Hall tensor is given by [61], see also [14],

$$|\boldsymbol{A}^*_{\mathrm{H}}| \leq 18 \frac{\beta_{\mathrm{H}}}{\alpha} a_{\mathrm{H}}. \tag{3.37}$$

In essence, the bound is determined by the conductivity contrast of the constituent materials. In order to obtain a large effective Hall coefficient, one has to employ constituent materials with very different conductivities. For porous structures, one of the constituent materials is insulating. Hence, α is zero and the contrast of conductivities becomes infinitely large.

An example of such a porous structure is the hollow chainmail-like metamaterial introduced in section 3.2. As discussed there, the effective Hall coefficient can be made arbitrarily large by reducing the thickness t. There is, however, a trade-off between the effective Hall coefficient and the effective conductivity [14]. While A^*_{H} scales asymptotically as t/a, the effective conductivity, σ^*_0, scales asymptotically as a/t. The product of these two quantities, i.e., the effective Hall mobility, $A^*_{\mathrm{H}}\sigma^*_0$, is asymptotically constant.

A thorough analysis shows that the effective Hall mobility of a metamaterial is fundamentally bounded. Let m_{H} be an upper bound to the Hall mobility of the constituent materials. Then, the bound on the effective Hall mobility, which I have derived based on the work of Marc Briane and Graeme Milton [61], is given by [14],

$$|A^*_{\mathrm{H}}\sigma^*_0| \leq 2m_{\mathrm{H}}. \tag{3.38}$$

Hence, using conventional Hall metamaterials, it is not possible to obtain a significantly enhanced effective Hall mobility, which would lead to an

increase in sensitivity and signal-to-noise ratios, compare section 2.1. However, in section 3.5, I will discuss how one can exceed this bound using certain structures made from a material with very high or low magnetic permeability, which offer control over the magnetic field within the unit cell.

3.5 Magnetic permeability distributions

In the following, I will study the influence of a microscopic magnetic permeability distribution on the effective Hall tensor of a metamaterial. Such permeability distributions allow to control and guide the magnetic field lines within the unit cell. Magnetic permeability distributions in the form of cylindrical laminates, which can be seen as magnetic hoses, have been used previously to transfer and route magnetic fields over long distances [83].

Following some fundamentals, I will introduce two novel metamaterials. The first metamaterial exhibits a sign-inversion of the effective Hall coefficient. The origin of the sign inversion is a specifically chosen structure with high magnetic permeability. Without this structure, the sign-inversion breaks down. The second metamaterial employs a magnetic permeability distribution to break, albeit just barely, the bound on the effective Hall mobility derived in section 3.4. As pointed out in section 2.1, high (effective) Hall mobilities are desirable as they imply high voltage-related sensitivities as well as high signal-to-noise-ratios. Furthermore, this example shows that magnetic permeability distributions allow for effective parameters that are inaccessible using conventional Hall metamaterials. For the rest of this section, I am following the corresponding chapter of my previous publication on the theory of the Hall effect in metamaterials [14]. This generalization of the theory has been suggested to me by Graeme Milton.

In order to find the effective properties of a Hall metamaterial that includes a permeability distribution, one needs to solve two problems. First, one has to determine the microscopic magnetic field for a given macroscopic average. Using this result, one can determine the effective electrical properties of the material. The equations for the microscopic magnetic field are given by,

$$\nabla \cdot \boldsymbol{b} = 0, \ \nabla \times \boldsymbol{h} = 0, \ \text{with } \boldsymbol{b} = \mu_0 \boldsymbol{\mu} \boldsymbol{h}. \tag{3.39}$$

Here, $\boldsymbol{b}$ is the microscopic magnetic induction, $\boldsymbol{h}$ is the microscopic magnetic field, $\boldsymbol{\mu}$ is the microscopic permeability tensor, and $\mu_0 = 4\pi \cdot 10^{-7}\,\mathrm{V\,s\,A^{-1}\,m^{-1}}$ is the vacuum permeability. This problem is mathematically equivalent to the problem of electric conduction, compare section 2.4.

As $\boldsymbol{h}$ is curl-free, one can express it in terms of the magnetic scalar potential, ϕ_m, as

$$\boldsymbol{h} = -\nabla\phi_{\mathrm{m}}. \tag{3.40}$$

In analogy to the vector-valued electric potential, $\boldsymbol{\Phi}$, see section 3.1, the vector-valued magnetic "scalar" potential, $\boldsymbol{\Phi}_{\mathrm{m}}$, not to be confused with the magnetic vector potential, which is often denoted as $\boldsymbol{A}$, connects the microscopic magnetic field, $\boldsymbol{h}$, with the corresponding macroscopic magnetic field, $\langle \boldsymbol{h} \rangle$,

$$-\left(\nabla\boldsymbol{\Phi}_{\mathrm{m}}\right)\langle \boldsymbol{h} \rangle = \boldsymbol{h}. \tag{3.41}$$

The vector-valued magnetic potential solves

$$\nabla \cdot \left(\boldsymbol{\mu}\nabla\boldsymbol{\Phi}_{\mathrm{m}}\right) = 0. \tag{3.42}$$

and is subject to the same periodicity conditions as $\boldsymbol{\Phi}$. One can now define the matrix-valued magnetic field as

$$\boldsymbol{H} = -\left(\nabla\boldsymbol{\Phi}_{\mathrm{m}}\right) \text{ and } \boldsymbol{B} = -\mu_0\boldsymbol{\mu}\left(\nabla\boldsymbol{\Phi}_{\mathrm{m}}\right). \tag{3.43}$$

The effective permeability of the metamaterial is given by

$$\boldsymbol{\mu}^* = \boldsymbol{\mu}^* \langle \boldsymbol{H} \rangle = \frac{1}{\mu_0} \langle \boldsymbol{B} \rangle. \tag{3.44}$$

For the Hall effect, it is the the local magnetic field that is essential. Consequently, the effective Hall tensor results from a product of the local magnetic field and the cofactor of the matrix-valued current density. A more detailed analysis, see [14], leads to the following generalization of Equation 3.11,

$$\mathrm{Cof}\left(\sigma_0^*\right)\boldsymbol{A}_{\mathrm{H}}^*\boldsymbol{\mu}^* = \left\langle \mathrm{Cof}\left(\sigma_0\nabla\boldsymbol{\Phi}\right)^{\mathsf{T}}\boldsymbol{A}_{\mathrm{H}}\boldsymbol{\mu}\left(\nabla\boldsymbol{\Phi}_{\mathrm{m}}\right)\right\rangle, \tag{3.45}$$

which holds in the limit of weak magnetic fields.

Following these general considerations, I will come back to the two aforementioned examples of generalized Hall metamaterials. The effective magnetic permeability and the effective Hall tensor of these metamaterials follow from Equation 3.44 and Equation 3.45, respectively. I will perform the evaluation of these equations using the numerical methods described in section 3.1.

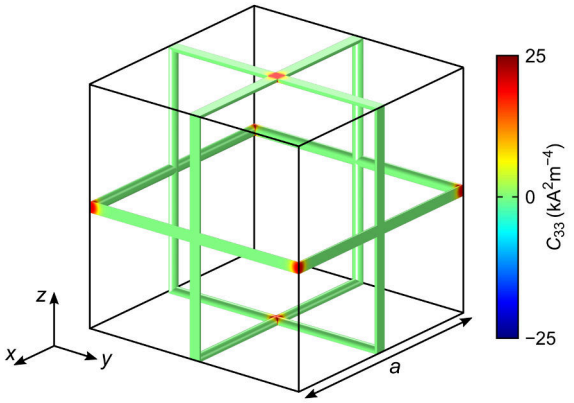

Figure 3.16: Numerical calculation of the cofactor C_{33}, corresponding to a magnetic field along $\hat{z}$, for the unit cell of a structure consisting of intersecting cylinders with radius r_1. The constituent material is isotropic with zero magnetic-field conductivity σ_0^0 and Hall coefficient A_H^0. The effective electrical properties of the structure are isotropic by symmetry. The cofactor is significantly larger than zero only in and close to the crosses that lie in planes perpendicular to the magnetic field. The effective Hall coefficient of the structure is not sign-inverted. However, it becomes sign-inverted upon the addition of a specific structure with a high magnetic permeability, compare Figure 3.17 and Figure 3.18. Parameters are $r_1 = 2\,\mu m$, $a = 86\,\mu m$, and $\sigma_0^0 = 200\,S\,m^{-1}$. Reproduced from [14].

While the equations hold for the general case, I will only discuss isotropic structures.

Both examples of generalized Hall metamaterials are based on the electrically conducting structure shown in Figure 3.16. This structure consists of crossing cylinders with radius r_1, conductivity σ_0^0, magnetic permeability $\mu^0 = 1$, and Hall coefficient A_H^0. The crosses are arranged on a body-centered cubic lattice. A numerical evaluation of Equations 3.5 and 3.11, implicitly assuming $\mu = 1$ everywhere, yields $\sigma_0^* = 3.48 \cdot 10^{-3}\sigma_0^0$ and $A_H^{*(0)} = 11.86 A_H^0$ for the effective zero magnetic-field conductivity and the effective Hall coefficient, respectively [14]. The superscript of the effective Hall coefficient indicates that any magnetic permeability is assumed to be trivial, i.e., $\mu = 1$ everywhere. The effective Hall coefficient in the presence of a non-trivial magnetic permeability distribution is denoted as $A_H^{*(\mu)}$. Clearly, the zero

magnetic-field conductivity is independent of the magnetic permeability, which is why the corresponding superscript is omitted, $\sigma_0^* = \sigma_0^{*(\mu)} = \sigma_0^{*(0)}$.

The cofactor C_{33} of the structure, shown in Figure 3.16, is, similar to the one for the structures considered previously, nonzero only in and close to the crosses. Hence, it is only the magnetic field at the crosses that is relevant. Moreover, C_{33} is nonzero only in the crosses that lie in a plane perpendicular to $\hat{z}$, i.e., perpendicular to the magnetic field. This behavior can be understood intuitively. Assume that a current is flowing axially through a cylinder perpendicular to the magnetic field. The resulting local Hall voltage can only be picked-up if the axis of the second cylinder of the cross is perpendicular to the magnetic field as well.

As pointed out above, the first metamaterial features a sign-inversion of the effective Hall coefficient. The key idea underlying the sign-inversion is to invert the corresponding component of the magnetic field for each of the crosses using a second structure made from a material with a high magnetic permeability, $\mu^1 \gg 1$.

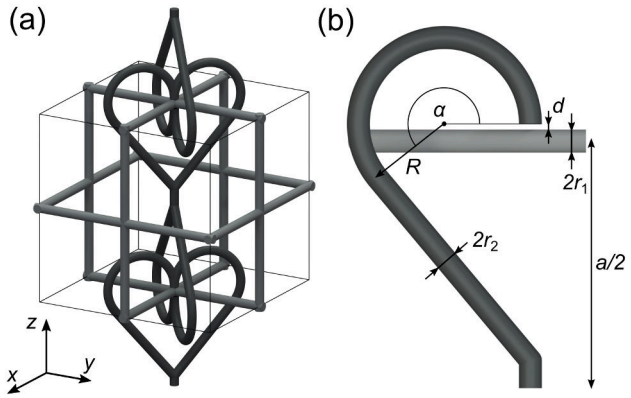

Figure 3.17: (a) Illustration of an extended unit cell of a precursor of a metamaterial with a sign-inverted effective Hall coefficient. It consists of two structures. The first structure, shown in grey, is the one introduced in Figure 3.16, which consists of electrically-conducting crossing cylinders with finite Hall coefficient. The second structure, shown in black, is made from a material with a high magnetic permeability. This second structure locally inverts the z-component of the magnetic field at the crosses perpendicular to $\hat{z}$. (b) Parameters of the structure. Reproduced from [14].

For a macroscopic magnetic field along the z-direction, such a structure is shown in Figure 3.17. It has two-fold rotational symmetry about the principal axes of the cubic unit cell. This "hose"-like structure collects the magnetic field lines and guides them such that the magnetic field is, at the crosses, locally inverted. The two structures, the electrical structure and the highly permeable structure, are not connected but separated by a small gap, compare Figure 3.17. Furthermore, the highly permeable structure is not connected over long distances. As a consequence, its electrical properties do not enter into the effective properties of the metamaterial and can be chosen arbitrarily. Due to the lack of mechanical connection of the two structures, one has to provide mechanical support, e.g., by embedding it an electrically insulating host material with $\mu = 1$.

In order to arrive at a metamaterial with an sign-inverted effective Hall coefficient, one can add such structures for each of the three axes. This procedure results in the metamaterial unit cell shown in Figure 3.18. It should be pointed out that the magnetic field is inverted only at every second cross. Naively, one might think that the two opposing contributions compensate each other and, hence, lead to a zero effective Hall coefficient. However, the hoses not only invert but also concentrate the magnetic field lines, which is why the effective Hall coefficient is sign-inverted. For the parameters given in Figure 3.18, a numerical evaluation of Equation 3.45 yields $A_{\mathrm{H}}^{*(\mu)} = -7.5 A_{\mathrm{H}}^{0}$ [14]. The effective permeability is calculated from Equation 3.44, $\mu^* = 3.14 \cdot 10^{-3} \mu^1$ [14]. Isotropic effective properties follow from the symmetry of the structure.

The second metamaterial is based on the structure shown in Figure 3.16 as well. A magnetic permeability distribution is used to concentrate the magnetic field at the crosses, which leads to an increase in the effective Hall coefficient and the effective mobility. Two cases are considered: First, a high-permeability structure, which picks-up the field lines, and, second, a zero-permeability structure, which forces the field lines into the voids. In the second case, the bound on the effective mobility, derived in section 3.4, is ultimately exceeded. Before introducing these permeability distributions, I

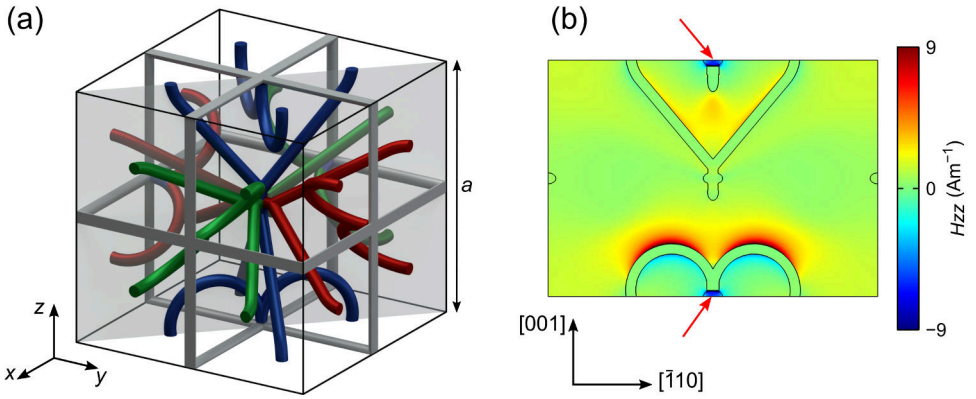

Figure 3.18: (a) Illustration of a unit cell of a metamaterial with a sign-inverted effective Hall coefficient. The sign-inversion is due to structures with a high magnetic permeability that locally invert a component of the magnetic field. Three of these structures, introduced in Figure 3.17, corresponding to the three axes, are shown. For clarity, these structures are colored in green, red, and blue corresponding to the x-, y-, and z-axis, respectively. The magneto-electric properties of the metamaterial are isotropic by symmetry. A cutplane is indicated in grey. (b) Numerical calculation of one of the components of the matrix-valued magnetic field, H_{zz}, for the cutplane shown in (a). This component relates the z-component of the microscopic magnetic field to the z-component of the macroscopic magnetic field. At the crosses, H_{zz} turns negative (indicated by the red arrows). Parameters are, compare Figure 3.17, $R = 15\,\mu\text{m}$, $r_1 = r_2 = 2\,\mu\text{m}$, $d = 0.2\,\mu\text{m}$, $\alpha = 220°$, $a = 86\,\mu\text{m}$, $\sigma_0^0 = 200\,\text{Sm}^{-1}$, $\mu^1 = 1000$. Adapted from [14].

will revisit the effective properties of the purely electrical structure.

The effective zero magnetic field conductivity of this structure is determined by the relative area of one cylinder, $\sigma_0^* = 2\pi\,(r_1/a)^2\,\sigma_0^0$, as long as r_1/a is small. This result is in excellent agreement with corresponding numerical calculations (not depicted). The confinement of the current flow to the cylinders leads to an enhancement of the effective Hall coefficient of the structure as compared to A_H^0, which is proportional to a/r_1. The proportionality constant is inferred from numerical calculations (not depicted), which yield $A_\text{H}^{*(0)} \approx 0.275\,(a/r_1)\,A_\text{H}^0$. Hence, the effective mobility, $A_\text{H}^{*(0)}\sigma_0^*$, scales as r_1/a. Upon reducing r_1, it becomes smaller as the reduction in conductivity overcompensates the increase in the effective Hall coefficient.

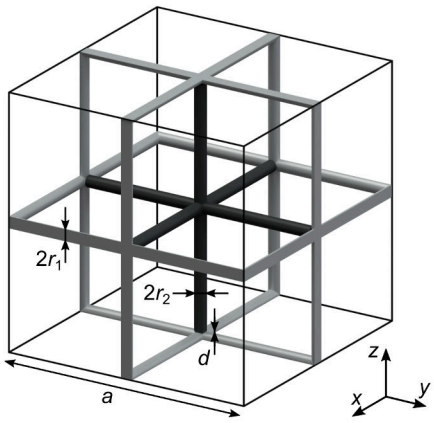

Figure 3.19: Illustration of a unit cell of a metamaterial based on the structure introduced in Figure 3.16, which is shown in grey. It employs a second structure, shown in black, made from cylindrical rods with radius r_2 and high permeability, $\mu^1 \gg 1$, to concentrate the magnetic field at the crosses. This concentration leads to an increase in the effective Hall coefficient and the effective mobility. However, it does not break the bound on the effective mobility derived in section 3.4. Reproduced from [14].

A strategy of enhancing the effective mobility starts from the observation that most of the magnetic field lines pass through the unit cell without actually contributing to the effect. Ideally, one would like to confine the magnetic field to the crosses. A straightforward way of doing so is to use cylindrical rods made from a material with a high permeability as a magnetic field concentrator. This structure enhances the corresponding component of the magnetic field at each of the crosses. As a result, the local Hall voltage, and therefore, the effective Hall coefficient increases. Similar strategies are used to enhance the sensitivity of Hall effect based magnetic field sensors [4, 9]. The corresponding metamaterial unit cell is shown in Figure 3.19. Note that there are small gaps between the two structures, which provide electrical insulation. This insulation is necessary as high-permeability materials are typically electric conductors.

While this strategy further enhances the effective Hall coefficient, a thorough analysis shows that no combination of parameters yields an effective mobility larger than the mobility of the constituent material of the electrical structure, see [14], i.e., this structure does not yet break the bound on the

effective Hall mobility, see [14]. However, for a specific choice of parameters and by reducing r_1, one can approach this value, i.e., $A_{\mathrm{H}}^{*(\mu)}\sigma_0^* \to A_{\mathrm{H}}^0\sigma_0^0$. At the same time, the effective Hall coefficient, $A_{\mathrm{H}}^{*(\mu)}$, can be made arbitrarily large. The key problem of this structure is that the high-permeability rods leave gaps with a width of $2(r_1 + d)$ for the electrical structure and the corresponding insulation. The electrical structure has the same permeability as the surrounding vacuum/air, which leads to a weaker confinement of the field lines as one may expect.

One possibility to circumvent this problem, and eventually to break the bound, is to use a material with zero magnetic permeability, $\mu^1 = 0$, i.e., a superconductor. A corresponding metamaterial unit cell is shown in Figure 3.20. The electrical structure is shown in grey. The superconductor is shown in blue. The voids have the same shape as the high permeability material in Figure 3.19. Additionally, thin vacuum/air gaps are introduced to insulate the superconductor from the rest of the structure.

As the magnetic field lines cannot penetrate into the superconductor, they are forced into the voids. Hence, the corresponding enhancement in local magnetic field can be estimated by considering the relative cross-sectional area of the voids, $(6\pi(r_1/a)^2 + 2(d/a))^{-1}$, for $r_2 = 2r_1$, $r_1/a \ll 1$, and $d/r_1 \ll 1$, giving $A_{\mathrm{H}}^{*(\mu)} \approx 0.069(3\pi(r/a)^3 + 2dr_1/a^2)^{-1}$. The enhancement can become large enough to break the bound on the effective mobility. However, breaking the bound requires quite extreme parameters. An effective Hall mobility of $A_{\mathrm{H}}^{*(\mu)}\sigma_0^* = 3.85A_{\mathrm{H}}^0\sigma_0^0$, as calculated by a numerical evaluation of Equation 3.45, which is in very good agreement with the simple estimate given above, is obtained for $r_1 = 0.5\,\mu\mathrm{m}$, $r_2 = 2r_1$, $d = 0.01\,\mu\mathrm{m}$, and $a = 86\,\mu\mathrm{m}$ [14]. It should be pointed out that I am still making the assumption of weak magnetic fields. As this assumption has to hold at the crosses, the corresponding macroscopic magnetic field has to be even weaker.

While a realization of such a metamaterial does not seem to be in reach, at least on the microscale, it shows that, conceptually, magnetic permeability distributions can lead to previously inaccessible effective parameters. In contrast to conventional Hall metamaterials, which are the main subject of this thesis, they not only allow for arbitrarily high effective Hall coefficients but also for an enhancement of the effective Hall mobility.

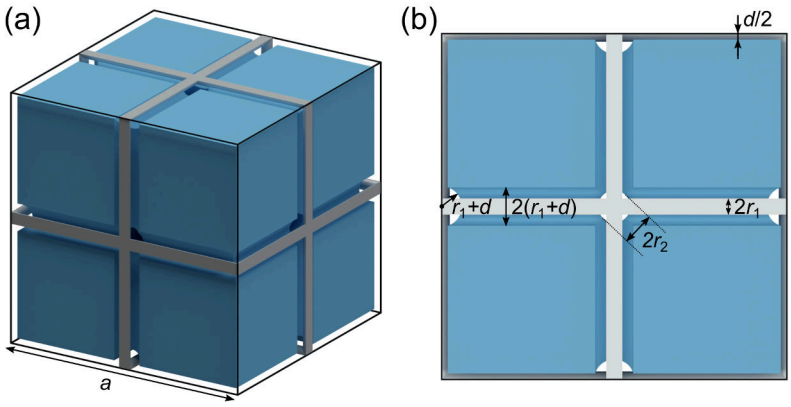

Figure 3.20: (a) Illustration of a unit cell of a metamaterial similar to the one shown in Figure 3.19. Instead of a high permeability material, it employs a superconducting structure, i.e., $\mu^1 = 0$, shown in blue, to concentrate the magnetic field at the crosses, which are the regions of larger cofactor, compare Figure 3.19, by forcing the magnetic field lines into the voids. For a specific choice of parameters, the effective mobility of this metamaterial can be larger than twice the largest value among the constituent materials, breaking the bounds derived in section 3.4. The two structures are separated by a thin gap, which is crucial to avoid short-circuits. (b) Top view of the unit cell with a definition of the geometry parameters. Reproduced from [14].

Chapter 4

4 Methods

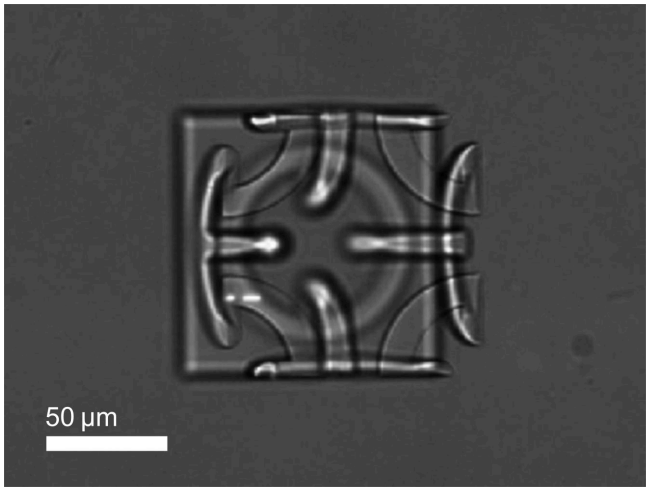

Light micrograph of a chainmail-inspired polymer unit-cell template during the 3D DLW process.

In this chapter, I will present the methods used in the fabrication of microscale Hall metamaterials. I will start with a discussion of three-dimensional laser lithography, which has been used to create electrically insulating three-dimensional polymer templates. Thereafter, I will outline the fundamentals of atomic layer deposition. Using this highly conformal deposition technique, the polymer templates were coated with a thin semiconducting film. Together, these two techniques enable the fabrication of highly complex three-dimensional Hall metamaterials. Furthermore, I will briefly summarize the principles of electron-beam evaporation, which has been used for the deposition of thin metal films forming Ohmic electrical contacts to the semiconducting metamaterial.

4.1 Three-dimensional laser lithography

Three-dimensional laser lithography, also called three-dimensional direct laser writing (3D DLW), is a technique for the fabrication of almost arbitrarily complex three-dimensional structures on the nano-, micro-, and mesoscale [84, 85]. It is based on tightly focusing a pulsed laser beam via an objective lens into a photoresist. Via multi-photon (typically two-photon) absorption, the photoresist undergoes a chemical reaction in the focal volume (the voxel). By moving the focus relatively to the sample, complex three-dimensional structures can be created. In the case of a negative photoresist, the exposed regions are, due to the chemical modification, rendered insoluble while the rest of the resist dissolves in the developer. In the less common case of a positive photoresist, the exposed volume is rendered soluble, while the unexposed regions are not.

The method, which belongs to the class of 3D printing techniques, was originally introduced in 1997 [86], seven years after two-photon absorption had first been employed in laser fluorescence scanning microscopy [87]. In the meantime, it has found a wide range of applications. Prominent examples include the fabrication of photonic crystals [88], micro-optics [89], cell scaffolds [90, 91], and mechanical metamaterials [92].

In the scope of my thesis, I have used 3D DLW in the so-called dip-in configuration for the fabrication of templates for metamaterial Hall-bar structures on the microscale. Using a galvanometer mirror system, structures were fabricated from a commercial photoresist in a layer-by-layer fashion. Detailed fabrication parameters are given in chapter 5 and chapter 6.

In the following, I will introduce the fundamentals of 3D DLW followed by a description of the setup used. Thereafter, I will discuss specific issues that arise during layer-by-layer fabrication, which is typically used for structures with medium and large feature sizes as compared to the size of a voxel.

Fundamentals

In the most common version of 3D DLW, one uses a negative photoresist that is a liquid mixture of at least two components, a monomer (typically an acrylate) and a photoinitiator. An example of a typical monomer is pen-

taerythritol triacrylate (CAS 3524-68-3, commonly abbreviated as PETA). A typical photoinitiator is Irgacure 369 (CAS 119313-12-1). In the simplest case, the photoinitiator molecule is excited by the simultaneous absorption of two photons. Following excitation, the molecules cleave and form radicals, which subsequently trigger a radical polymerization reaction. The crosslinked polymer withstands the developer, typically an organic solvent, while the liquid monomer is washed away. Other systems, such as chemically amplified resists [93], based on molecules generating acids upon illumination, can be used as well. An example of such a resist used in 3D DLW is SU-8 [94].

As stated above, the photoinitiator is typically excited by the simultaneous absorption of two photons. In two-photon absorption [95], the rate of photons absorbed per molecule is proportional to the intensity squared. Hence, pulsed lasers, which achieve high intensities by concentrating the energy in the temporal domain are commonly employed for 3D DLW. Examples include Ti:sapphire lasers with typical specifications of a pulse width of less than 100 fs and a repetition rate of 80 MHz. Nevertheless, 3D DLW using continuous wave (CW) lasers has been demonstrated as well [96].

The nonlinearity of the process is crucial for the fabrication of extended three-dimensional structures. A simple example of such a structure is a laterally extended thin sheet [96]. In order to create such a sheet, one would move the focus through the photoresist in a corresponding way, which results in a series of sequential exposures. In most cases, it can be assumed that these sequential exposures add up linearly [97]. Furthermore, the laterally integrated intensity of the laser beam is constant along the optical axis. Hence, if the process is linear, all volume elements of the photoresist would see the same exposure dose and a massive block of material rather than a thin sheet would result [96].

The resolution of 3D DLW is, due to the wave-nature of light, limited by diffraction. However, the term *resolution* requires some specification. One needs to differentiate between the minimum width of a line and the minimum distance between neighboring lines.

The complicated behavior of a photoresist can often be described by a simple threshold model [97]. In this model, a region is polymerized and withstands development if the exposure dose is higher than a certain threshold value. By approaching this threshold, the linewidth can, in principle,

become arbitrarily small [97]. In reality, where this threshold model falls short, linewidths of about 100 nm can be achieved. On the contrary, the minimum distance between neighboring lines is fundamentally limited as long as doses of sequential exposures accumulate [97]. This problem is especially pronounced in the axial direction, in which the confinement of the intensity is weaker.

High resolution requires objectives with high numerical apertures (NA) and favors the use of short wavelengths. For example, in [98], a wavelength of 400 nm rather than the typical near-IR wavelengths around 800 nm was used for the fabrication of nonlinear three-dimensional photonic crystals. Using techniques inspired by stimulation emission depletion (STED) microscopy [99], it is possible to overcome the diffraction limit [97].

As mentioned above, three-dimensional structures are created by moving the focus along a corresponding trajectory through the photoresist. Different methods may be used to achieve this movement. Many systems feature conventional three-axis piezo stages, which offer ultra-high precision and repeatability but suffer from low writing speeds and small movement ranges. The use of galvanometer mirror scanning systems, which are based on a deflection of the beam and have been wide-spread in imaging applications for decades, allows for much higher lateral writing speeds. Motorized stages are often employed in combination with the aforementioned systems, typically in order to increase the maximum lateral dimensions of the structures.

The strategy used for the discretization of an object into a corresponding trajectory depends on its feature size. For structures with a feature size in the order of the size of a voxel, the density of trajectory lines, which are often complex and three-dimensional, is typically low. The shape of the voxel is clearly visible in the final structure. Often, the total path length of the trajectory is short and piezo stages are used. Examples include three-dimensional chiral photonic crystals [100]. For objects that are large as compared to the size of a voxel, usually a different approach, known from conventional macroscopic 3D printing, is used. First, the object is decomposed into a set of lateral layers or slices. Thereafter, each layer is filled with a dense set of lines. Different methods of filling the layer may be used. Typically, it is rastered, i.e., filled with parallel straight lines. Alternatively, it can be filled with lines contouring to the shape of its outer boundary. Sometimes, a combination of

these approaches is used. In specifying fabrication parameters, I will refer to the distance between neighboring slices as the slicing distance, while the distance between neighboring lines is referred to as the hatching distance. Fabrication is performed line-by-line and layer-by-layer. In this layer-by-layer approach, the high lateral writing speeds of galvanometer mirror scanners can be fully exploited, while the axial movement can be comparably slow.

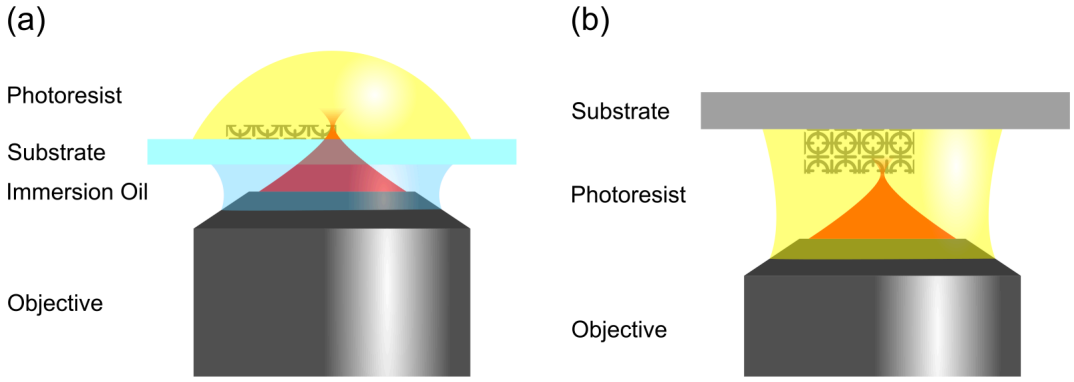

Figure 4.1: Schematic illustration of the two most common writing configurations of 3D DLW. (a) Conventional configuration: The objective is immersed in an index-matched transparent oil. The laser is focused through a thin, transparent substrate into the photoresist. (b) Dip-in configuration: The objective is directly immersed in a liquid photoresist. In order to obtain high resolution, the resist has to be index-matched. The dip-in configuration allows for structures taller than the working distance of the objective and, furthermore, for opaque substrates. Adapted from [101].

Depending on the photoresist and the desired height of the structures, different writing configurations are used. The two most often used configurations are shown in Figure 4.1. In the conventional configuration, the objective is immersed in an index-matched oil and the laser is focused through a transparent thin substrate, usually a coverslip, into the photoresist. Hence, the height of the structures is limited by the working distance of the objective and the thickness of the substrate. Further limitations on the height of the structures are imposed by abberations caused by the substrate, the polymerized material, and, if the photoresist is not index-matched, the photoresist itself. In the more recently introduced dip-in configuration [92], the objective

is immersed in the photoresist itself. In this configuration, the height of the structures is, in principle, unlimited. The sequential fabrication of two closely spaced structures taller than the working distance, however, is still impossible. A further advantage is that the substrate may be opaque. The dip-in configuration requires the photoresist to be liquid and index-matched. Furthermore, cleaning of the objective from the resist has to be possible.

Solid photoresists, which include all positive photoresists, are not compatible with the dip-in configuration and, therefore, not suitable for the fabrication of tall structures. Solid resists are sometimes desired as they facilitate the fabrication of structures that are not attached to the substrate or other parts of the structure.

Nanoscribe setup

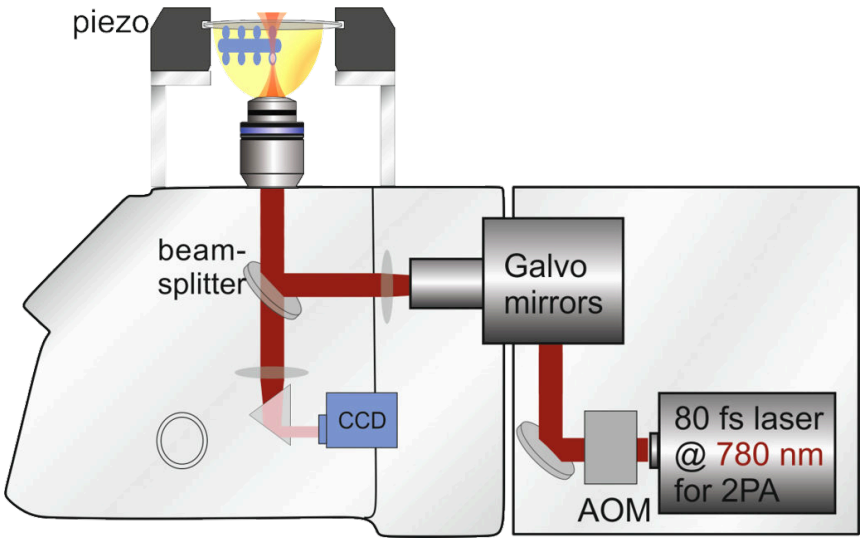

Figure 4.2: Schematic illustration of the Photonic Professional GT (Nanoscribe GmbH) 3D DLW sytem. Image courtesy of Nanoscribe GmbH.

For the fabrication of the structures presented in this thesis, a commercial setup was used (Photonic Professional GT, Nanoscribe GmbH). The system is schematically shown in Figure 4.2. It is based on an inverted microscope and employs a femtosecond pulsed frequency-doubled erbium-doped fiber

laser with a wavelength of 780 nm. The laser power can be controlled via an acousto-optic modulator (AOM) and is typically in the order of 10-40 mW. The system features a three-axis piezo stage with a writing range of 300 µm along all three axes that allows for writing speeds in the order of 100 µm s^{-1}. Lateral writing speeds as high as 15 cm s^{-1} can be achieved by deflecting the beam using a galvanometer mirror scanning system. Its scanning field depends on the objective used. For the 25× NA 0.8 objective that I have used, it has a diameter of up to 600 µm. Larger structures can be decomposed into smaller parts and fabricated stepwise. In this case, several writing fields are stitched together using a motorized stage. A so-called interface finder facilitates the determination of the position of the interface between the substrate and the photoresist. Furthermore, the writing process can be monitored via a camera.

Fabrication challenges

In 3D DLW, deviations from the intended design can have numerous causes including poor discretization, finite voxel size [102], and proximity effects [103]. In the following, I will focus on specific problems that arise during layer-by-layer fabrication of structures that protrude downwards or horizontally. As described above, this method is typically chosen for the fabrication of structures with feature sizes that are large as compared to the size of a voxel.

Many of such structures have features protruding downwards, i.e., towards the substrate. If the fabrication is performed in a layer-by-layer fashion, these features will, at certain times during the writing process, not have a mechanical connection to the rest of the structure, which is typically anchored to the substrate, which means that they are free to move in the usually liquid photoresist. Such movement can cause significant deviations from the intended design.

In some cases, but not in general, it is possible to alleviate this problem by adopting a certain writing strategy or by choosing a specific orientation of the structure. In conventional 3D printing, one uses sacrificial materials, which provide mechanical support during fabrication and can be readily removed afterwards. This removal is either performed mechanically or with the aid

of chemicals. For 3D DLW, such sacrificial materials have been developed recently [104]. Due to the typical length scales involved, mechanical removal of the sacrificial structures is not feasible. Rather, chemical bond cleavage was employed [104].

For negative values of the distance parameter, d, this problem occurs, in principle, during fabrication of the chainmail-like metamaterial structures, see section 5.3. It is, however, not pronounced as the mechanical connection to the rest of the structure is made within seconds and can, therefore, be neglected.

Another issue is encountered for cantilever-like, i.e., horizontally protruding, structures. Such structures tend to warp, i.e., they are often distorted and bent upwards. The effect, which at least partially occurs during the writing process already, is assumed to be related to stresses within the structure. As a rule of thumb, structures protruding by more than 50 µm will show pronounced signs of warping.

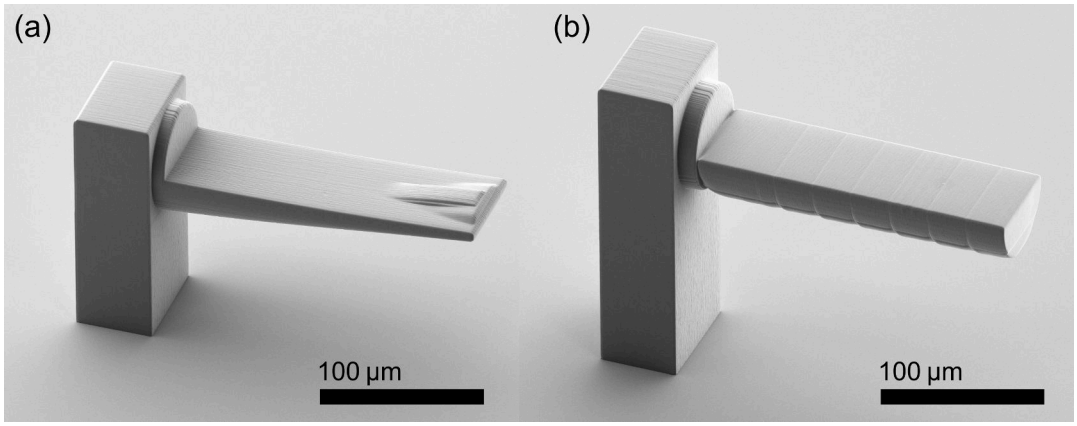

Figure 4.3: Scanning electron micrographs of cantilever-like polymer microstructures with a nominally semi-circular cross section fabricated via 3D DLW. Fabrication was performed in a layer-by-layer fashion from a commercial photoresist (IP-S, Nanoscribe GmbH) using a 25× NA 0.8 objective. The structures resemble the side-contacts of metamaterial Hall bars, see section 5.1. (a) Cantilever fabricated in a single step. The structure is heavily deformed. (b) Cantilever fabricated in a sequential fashion from shorter overlapping segments. The realized structure shows the intended semi-circular profile.

The problem of warping is known from conventional 3D printing techniques, such as stereolithography (SLA) [105] and fused deposition modeling (FDM) [106]. In FDM, warping occurs due to thermal shrinkage during cooling of the liquefied filament [106].

Warping affects the fabrication of the side-contacts of the polymer metamaterial Hall bar templates that is described in section 5.1. Scanning electron micrographs of cantilevers resembling these side-contacts are shown in Fig 4.3. The cantilevers are nominally identical and protrude by 200 µm. In the design, they have a semi-circular cross section. The cantilever shown in Fig 4.3(a) was fabricated in a single step. It is heavily distorted and bent upwards. Its profile strongly deviates from the intended semi-circular shape. A simple yet effective remedy is a step-wise fabrication strategy. A scanning electron micrograph of a corresponding structure is shown in Figure 4.3(b). In each step, only a short segment, protruding by a few ten microns, is written. The final structure, which closely resembles the intended shape, is composed of several such sequentially-written overlapping segments. Sacrificial support structures, as discussed above, offer an alternative approach of tackling the problem, compare [104].

4.2 Atomic layer deposition

Atomic layer deposition (ALD) is a method for the conformal deposition of thin films with excellent homogeneity and thickness control at the atomic level. The films are deposited from gas phase, typically in vacuum. Two chemicals, so-called precursors, react sequentially with the surface of a sample in a self-terminating manner, which leads to an almost perfectly conformal coating, even in the case of very high aspect-ratio structures such as deep holes or trenches. This conformal nature of the deposition process is schematically illustrated in Figure 4.4.

The technology was invented independently in the Soviet Union and Finland in the 1960s and 1970s, respectively [107]. While it was a niche technology in the years following its invention, ALD related research has seen a tremendous growth over the past three decades [107, 108] and it has found use in the industrial fabrication of semiconductor devices [109]. For example, it can be used in the fabrication of trench capacitors for dynamic random access memory (DRAM) [110, 111], which feature very large depth-to-width ratios. The ongoing miniaturization almost inevitably leads to such high-aspect ratio structures as well as to the need for excellent control over the deposition of very thin high-quality films [111–113]. Aside from the use of ALD in the semiconductor industry, other applications, such as the fabrication of solid oxide fuel cells [114, 115] or the fabrication of gas diffusion barriers [116, 117] exist as well.

For my purposes, two aspects were decisive. First, complex three-dimensional polymer templates fabricated by 3D DLW can be coated with a conformal, homogeneous thin film with a well-defined thickness. ALD has been previously used for this purpose. Examples include the fabrication of lightweight hollow ceramic nanostructures [118] and the fabrication of woodpiles with complete photonic bandgaps in the visible based on a sophisticated double inversion process [119]. Second, a suitable electrically conducting material, namely zinc oxide (ZnO), is available. The combination of these two technologies, 3D DLW and ALD, allows for the fabrication of of Hall metamaterials on the microscale.

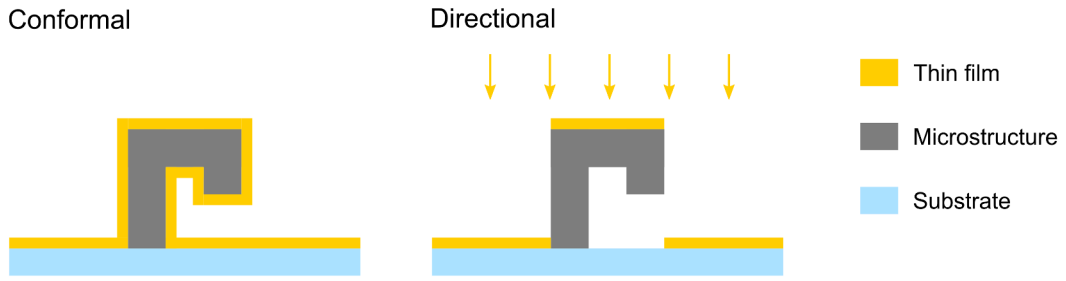

Figure 4.4: Schematic illustration of conformal (left) versus directional (right) deposition. An ideally conformal process coats all surfaces of a structure independently of their orientation with a layer of constant thickness. An example of an almost ideally conformal process is ALD. On the contrary, physical vapor deposition techniques, such as electron-beam physical vapor deposition, are typically directional, coating only the parts within line-of-sight.

In the following, I will briefly describe the deposition of ZnO by ALD as well as the ALD reactor used in this thesis. Detailed discussions of ALD in general [108, 113] and ALD of ZnO in particular [122] can be found elsewhere. The deposition of ZnO from diethylzinc (DEZn) and water is based on the following exothermic reaction [113]:

$$\mathrm{Zn(CH_2CH_3)_2 + H_2O \longrightarrow ZnO + 2\,C_2H_6}, \quad \Delta H = -293\,\mathrm{kJ}. \tag{4.1}$$

The key idea of ALD is that the two precursors are not present simultaneously in the reactor chamber but only one at a time. As stated above, this results in sequential gas-surface reactions (described in detail below). Due to the pronounced exothermic nature of these reactions, they can be performed without employing additional means such as plasma- or radical-assistance [113]. The remaining aid is the temperature of the sample and reactor chamber, which is usually chosen within a specific temperature range. Consequently, the process is referred to as a thermal ALD process.

This deposition of ZnO from DEZn and water is an important example of thermal ALD using metal organic chemistry. Another example is the deposition of Al_2O_3 from trimethylaluminum (TMAl) and water, see, e.g., [123], which can be considered to be the prime example of ALD in general. Other types of reactions, e.g., fluorosilane elimination chemistry for the deposition of metals, have been employed as well, see, e.g., [113].

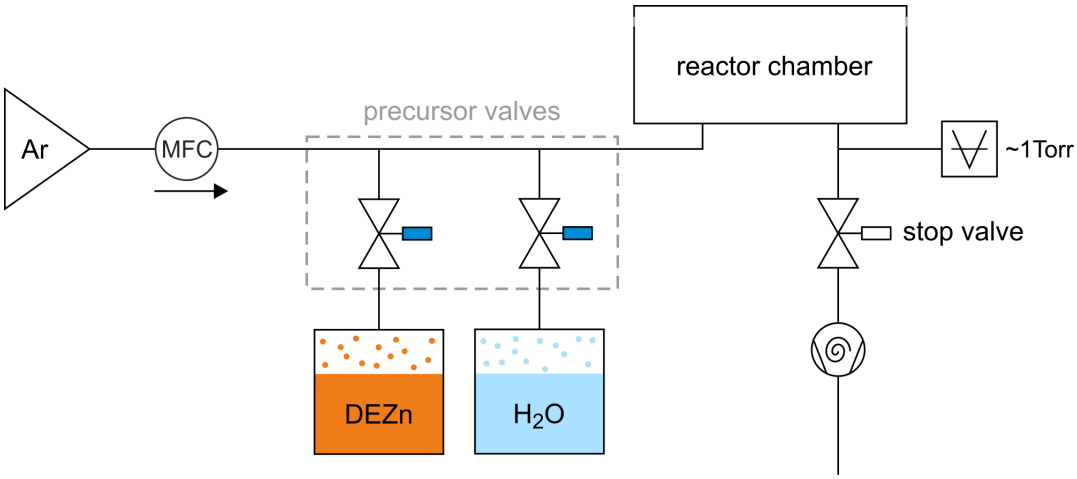

Figure 4.5: Simplified schematic of the ALD system used in this thesis. The samples are placed in a heated reactor chamber which has a carrier gas inlet and an oulet which is connected to a vacuum scroll pump. A constant viscous Ar gas flow through the chamber is maintained and controlled using a mass flow controller (MFC). Precursor cylinders are connected to the carrier gas line via dedicated electrically controlled valves. An additional valve, the stop valve, is used for venting the chamber and for alternative growth schemes, see [120]. The pressure is monitored using a Pirani gauge. Adapted from [121].

The commercial ALD reactor used in this thesis (Savannah 100, Cambridge Nanotech Inc., now Ultratech Inc.) is schematically shown in Figure 4.5. The reactor features a heated reactor chamber which is connected to a vacuum pump. It is a so-called viscous-flow reactor, i.e., a constant viscous carrier gas flow through the chamber to the pump is maintained throughout the deposition process. The cylinders containing the precursors are connected to a carrier gas line upstream of the reactor chamber and the precursors can be pulsed into the carrier gas stream using dedicated valves. The carrier gas entrains the precursor molecules and carries them to and through the reactor chamber acting simultaneously as a purge gas for removing excess precursor molecules. The pressure in the reactor chamber is around 1 Torr $\approx$ 1.3 mbar. Depending on the process, the temperature of the reactor chamber is typically between 80 °C and 250 °C. In order to avoid condensation of the precursors, certain other parts of the reactor are heated as well. It should be noted that

many other reactor designs have been developed and are currently used, see, e.g., [113]. Some of these often industry-driven designs enable much shorter deposition times and lead to better cost-efficiency.

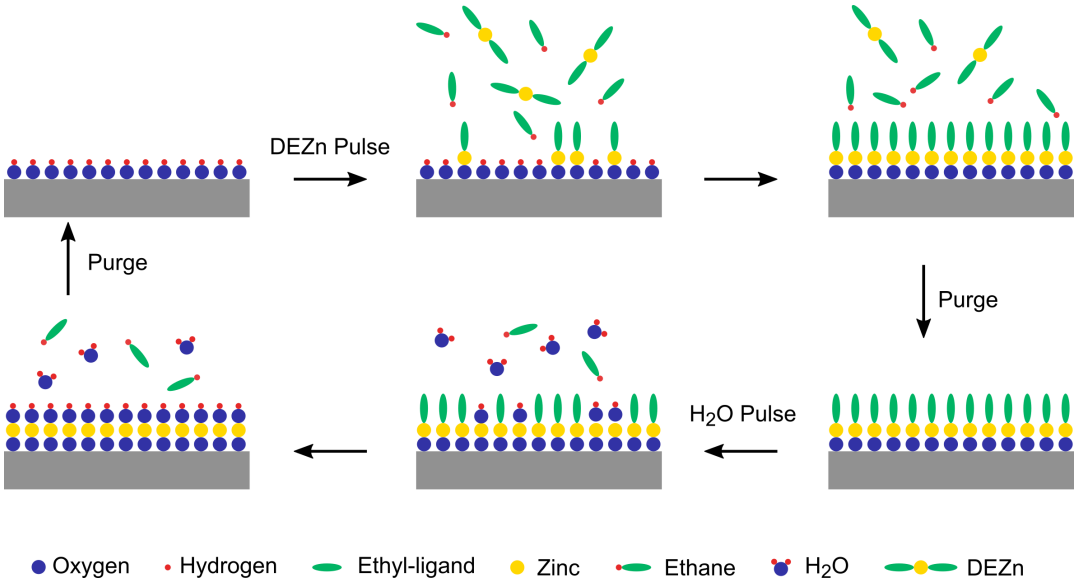

Figure 4.6: Simplified and idealized schematical illustration of a single ALD cycle for the growth of ZnO from DEZn and water. A cycle consists of two half-cycles. In the first half-cycle, DEZn is introduced into the chamber and reacts with the hydroxyl-terminated surface. In the second half-cycle, H_2O reacts with the surface. In both half-cycles, excess precursor molecules are removed from the chamber in the purge step due to the carrier gas flow. Adapted from [120, 124].

The deposition of films via ALD is based on a typically large number of repetitions of a single ALD cycle. Such an ALD cycle consists of two half-cycles, each corresponding to the reaction of one of the precursors with the sample surface. The layer deposited in a single ALD cycle is usually less than a monolayer [113]. In the case of ZnO from DEZn and water, the growth per cycle (GPC), which depends on a number of factors including the reactor design, is typically between 1.8 Å and 2.0 Å, and close to the ideal interplanar distance, which lies, depending on the orientation, between 2.48 Å and 2.82 Å [122, 125]. The GPC is often almost constant over a wide temperature range,

which is referred to as the ALD window[1]. Nevertheless, even in the ALD window, other properties depend heavily on temperature (see below). The ALD window for ZnO from DEZn and water is $\sim$ 100-170 °C [126]. However, successful deposition at temperatures as low as room temperature [127] and above 300 °C [122] has been reported. In the following, I will give a detailed step-by-step description of the ALD process for the deposition of ZnO as described in [126]. A corresponding illustration of a single ALD cycle is shown in Figure 4.6.

1. The samples are placed in the heated reactor chamber. A constant Ar gas flow of 20 sccm is set and controlled. The surface is assumed to be terminated by hydroxyl groups. This is not always the case. For example, the growth initiation on polymeric substrates can be very complex (see below).

2. DEZn is introduced into the reactor chamber by opening the corresponding valve for a short time (15 ms). The DEZn molecules react with the hydroxyl groups mainly via ligand exchange, i.e., they are chemisorbed, forming surface$-O-Zn-C_2H_5$ groups. The reaction terminates as soon as there are no hydroxyl groups left on the surface, i.e., the reaction is self-terminating.

3. Due to the Ar gas flow, excess DEZn molecules are removed from the reactor chamber. At 150 °C and 200 °C the purge time is 20 s and 10 s, respectively.

4. H_2O is introduced into the reactor chamber by opening the corresponding valve for 15 ms and reacts with the surface in a self-terminating way forming surface$-O-Zn-OH$ groups. Following the reaction, the film is again terminated by hydroxyl groups.

5. Due to the Ar gas flow, excess H_2O molecules are removed from the reactor chamber. The purge time is the same as in step 3.

6. The ALD cycle, i.e., steps 2 to 5, is repeated for a specified number of times.

[1] Alternatively and in a more general sense, the ALD window is often defined as the range over which the reactions are self-terminating [123].

The process as described above is idealized. Saturation of the half-reactions is not only due to the limited number of reactive sites but steric hindrance can play a role as well [123]. Besides ligand exchange, chemisorption can take place via dissociation and association [123]. Furthermore, purge times are determined by the desorption of the precursors from the reactor surfaces, which leads to their aforementioned temperature dependence [113].

Properties of ALD deposited ZnO

In the following, I will briefly review the properties of ZnO with an emphasis on the properties of films deposited via ALD. Exhaustive discussions of the properties of ZnO can be found in the literature [128, 129].

ZnO is a II-VI semiconductor with a direct wide bandgap of 3.4 eV [130] that is transparent throughout the visible regime of electromagnetic radiation [131]. It crystallizes in the wurtzite, zincblende, and rocksalt structure, with the wurtzite structure being stable at ambient conditions [128]. Films deposited via ALD are usually polycrystalline and have wurtzite structure. The preferential orientation of the grains depends on the process parameters, especially temperature, and the substrate [122, 132]. Additional control over the orientation was obtained by using intermediate Al_2O_3 layers [133, 134]. Epitaxial growth via ALD, though less common, is possible as well and has usually been performed using Sapphire substrates [122]. Notably, the crystal structure lacks a center of inversion, which is a prerequisite for the piezoelectricity of ZnO as well as for second harmonic generation (SHG), compare section 2.2.

ZnO usually shows a strong intrinsic n-type conductivity, the origin of which is being controversial. In the past, it has been attributed to oxygen-vacancies and zinc-interstitials. More recent computational work has shown that this explanation is unlikely and that the intrinsic conductivity is rather due to unintentional doping, with hydrogen being a prime candidate [135, 136].

Additional n-type doping can be achieved using, e.g., group III elements [128]. An important example is aluminum doped zinc oxide (Al:ZnO or AZO), which is an alternative to other transparent conducting oxides (TCOs) such as the widely-used indium tin oxide (ITO). ALD of Al:ZnO is well

established [122, 137]. An important application of Al:ZnO is its use in copper indium gallium selenide (CIGS) thin-film solar cells [138]. There, bilayers of Al:ZnO and ZnO are used as transparent front contacts, with the ZnO layer preventing diffusion of Al into the absorber. These layers are, however, usually not deposited via ALD [139]. Al:ZnO has been considered as an alternative to ZnO for the realization of Hall metamaterials. However, it was not used as its electrical properties are not more suitable than those of ZnO.

In contrast to n-type doping, p-type doping, especially reliable and high p-type doping, is hard to achieve, both for ALD deposited ZnO as well as for ZnO in general [128, 131, 140]. However, p-type conductivity has been reported [122], e.g., for ALD films deposited from DEZn and ammonia water [126].

For ZnO, one can assume that the Hall scattering factor is unity [128]. Consequently, Hall mobility and drift mobility are identical. In experiments, usually the Hall mobility is measured. For bulk crystalline ZnO, experimental values as high as $\sim 200\,\mathrm{cm^2\,V^{-1}\,s^{-1}}$ at room temperature have been reported [128, 141, 142]. At lower temperatures, the mobility reaches $2000\,\mathrm{cm^2\,V^{-1}\,s^{-1}}$ at 50 K [141].

The electrical properties of ALD deposited ZnO films can be tuned by varying the deposition parameters, especially temperature. Figure 4.7 shows the charge-carrier concentration and Hall mobility for such films versus temperature as reported in the literature and determined in my experiments. All of the measurements correspond to films deposited from DEZn and water using a Savannah 100 ALD reactor (Cambridge Nanotech Inc., now Ultratech Inc.). Results for two own types of samples, corresponding to reference samples for the probe station based experiments, see chapter 5, and the integrated Hall-bar devices, see chapter 6, are shown. In both cases, the film was grown on a glass substrate. Measurements were carried out in van-der-Pauw geometry on square shaped samples. In order to determine the charge-carrier density (and the Hall coefficient) of a film, one needs to know its thickness. I have determined the thicknesses of the ZnO films using a commercially available ellipsometry system (VASE, J.A. Woollam Co.). Ellipsometry is based on measuring the complex reflectance ratio of

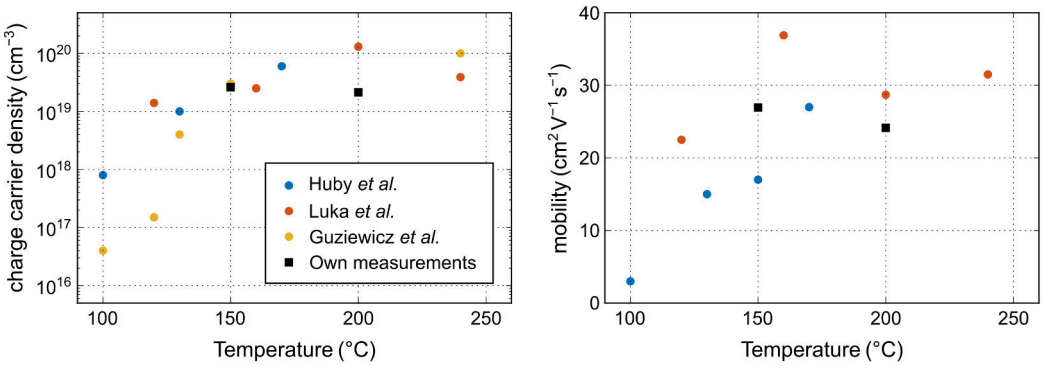

Figure 4.7: Experimentally determined charge carrier density (left) and Hall mobility (right) for ZnO thin films deposited via ALD from DEZn and water using a Savannah 100 ALD reactor. The circles correspond to values reported in the literature, the different colors denoting three different publications [126, 143, 144], while the black squares correspond to my own measurements. Two own results corresponding to two types of reference samples are shown. In both cases, 1000 ALD cycles were deposited. The film thicknesses were determined by ellipsometry on Si substrates. Reference samples for the anisotropic structures that were investigated in the probe-station based experiments were grown at 150 °C on glass substrates, compare section 5.4. The corresponding thickness of the ZnO layer is 0.185 µm. Reference samples for the integrated Hall-bar devices were grown at 200 °C on glass substrates with a thin Al_2O_3 base layer, compare section 6.3. The corresponding thickness of the ZnO layer is 0.17 µm.

a sample. Measurements were carried out on films grown on Si substrates. In order to determine the properties of the sample, ellipsometry requires corresponding material models. For ZnO, a Cauchy model was used for the spectral range in which it is transparent.

Note that, assuming a magnetic field of 1 T, the values of the mobility obtained for the thin ZnO films lead to $\lambda b \approx 2 \cdot 10^{-3} \ll 1$. Furthermore, using an effective mass of $0.27 m_e$, where m_e is the mass of an electron, and a charge-carrier velocity of $10^5\,\mathrm{m\,s^{-1}}$, one obtains a mean free path of $\sim 15\,\mathrm{nm}$. This value is smaller than the film thickness and, therefore, much smaller than the unit cell of the Hall metamaterials that I will study in the following

chapters. Hence, a classical treatment assuming weak magnetic fields on the basis of the continuity equation is justified.

Atomic layer deposition on polymers

ALD film growth on polymers can be quite different from growth on inorganic substrates, such as glass or Si (usually with a native layer of SiO_2). The main differences is the initiation of film growth. In general, two cases are distinguished: First, polymers featuring surface functional groups that can directly react with the metal precursor (such as hydroxyl groups) and, second, inert polymers which lack these functional groups [117]. As in the case of inorganic substrates, the most often studied system is the growth of Al_2O_3 from TMAl and water [145].

On polymers with a high density of reactive surface functional groups, regular growth (implying a GPC very similar to those measured for inorganic substrates) is obtained after very few deposition cycles as the metal precursor directly reacts with the polymer surface [117]. A sharp transition between the polymer and the ALD film results. All ALD layers that I have grown on three-dimensional microstructures fabricated by 3D DLW show such a sharp transition. A scanning electron micrograph of a corresponding ZnO ALD film grown from DEZn and water on a layer of polymerized IP-S is shown in Figure 4.8.

In the case of inert polymers, the metal precursor will often diffuse into the polymer beneath the polymer surface. A corresponding example is the growth of Al_2O_3 from TMAl on polypropylene (PP) [145–147]. The authors found that the uptake of precursor molecules by the polymer as well as its ability to retain the precursor depends on various factors including the porosity of the polymer and the solubility of the precursor. They have monitored these processes experimentally using a quartz crystal microbalance (QCM) sensor [145]. During subsequent exposure with water, the trapped metal precursor reacts and form subsurface clusters, which at some point, coalesce. Eventually, they form a connected layer and almost regular growth will commence. Pronounced diffusion led to rough surfaces of the resulting films and graded transitions between the polymer and the ALD film [147].

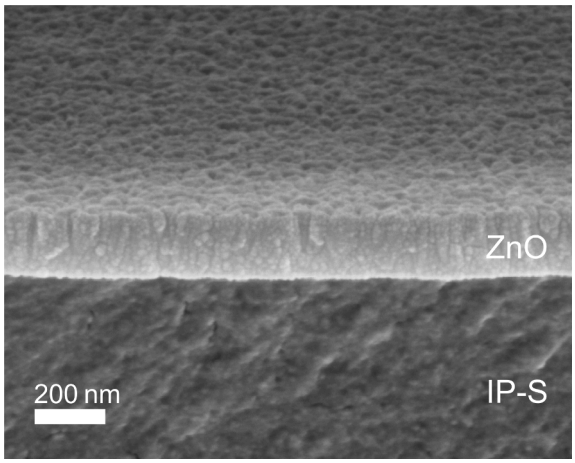

Figure 4.8: Scanning electron micrograph of an edge of a ZnO film deposited on polymerized IP-S. The film was grown from DEZn and water at a temperature of 150 °C. In total, 1000 cycles were deposited. Ellipsometry measurements on films grown on Si reference substrates yield a thickness of 185 nm. A sharp transition between the polymer and the film can be seen. The polycrystalline nature of the film is clearly visible.

Yet different growth arises from polymer backbones which enable other reaction mechanisms [117]. An example is the deposition of Al_2O_3 from TMAl on Polymethylmethacrylate (PMMA) films. In this case, it is assumed that the carbonyl groups in the PMMA backbone, which are Lewis bases, react with the TMAl molecules, which are Lewis acids, which leads to a complex reaction pathway [147].

Depending on the material and process parameters, the growth on certain polymers can also be inhibited, which can be used to selectively deposit ALD films by patterning the polymer layer using, e.g., electron-beam lithography (see [148] for a review including other approaches for selective deposition). For this purpose, the precursors should not react with the polymer nor should there be a sub-surface growth based on trapped precursor molecules as in the case of Al_2O_3 on PP fibers mentioned above. Examples include the selective deposition of TiO_2 [149] and Ir, Pt, Ru, and TiO_2 [150] on patterned PMMA.

In principle, selective ALD of ZnO could be used for avoiding short-circuits in the fabrication of metamaterial Hall-bar devices, see chapter 6. However,

(polymer) mask layers often delay the growth rather than preventing it completely. In the case of ZnO on PMMA, at low temperatures, a growth delay of several hundred cycles with subsequent uniform growth has been reported [127]. Obtaining a reliable passivation for thick layers without affecting film growth in the vicinity of the masking layer is very challenging and my own corresponding efforts have not been successful. Consequently, for contacting the Hall bars in a permanent fashion, a different approach based on transferring the Hall bar from a substrate to a printed circuit board after ALD has been chosen, see section 6.1.

In the future, it might be possible to deposit ALD films selectively on certain parts of three-dimensional polymer microstructures, for example, in order to locally tune their mechanical properties. A potential realization might be based on two resists, only one of which inhibiting the growth of layers via ALD. Alternatively, passivating one of the resists via a functionalization, potentially based on thiol-ene click chemistry [151], might be viable as well.

4.3 Electron-beam physical vapor deposition

Electron-beam physical vapor deposition (EB-PVD), also called electron-beam evaporation, is a well-established method for the directional deposition of thin films [152–154]. The process is based on the evaporation of a target material using a high-energy electron beam.

Deposition is usually performed under high or ultra-high vacuum conditions. The electron source is typically a tungsten filament. A high voltage is used to accelerate the electrons. Often, the electron source is placed below the target, implying that the electron beam needs to be deflected, which is achieved using a strong magnetic field. Additional electric fields are used to precisely control and modulate the position of spot of the electron beam on the target. As the electron beam hits the target, the material is heated and evaporates coating everything within line-of-sight. Due to the high or even ultra-high vacuum conditions, almost no collisions with remaining gas molecules occur and the vaporized material travels in straight lines. This highly directional behavior, which is illustrated in Figure 4.4, is in sharp contrast to the conformal behavior of ALD and implies that structures cast a shadow, which vastly facilitates lift-off processes. Furthermore, it enables a number of more specific applications, for example, the fabrication of Josephson junctions using suspended masks and a series of depositions at different angles of incidence [155]. In other cases, this property can be undesired.

I have used EB-PVD to make Ohmic contacts to metamaterial Hall bar structures via the deposition of titanium/gold bilayers, see section 5.1. Using the fact that the technique is highly directional, the bilayers are deposited on specific parts of the structure only, i.e., on the areas that serve as contacts.

It is well known that Ohmic contacts on ZnO can be obtained with non-alloyed bilayers of titanium and gold with titanium forming the actual contact and gold acting as a protective layer [143, 156, 157]. Without this protective layer, the titanium surface would oxidize quickly. For the same reason, venting in between the depositions of titanium and gold, thereby exposing the titanium surface to the atmosphere, has to be avoided. Titanium has the convenient property of adhering well to many substrates.

Other methods for the directional deposition of thin films, such as thermal evaporation [153], exist as well. EB-PVD was chosen as it is excellently suited

for the deposition of titanium and gold [158]. In the case of gold, ejection of small liquid droplets, so-called spitting, can occur. This undesired effect is, however, not of concern in my case.

In this thesis, I have used a custom-built EB-PVD setup based on a commercially available rotary evaporation source (e-vap 4000 UHV, MDC Vacuum Products, LLC). Deposition was carried out at pressures below $5 \cdot 10^{-7}$ mbar, as measured right before the deposition, using an acceleration voltage of 8 kV. The deposition rate of about 1 Å s^{-1} was monitored using two quartz crystal sensors.

Chapter 5

5 Probe-station based experiments

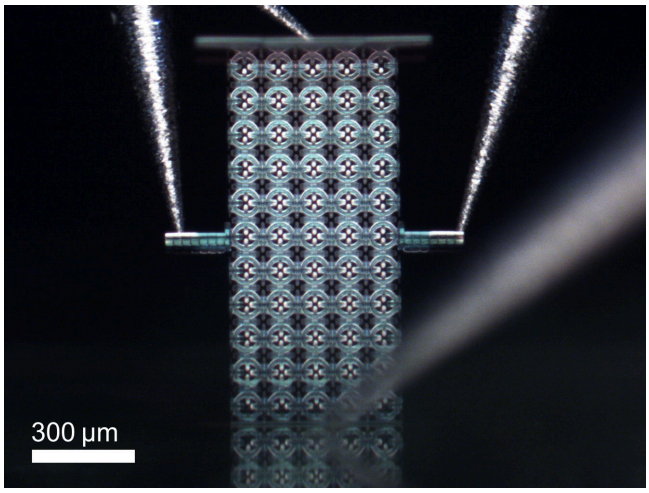

Light micrograph of a metamaterial Hall bar in the measurement setup.

In this chapter, I will present experimental results on the fabrication and characterization of microscale Hall metamaterials. Fabrication of the structures is based on three-dimensional laser lithography and atomic-layer deposition. Characterization was performed using a dedicated magneto-electric probe station. Two different metamaterial designs were studied. First, the sign-inversion of the effective Hall coefficient in chainmail-like metamaterials was confirmed experimentally. Second, anisotropic structures were studied, which led to the experimental observation of the parallel Hall effect.

5.1 Fabrication

In chapter 3, I have introduced a variety of single-constituent porous Hall metamaterials. For two of those metamaterials, I will in the following discuss the fabrication of corresponding microscale metamaterial Hall-bar structures. The measurement setup used for the characterization of these metamaterial structures and the experimental results are described in subsequent sections.

The first structure is the chainmail-inspired metamaterial exhibiting a sign-inversion of the effective Hall coefficient. The second structure is the anisotropic metamaterial that allows to control the orientation of the macroscopic Hall electric field in the plane perpendicular to the direction of current flow. This second metamaterial, furthermore, exhibits the parallel Hall effect. The following summary is based on two of my previous publications, on the sign-inversion of the effective Hall coefficient [73] and the parallel Hall effect [82].

Fabrication of the metamaterial Hall bars is performed in a multi-step process, which is identical for both structures. The corresponding methods have been described in chapter 4. Fabrication starts with 3D DLW of electrically insulating metamaterial polymer templates on glass substrates. These templates are subsequently conformally coated with a thin film of n-type ZnO using ALD. In order to obtain Ohmic contacts to the structures, they are coated with a bilayer of Ti and Au.

For both structures, the unit cell size is in the order of 100 µm. The overall length of the Hall bars is in the order of 1-2 mm. As already pointed out, the effects considered in this thesis are stationary. Hence, there is no restriction on the size of the unit cell as long as the samples are composed of a large number of unit cells. Therefore, the unit cells might be much larger.

However, several reasons speak against an experimental realization of much larger unit cells. First, for a given current flow, the Hall voltage scales inversely with sample thickness. Hence, upon reducing all Hall-bar dimensions simultaneously, the current-related sensitivity, compare section 2.1, increases. Second, fabrication of such complex three-dimensional semiconductor structures on a larger length scale is not necessarily much simpler. Furthermore, in order to measure the effect, one would need a strong magnetic field that is homogeneous over a large volume. Third, po-

tential applications, compare section 3.3, require the Hall bar to be small.

In the following, I will go through the fabrication step-by-step:

1. ITO-coated glass substrates are pretreated in order to promote adhesion of the polymer microstructures. Following an air plasma treatment for 20 min in order to activate the surface, the substrates are immersed in a 1 mM solution of 3-(trimethoxysilyl)propyl methacrylate (CAS 2530-85-0) in toluene. Subsequently, they are briefly immersed in water and dried using a nitrogen spray gun.

2. Using 3D DLW, electrically insulating metamaterial Hall-bar templates are fabricated on the glass substrates. The ITO layer on the substrates aids in the determination of the position of the interface between the photoresist and the substrate by providing a refractive-index contrast. The Hall bars are fabricated in upright orientation. Other orientations may lead to short-circuits, as not only the template but also the substrate is coated with an electrically conductive layer during the subsequent ALD step. Furthermore, side-arms, which aid as contacts for the measurement of the Hall voltage, and a roof-like structure, which casts a shadow during the subsequent EB-PVD step, are added. The side-arms have a notch, which facilitates contacting. In order to avoid warping, compare section 4.1, the side-arms and the roof-like structure are fabricated in a segment-wise way. A commercial photoresist, IP-S (Nanoscribe GmbH), and a 25× NA 0.8 objective (LCI Plan-Neofluar Imm Corr DIC M27, Carl Zeiss Microscopy GmbH) are used. The discretization of the structure is performed using a slicing distance of 0.5 µm and a hatching distance of 0.2 µm.

3. In order to wash away the remaining liquid photoresist, the samples are immersed in the developer, mr-Dev 600 (based on 1-methoxy-2-propanyl acetate/PGMEA, micro resist technology GmbH), for 20 min, followed by short immersions in acetone, isopropyl alcohol, and water.

4. Using ALD, the templates are conformally coated with a thin film of ZnO. Deposition of 1000 cycles is carried out at a temperature of 150 °C using DEZn and water as precursors. The ZnO film has a thickness

of 185 nm, as determined by ellipsometry measurements on reference films grown on Si substrates.

5. Using EB-PVD, the sample is coated with a bilayer of Ti and Au with thicknesses of 30 nm and 100 nm, respectively. As pointed out in section 4.3, EB-PVD is a directional deposition technique, which implies that structures cast a shadow. The roof-like structure on the top prevents the actual metamaterial from being coated. The metal film is only deposited on the parts which serve as contacts. These parts are the substrate and the top of the structure, for imposing the current flow, and the two side-arms, for measuring the Hall voltage.

5.2 Measurement setup

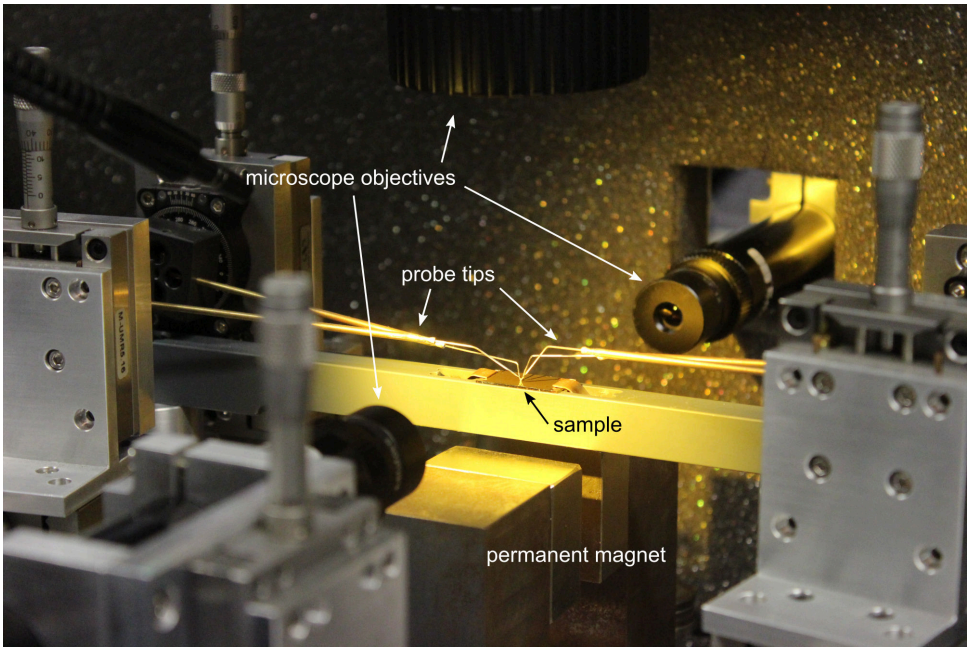

Figure 5.1: Photograph of the probe-station based measurement setup (front view). The sample is placed on a sample holder and contacted using four probe tips. The permanent magnet, which is used to impose the magnetic field, is in its lower position. The sample is observed from the front and the back using digital microscopes, and from the top using a stereo microscope.

Measurements are performed using a custom-built magneto-electric probe station. Front and top views of the measurement setup are shown in Figure 5.1 and Figure 5.2, respectively. The sample is fixated on a dedicated sample holder. A source-measurement unit (B2901A, Keysight Technologies Inc.) is used for imposing electric currents and measuring voltages. Electrical contact to the structure is made via four tungsten probe tips with a tip diameter of 20 µm (SE-20TB, Lucas Signatone Corp.) and corresponding probe tip holders (U-E, Lucas Signatone Corp.). The position of the probe tips is controlled using four manual three-axis stages (each based on three linear stages, M-UMR5.16, Newport Corp.). Each of the probe tips can be

tilted using a rotation stage (MSRP01/M, Thorlabs). The sample is observed from the front and the back via two digital optical microscopes using long working-distance objectives (CF 3x and CF 2x, Mitutoyo Corp.). Furthermore, it is observed from the top using a stereo microscope (MZ12.5, Leica GmbH). During contacting, the resistance is monitored, which indicates whether contact has been made. A custom-built computer-controlled switch system allows to realize any possible connection between the source-measurement unit and the probe tips. This system enables a fast and simple characterization of the contacts by measuring the I-V curves for each combination of contacts. The actual Hall measurements are performed by imposing a current flow (between the bottom/substrate and top contact) and a magnetic field, and measuring the corresponding transversal voltage (between the side contacts).

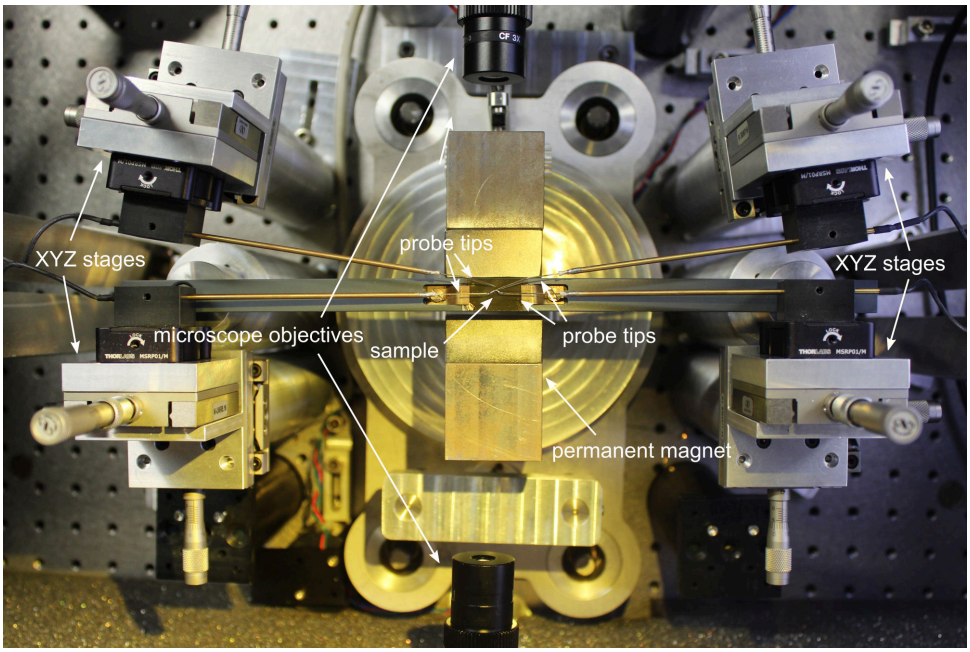

Figure 5.2: Photograph of the probe-station based measurement setup (top view).

The magnetic field is imposed using a permanent magnet. Using a stepper motor (QSH 4218-049, TRINAMIC Motion Control GmbH & Co. KG),

the magnet can be moved vertically. In the upper magnet position, the samples are subject to a homogeneous magnetic field of $\pm 0.83\,\mathrm{T}$ as measured using a commercial Hall sensor (HGT-2010, Lake Shore Cryotronics, Inc.). In the lower magnet position, the sample can be observed via the digital microscopes. The residual magnetic flux density at the sample location is $\pm 0.3\,\mathrm{T}$.

As discussed in section 2.1, the experimentally measured transversal voltage is the sum of the Hall voltage and a magnetic-field independent offset voltage. This offset voltage originates from imperfections and asymmetries of the sample. In order to extract the Hall voltage, the magnetic field is inverted during the measurement. This sign-change is achieved by employing a second stepper motor (QSH 4218-035, TRINAMIC Motion Control GmbH & Co. KG), which allows for a 180° rotation of the magnet about the x-axis. In order to rotate the permanent magnet, it has to be moved to its lower position. Otherwise, the magnet would collide with the probe tips and the sample fixture during rotation. In principle, an electro-magnet could have been employed as well. However, most systems based on electro-magnets do not offer suitable optical access to the sample, which is necessary for making the contacts.

A personal computer is used to control the source-measurement unit, switch system, and stepper motors. For the stepper motors, two commercial driver modules (TMCM-1110, "StepRocker", TRINAMIC Motion Control GmbH & Co. KG) are employed. A dedicated software serves for data acquisition and subsequent data processing.

5.3 Sign-inversion of the effective Hall coefficient

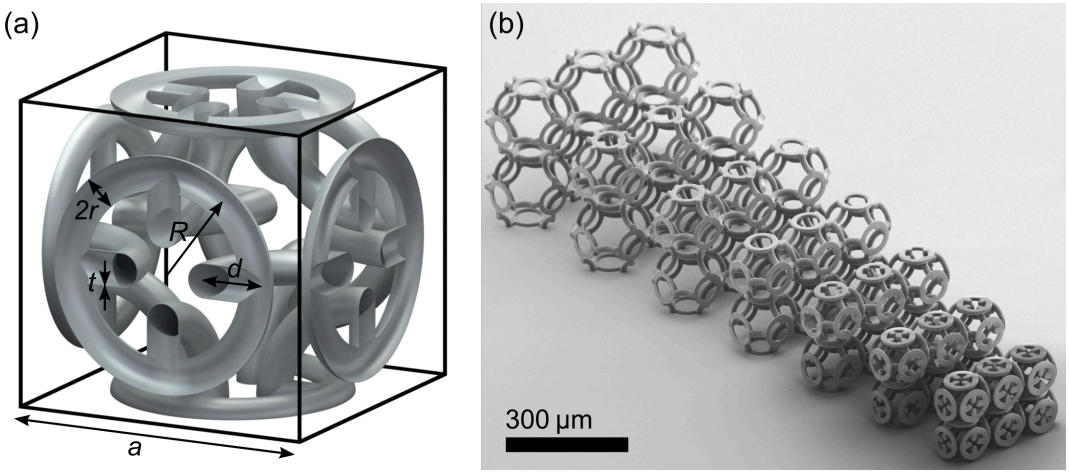

Figure 5.3: (a) Schematic illustration of a unit cell of the hollow version of the chainmail-inspired metamaterial exhibiting a sign-inversion of the effective Hall coefficient, compare section 3.2. (b) Scanning electron micrograph of corresponding polymer unit-cell templates fabricated via 3D DLW on a glass substrate. The structures correspond to different values of the distance parameter, d, which leads to different values of the lattice constant, $a = 4R + 2d$. The distance parameter increases from the bottom-right ($d = -22\,\mu\text{m}$) to the top-left ($d = 4\,\mu\text{m}$). Other parameters are $R = 36\,\mu\text{m}$ and $r = 6\,\mu\text{m}$. Adapted from [73, 159].

In the following, I will discuss my experimental results on the sign-inversion of the effective Hall coefficient in chainmail-inspired metamaterials. The structure consists of interlinked tori that are connected by small cylinder segments. Theoretical aspects have been discussed in section 3.2. An intuitive explanation for the sign-inversion was given there as well. The sign-inversion is theoretically expected for negative values of the distance parameter, d, with large modulus. As pointed out previously, the fabrication process leads to a structure that is hollow in an electrical sense. A unit cell of this hollow version of the metamaterial is shown in Figure 5.3(a). Fabrication of the corresponding metamaterial Hall bars was performed as described

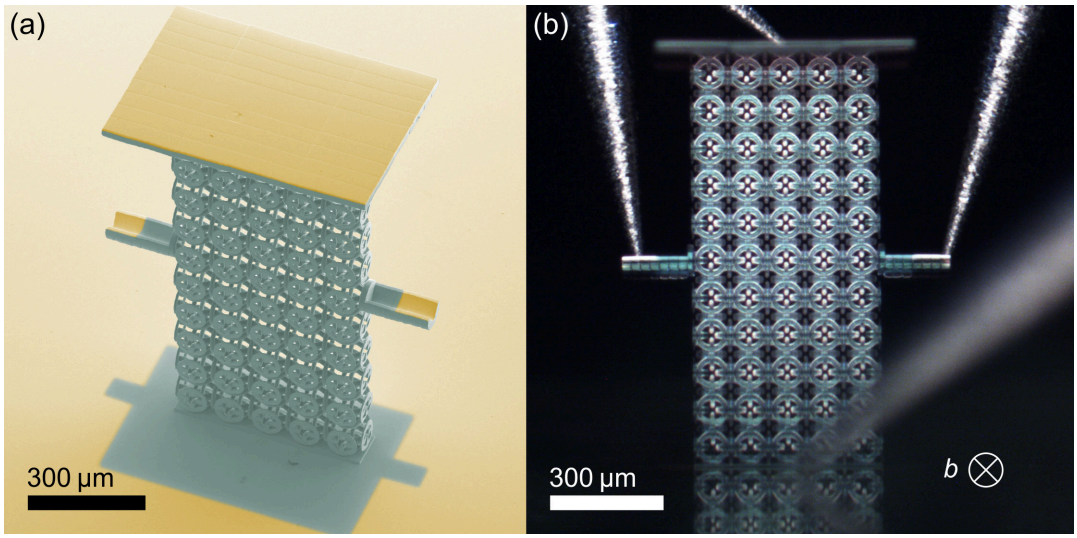

Figure 5.4: (a) Scanning electron micrograph of a chainmail-inspired metamaterial Hall bar after 3D DLW, ALD, and EB-PVD. The micrograph has been colored for clarity. The Hall bar is composed of $11 \times 5 \times 1$ unit cells. The shadow cast during the EB-PVD step by the roof-like structure and the side arms is clearly visible on the substrate. The distance parameter is $d = -22\,\mu\text{m}$. The other parameters are $R = 36\,\mu\text{m}$ and $r = 6\,\mu\text{m}$. (b) Light micrograph of a metamaterial Hall bar in the probe-station setup. The magnetic field direction is schematically indicated. The four tungsten probe tips are clearly visible. The probe tip that is used to contact the substrate is out of focus. Adapted from [73].

in section 5.1. The Hall-bars are composed of $N_x \times N_y \times N_z = 11 \times 5 \times 1$ unit cells. Design parameters of the structure are $R = 36\,\mu\text{m}$ and $r = 6\,\mu\text{m}$. For the distance parameter, d, values ranging from $-22\,\mu\text{m}$ to $4\,\mu\text{m}$ were chosen, which leads to different values of the lattice constant, a, that is given by $a = 4R + 2d$. A scanning electron micrograph of corresponding polymer templates is shown in Figure 5.3(b). A colored scanning electron micrograph of a completed Hall bar is shown in Figure 5.4(a).

Following fabrication, I have performed Hall measurements on the structures using the setup described in section 5.2. A light micrograph of a Hall bar in the setup is shown in Figure 5.4(a). In a first step, electrical contact to the structure is made via the four tungsten probe tips. Thereafter, the quality

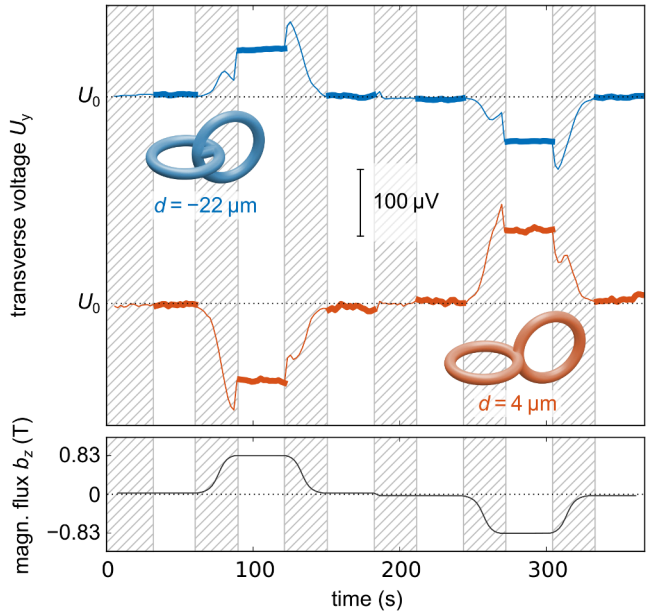

Figure 5.5: Measured transversal voltage, U_y, versus time for two metamaterial Hall bar samples corresponding to distance parameters of $d = 4\,\mu m$ and $d = -22\,\mu m$ at a current of $0.5\,\mu A$. A magnetic field of $b_z = \pm 0.83\,T$ is imposed using a permanent magnet. During the measurement, the magnetic field is inverted by moving and rotating the magnet. A corresponding reference measurement is shown in the lower part of the figure. The shaded regions correspond to the time intervals in which the magnet is moving. Peaks in the transversal voltage arise from magnetic induction due to this movement. The Hall voltage is inferred from the difference in transversal voltage for $b_z = +0.83\,T$ and $b_z = -0.83\,T$. Design parameters are as in Figure 5.4. Adapted from [73].

of the contacts is checked by measuring I-V curves between each pair of contacts. Once proper contact has been made, the contacts exhibit Ohmic behavior. During the following Hall measurements, these I-V measurements are regularly repeated. Sometimes, readjustment of the contacts, especially the side-contacts, is necessary.

Hall measurements were performed by measuring the transversal voltage, U_y, versus time for a given current, I, at a magnetic field of $b_z = \pm 0.83\,T$. The substrate and the top of the structures serve as contacts for imposing

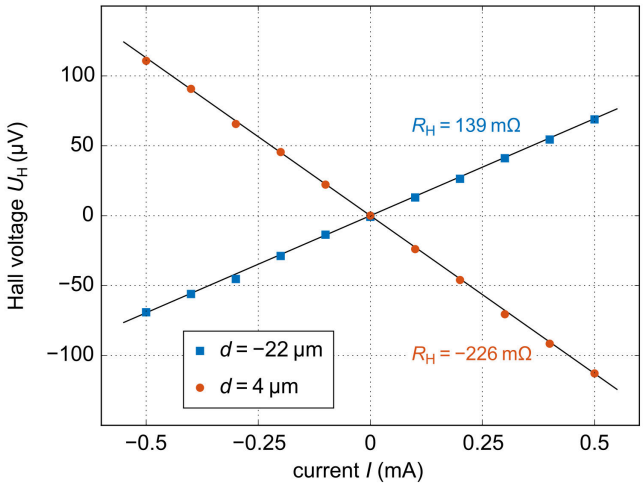

Figure 5.6: Extracted Hall voltage, U_H, versus imposed current, I, for the same two samples as in Figure 5.5, corresponding to distance parameters of $d = 4\,\mu m$ and $d = -22\,\mu m$. The Hall voltage shows the expected proportional behavior, $U_H \propto I$. The straight black lines correspond to fits, assuming a proportional behavior, which are used to determine the Hall resistances, R_H. For the sample corresponding to $d = 4\,\mu m$, the Hall resistance is negative, which implies a negative effective Hall coefficient. For the sample corresponding to $d = -22\,\mu m$, the Hall resistance is positive, which implies a positive and, hence, sign-inverted effective Hall coefficient. Adapted from [73].

the current flow. The two side arms serve as contacts for measuring the transversal voltage.

The measurement procedure is as follows. Initially, the magnet is in its lower position. It is then moved to its upper position and the sample is subject to a magnetic field of $b_z = +0.83\,T$. Spikes in the transversal voltage are caused by induction in the loop formed by the measurement wires due to the movement of the magnet. After a certain time, the magnet is lowered and rotated by 180°, which reverses the sign of the magnetic field. Subsequently, these steps are repeated for the now inverted magnetic field.

This procedure leads to raw data as those shown in Figure 5.5. The Hall voltage, U_H, is extracted from the difference in transversal voltage for the

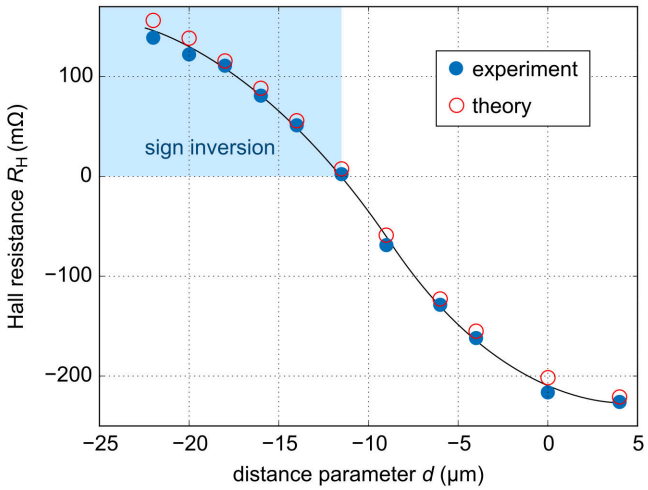

Figure 5.7: Experimentally determined Hall resistances (blue dots) for samples corresponding to different values of the distance parameter, d. The other parameters are as in Figure 5.4. For $d < 12\,\mu\text{m}$, the Hall resistance and, hence, the effective Hall coefficient is sign-inverted. The open red dots correspond to numerical calculations. The black curve is a guide to the eye. Adapted from [73].

two different magnetic field orientations,

$$U_\text{H} = \left(U_y(b_z = +0.83\,\text{T}) - U_y(b_z = -0.83\,\text{T})\right)/2. \tag{5.1}$$

Repeating such measurements for different currents, I, leads to the results shown in Figure 5.6. Results for two samples corresponding to distance parameters of $d = -22\,\mu\text{m}$ and $d = 4\,\mu\text{m}$ are shown. The Hall resistance, $R_\text{H} = U_\text{H}/I$, of the samples for a magnetic field of $b_z = 0.83\,\text{T}$ is obtained via a fit. Note that the Hall coefficient of the constituent material, ZnO, is negative. Hence, naively, one would expect to measure a negative Hall resistance. For the sample corresponding to non-interlinked tori ($d = 4\,\mu\text{m}$), the Hall resistance is indeed negative. For the sample corresponding to interlinked tori ($d = -22\,\mu\text{m}$), however, the Hall resistance is positive and the corresponding effective Hall coefficient, $A^*_\text{H} = R_\text{H} L_z\,(0.83\,\text{T})^{-1}$, is positive and, therefore, sign-inverted.

The extracted Hall resistances for metamaterial Hall bars corresponding to different values of the distance parameter, d, are shown in Figure 5.7. As

expected from theory, for negative values of the distance parameter with large modulus, the Hall resistance and, hence, the effective Hall coefficient becomes sign-inverted. In between, one can continuously tune the effective Hall coefficient by adjusting d. The experimental results show a zero crossing of the Hall resistance at around $d = -12\,\mu\text{m}$. Corresponding numerical calculations for the finite Hall-bar geometry have been performed as described in section 3.1. In order to obtain agreement between the experimental results and the calculations, one has to assume that the radius r is slightly larger than the design value of $r = 6\,\mu\text{m}$. These deviations are likely caused by the finite size and elongated shape of the voxel, which leads to slightly ellipsoidal cross-sections of the cylinder and tori. The numerical results shown in Figure 5.7 are obtained for a choice of $r = 7.5\,\mu\text{m}$ and the other geometry parameters being identical to the design values. The Hall coefficient of the constituent material, A_{H}^0, has been used as fit parameter, yielding $A_{\text{H}}^0 = 3.8 \cdot 10^{-7}\text{m}^3\,\text{C}^{-1}$ [73].

In summary, the experimental results clearly show a sign-inversion of the effective Hall coefficient, which can be continuously tuned from positive to negative values by adjusting a geometry parameter. The experiments confirm previous theoretical results, compare section 3.2, and are in agreement with corresponding numerical calculations.

5.4 Parallel Hall effect

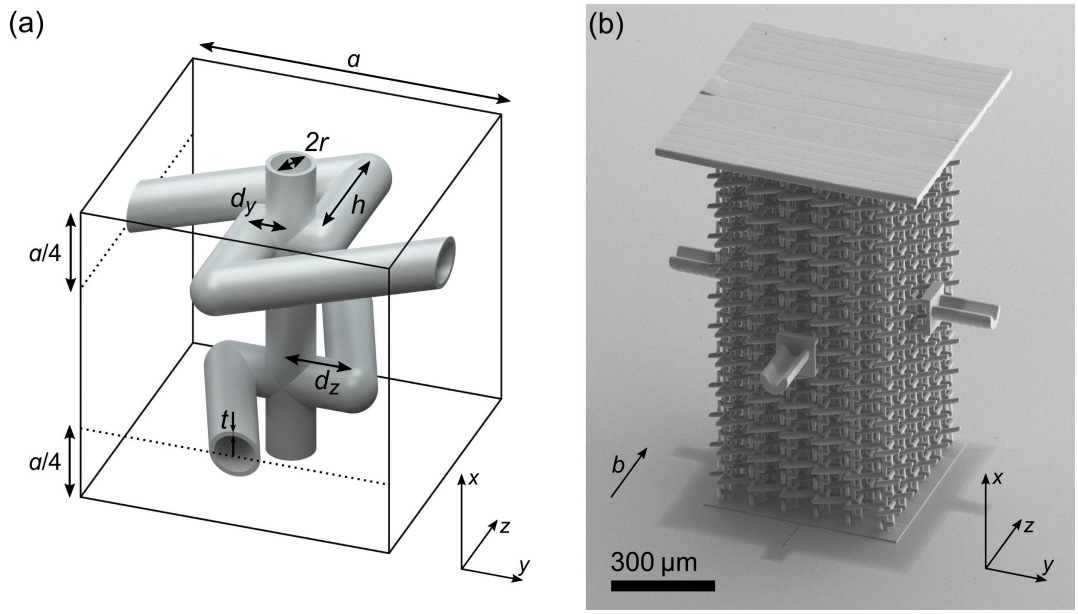

Figure 5.8: (a) Illustration of a unit cell of the hollow version of the anisotropic metamaterial introduced in [72], see also section 3.3. For a macroscopic current in the x-direction and a magnetic field in the z-direction, the structure exhibits macroscopic Hall electric field components perpendicular and parallel to the magnetic field, which can be adjusted via the geometry parameters d_y and d_z and which lead to two corresponding Hall voltages. (b) Scanning electron micrograph of a corresponding metamaterial Hall bar composed of $12 \times 6 \times 6$ unit cells after 3D DLW, ALD, and EB-PVD. The Hall bar has four side-contacts for measuring the two Hall voltages, U_{H}^{y} and U_{H}^{z}. Three of these side-contacts are visible here. Parameters are $a = 100\,\mu\mathrm{m}$, $r = 6.25\,\mu\mathrm{m}$, $h = 40\,\mu\mathrm{m}$, $d_y = -10\,\mu\mathrm{m}$, and $d_z = 20\,\mu\mathrm{m}$. Adapted from [82].

In the following, I will present experimental results on anisotropic structures and the parallel Hall effect that were previously published in [82]. Sample fabrication and measurements were performed by Vittoria Schuster in the course of her master's thesis that I have supervised [160]. Theoretical aspects are discussed in section 3.3. An illustration of a unit cell of

the realized anisotropic metamaterial is shown in Figure 5.8(a). Consider a corresponding metamaterial Hall bar. For a magnetic field in the z-direction and a current flow in the x-direction, the macroscopic Hall electric field has components along the y-direction and the z-direction, perpendicular and parallel to the magnetic field, respectively. These two components can be tuned by adjusting the geometry parameters d_y and d_z, which gives control over the orientation of the macroscopic Hall electric field in the yz-plane. The two Hall electric field components lead to two corresponding Hall voltages, the "orthogonal" Hall voltage, U_{H}^{y}, and the "parallel" Hall voltage, U_{H}^{z}, which can be measured experimentally and are directly related to the corresponding two components of the effective Hall tensor, compare section 3.3. According to theory, all other components of the effective Hall tensor are comparably small.

Fabrication of the metamaterial Hall bars with $N_x \times N_y \times N_z = 12 \times 6 \times 6$ unit cells was performed as described in section 5.1. The dimensions of the Hall bar, L_x, L_y, and L_z, are directly related to the number of unit cells in the respective direction, $L_x = N_x a$, $L_y = N_y a$, and $L_z = N_z a$. In contrast to the chainmail-inspired structures, the Hall bars have four pick-up contacts for measuring the two Hall voltages. A scanning electron micrograph of such a metamaterial Hall bar is shown in Figure 5.8(b). Four parameter combinations, $d_y = \pm 10\,\mu\mathrm{m}$, $d_z = \pm 20\,\mu\mathrm{m}$, corresponding to the four sign combinations of the two Hall voltages were realized.

Measurements were performed as for the chainmail-inspired structures using the probe-station setup described in section 5.2. Since the probe station has four probe tips only, the two transversal voltages corresponding to the two Hall voltages are measured sequentially. From these measurements, the Hall resistances, R_{H}^{y} and R_{H}^{z}, are inferred. The corresponding results for the four parameter combinations are shown in Figure 5.9.

The results clearly show a large parallel Hall resistance, providing experimental evidence that the material exhibits the parallel Hall effect. Furthermore, all four sign combinations of R_{H}^{y} and R_{H}^{z} can be realized by choosing d_y and d_z appropriately. More precisely, as predicted by theory, compare section 3.3, $\mathrm{sign}(R_{\mathrm{H}}^{y}) = \mathrm{sign}(d_y)$ and $\mathrm{sign}(R_{\mathrm{H}}^{z}) = \mathrm{sign}(d_z)$. Moreover, as expected, R_{H}^{y} and R_{H}^{z} are independent of d_z and d_y, respectively. As stated

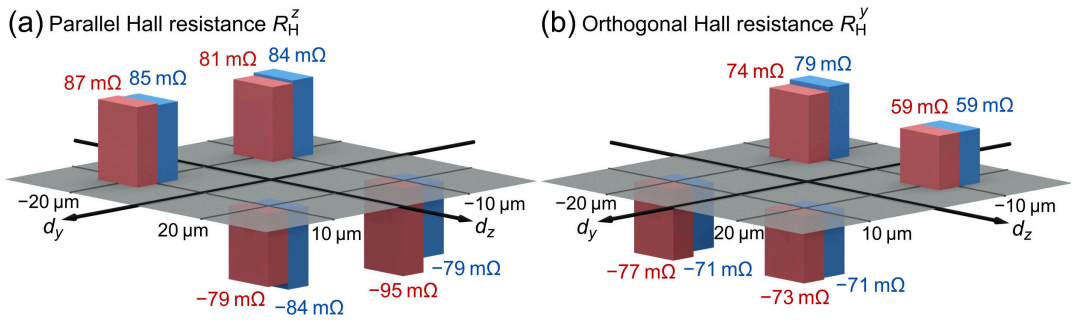

Figure 5.9: Experimentally determined Hall resistances for anisotropic metamaterial Hall bars corresponding to four different parameter combinations, $d_y = \pm 10\,\mu\text{m}$ and $d_z = \pm 20\,\mu\text{m}$. Other design parameters are as in Figure 5.8. The blue and red bars correspond to two generations of nominally identical samples. The magnetic field is $|b_z| = 0.83\,\text{T}$. (a) Parallel Hall resistance, R_H^z. (b) Orthogonal Hall resistance, R_H^y. Adapted from [82].

above, the four different sign-combinations correspond to four orientations of the macroscopic Hall electric field in the yz-plane. As the modulus of the Hall resistances is comparable, the orientations are approximately separated by quarter turns.

For a quantitative comparison of the results with theory, one needs to know the Hall coefficient of the constituent material, i.e., of the bare ZnO film, A_H^0. Corresponding van-der-Pauw measurements were carried out on films grown on square-shaped glass substrates with dimensions of $10\,\text{mm} \times 10\,\text{mm}$. The corners of the samples, which serve as contacts, were metallized using the EB-PVD process that was used for the metamaterial samples and a shadow mask. The measurements, which were performed using the same probe-station based setup, yield $A_H^0 = -2.5 \cdot 10^{-7}\,\text{m}^3\,\text{C}^{-1}$. Using this result, the Hall voltages can be estimated analytically, compare section 3.3. For the design parameters and a magnetic field of 0.83 T, see Figure 5.8, Equations 3.34 and 3.33 yield $\left|R_H^z\right| = \left|R_H^y\right| = 59\,\text{m}\Omega$ [82].

As pointed out in section 3.3, the parallel Hall resistance, as well as the parallel Hall voltage, scales inversely with the thickness of the Hall bar perpendicular to the magnetic field, $R_H^z \propto U_H^z \propto L_y^{-1}$, compare Equation 3.34, [82]. This behavior is in contrast to the behavior of the ordinary orthogonal Hall resistance, which scales inversely with the thickness in the direction

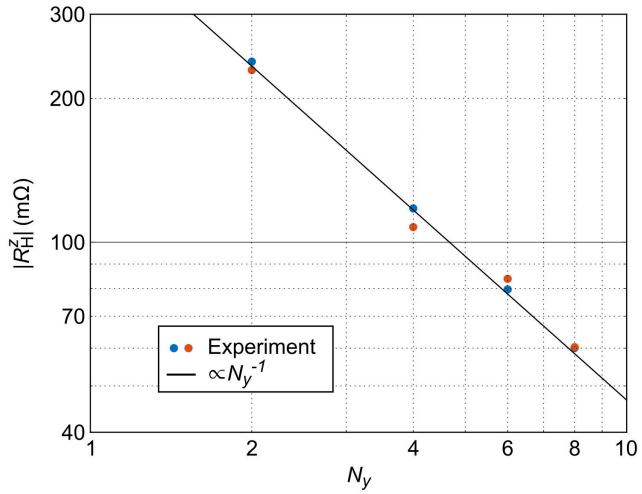

Figure 5.10: Double-logarithmic representation of the experimentally determined parallel Hall resistances, R_{H}^{z}, for metamaterial Hall bars with different values of N_y, the number of unit cells perpendicular to the magnetic field. The number of unit cells along the other two directions was kept fixed, $N_x = 12$ and $N_z = 6$. The blue and red dots are the results for two nominally identical sample generations. The straight black line corresponds to a scaling of $R_{\mathrm{H}}^{z} \propto N_y^{-1}$. For $N_y = 8$, the two dots overlap and only one of them is clearly visible. Design parameters are $a = 100\,\mu\mathrm{m}$, $r = 6.25\,\mu\mathrm{m}$, $h = 40\,\mu\mathrm{m}$, $d_y = 10\,\mu\mathrm{m}$, and $d_z = 20\,\mu\mathrm{m}$. The magnetic field is $|b_z| = 0.83\,\mathrm{T}$. Adapted from [82].

of the magnetic field, $R_{\mathrm{H}}^{y} \propto L_z^{-1}$, compare Equation 3.33. In a series of experiments, this unusual scaling of the parallel Hall voltage was closely examined [82]. Metamaterial Hall bars corresponding to different values of N_y were fabricated and characterized as described above. As the parallel Hall resistance was determined only, the Hall bars were fabricated with two instead of four pick-up contacts. The corresponding experimentally determined parallel Hall resistances are shown in Figure 5.10. The results clearly show the expected scaling, $R_{\mathrm{H}}^{z} \propto L_y^{-1}$.

In summary, the results provide clear evidence for the parallel Hall effect in anisotropic metamaterials. As expected from theory, the orthogonal and parallel Hall resistance can be tailored by adjusting corresponding geometry

parameters. The results are well described by a simple analytical model. Furthermore, the parallel Hall resistance shows the expected dependence on the Hall-bar dimensions.

Chapter 6

6 Hall-bar devices

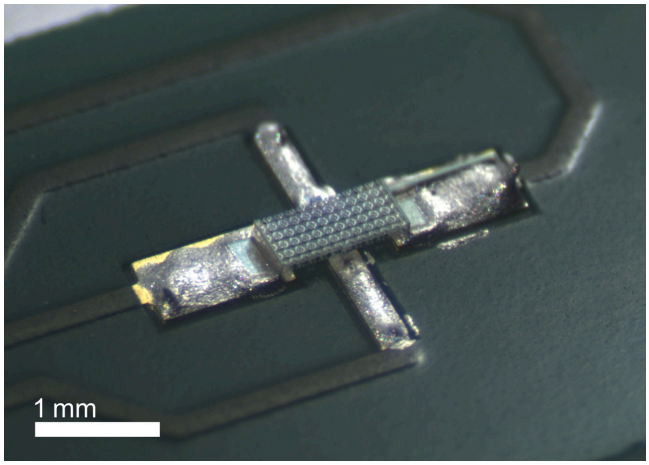

Light micrograph of a metamaterial Hall-bar structure contacted on a printed circuit board.

In this chapter, I will introduce a method of making permanent contact to metamaterial Hall-bar microstructures on printed circuit boards. This approach drastically simplifies measurements and, therefore, enables refined characterization of the metamaterial's properties. As an example, I have used it to investigate the role of unit cell orientation for metamaterials with cubic symmetry. Furthermore, such means of permanently contacting metamaterial Hall bars are a crucial step towards potential applications.

The measurement approach based on a dedicated magneto-electric probe station described in chapter 5 allowed for the reliable characterization of metamaterial Hall-bar samples and enabled the experimental observation of the sign-inversion of the effective Hall coefficient and the parallel Hall effect. However, it has certain drawbacks. For example, the mechanical way of contacting the samples limits their lifetime. Moreover, the setup is fairly complicated. Conventional Hall measurement setups, which are wide-spread and commercially available, would pose a much simpler tool for sample characterization if a simple and reliable method of contacting the structures was available. Furthermore, potential applications of Hall metamaterials, such as sensors for the circulation of a magnetic field as introduced in section 3.3, require a method of permanently contacting the samples.

In the following, I will introduce such a method, which combines the previously used fabrication strategy, ALD of thin ZnO layers on electrically insulating metamaterial Hall-bar templates obtained via 3D DLW, with a manual transfer of the Hall bars to prefabricated printed circuit boards (PCB), which are ubiquitous in everyday electronics. I will refer to such permanently contacted metamaterial Hall bars as metamaterial Hall-bar devices. The description of the method and the corresponding experimental results follows one of my previous publications [159].

6.1 Fabrication

A key property of ALD is that it coats all surfaces conformally. While this property is highly desired for coating the metamaterial Hall-bar templates, it unfortunately also leads to an electrically conductive coating of the substrate, which, depending on the Hall-bar geometry and orientation, may lead to short-circuits. As mentioned in section 5.1, this side effect is the reason why the samples for the probe-station based experiments were fabricated in upright orientation. If one aims at making permanent contact to the structures, this problem poses a major challenge in the search of a suitable fabrication strategy. One possible solution is to pattern the ALD film on the substrate. Two options of patterning the film have been investigated experimentally.

The first strategy, which was studied by Jessica Meier in the scope of her bachelor's thesis [124], that I have supervised, is based on a lift-off process. In a first step, the substrate is coated with a thin photoresist layer, which is subsequently structured via conventional photolithography. Following 3D DLW and ALD, the photoresist is removed with the aid of an organic solvent which lifts the ALD layer on top of the photoresist off the substrate. Lift-off based patterning of ALD films had previously been demonstrated [161]. We were able to reproduce these results and successfully used a lift-off process to pattern thin ZnO films. However, combining this technique with the 3D DLW process proved to by very challenging [124]. Essentially, the lift-off requires quite harsh conditions which lead to an unintended detachment of the metamaterial microstructures.

The second strategy is based on a selective passivation of the substrate, see section 4.2. As a passivating layer, I have mainly studied thin PMMA films structured via electron-beam lithography. Using this strategy, I was able to obtain a spatially selective passivation against the growth of ZnO. However, the PMMA films affected the growth in their vicinity and led to poor electrical properties of the ZnO films.

Hence, instead of patterning the ZnO film, I have used the aforementioned method that is based on transferring the structure to a different substrate. As a first structure, I have chosen the chainmail-like metamaterial, but the method may readily be applied to other structures as well. As previously, the unit cell size is about 100 µm while the total length of the Hall bar is in the order of 1-2 mm.

In the following, I will go through the fabrication of the chainmail-like metamaterial Hall-bar devices step by step. Different stages of the sample fabrication process are, furthermore, illustrated in Figure 6.1.

1. Using 3D DLW, a Hall bar is fabricated in upright orientation on a Si wafer substrate. In addition to the Hall bar itself, four pedestals, which serve for contacting the structure, and a handling arm with a cross section of 50 µm × 100 µm and a length of 1 mm are fabricated. The only mechanical connection to the substrate is the narrow edge of one of the pedestals with a width of 20 µm. There is no pretreatment of the substrates in order to promote adhesion, as it was used for the

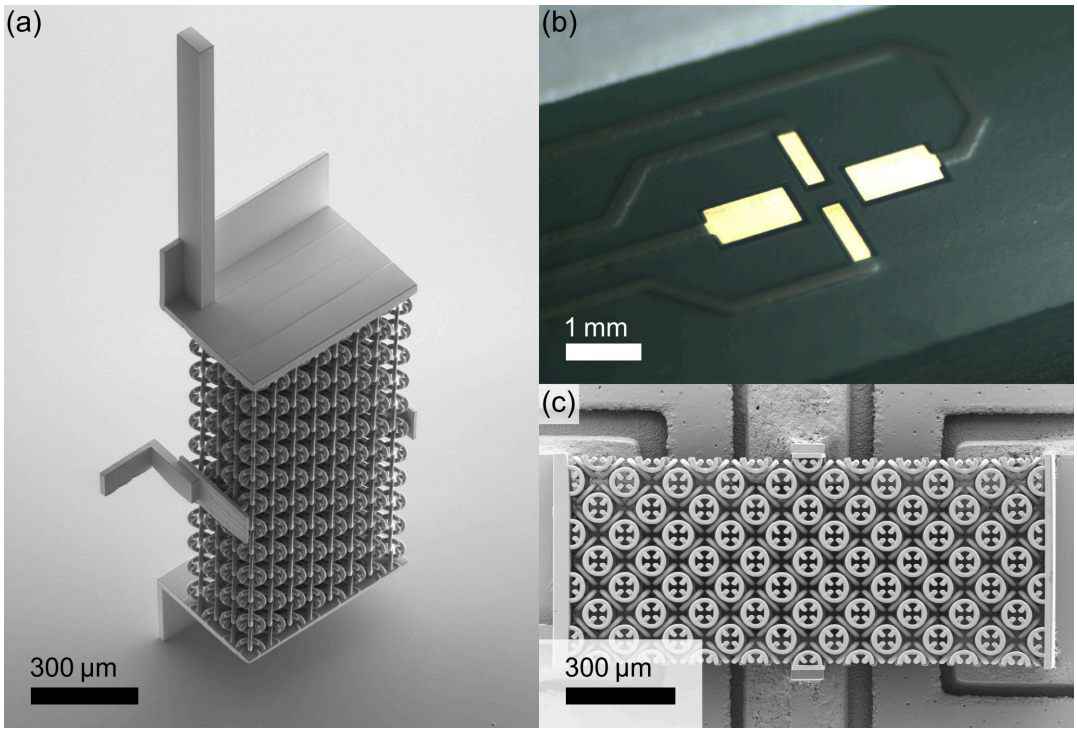

Figure 6.1: Micrographs illustrating different stages of the transfer-based fabrication process. (a) Scanning electron micrograph of a Hall bar on a Si substrate after 3D DLW and ALD prior to its transfer. A specific orientation of the chainmail-inspired unit cell is shown (case D, see Figure 6.3). (b) Light micrograph of the central area of the PCB with the four gold-coated contact pads. (c) Scanning electron micrograph of a completed Hall-bar device, i.e., a Hall bar after transfer and curing of the conductive resin. The orientation of the unit cells, see Figure 6.3, corresponds to case C. Adapted from reference [159].

probe station based experiments, see section 5.1. As a consequence, the sample can be readily removed from the Si substrate later. Nonetheless, unintended detachment during processing is rare. The structures are fabricated from IP-S (Nanoscribe GmbH) with a 25× NA 0.8 objective (LCI Plan-Neofluar Imm Corr DIC M27, Carl Zeiss Microscopy GmbH). The discretization is performed using a slicing distance of 0.5 µm and a hatching distance of 0.2 µm. The design parameters of the chainmail-like metamaterial template are, compare Figure 5.3, lattice constant $a =$

104 µm, major torus radius $R = 36\,\mu m$, minor torus radius $r = 6\,\mu m$, and distance parameter $d = -20\,\mu m$.

2. The sample is developed by immersing it in mr-Dev 600 (based on 1-methoxy-2-propyl acetate/PGMEA, micro resist technology GmbH) for 60 minutes, followed by immersing it in isopropyl alcohol and water for 2 minutes each.

3. Following baking at a temperature of 200 °C and a pressure of about 1.3 mbar for 7 h in the ALD reactor chamber, the sample is conformally coated with a thin layer of Al_2O_3 using ALD. Deposition of 50 cycles is carried out from TMAl and water at a temperature of 150 °C. This film, with a thickness of 5 nm, as determined by ellipsometry measurements of reference layers grown on Si substrates, acts as a base layer for the following deposition of ZnO.

4. The sample is conformally coated with a thin layer of ZnO using ALD. In total, 1000 cycles are deposited from DEZn and water at a temperature of 200 °C. A film thickness of $t = 0.17\,\mu m$ was determined by ellipsometry measurements of reference layers grown on Si substrates.

5. Electrically conductive silver epoxy resin (EC 101, Polytec PT GmbH) is dispensed onto the four contact pads of a prefabricated PCB. Dispensing is performed manually under a stereo microscope. A syringe with a dispense tip with an inner diameter of 150 µm is used.

6. Using a scalpel, the Hall bar is carefully removed from the substrate under a stereo microscope. Subsequently, it is gripped at the handling arm using a pair of fine-tip tweezers and transfered to the PCB where it is carefully positioned.

7. The conductive resin is cured by placing the sample on a hotplate at a temperature of 125 °C for 25 minutes.

8. Following cool-down, a box header connector is soldered onto the PCB.

The parameters for sample processing and ALD given above are slightly different from those used earlier for the fabrication of samples for the probe-station based experiments, compare section 5.1. The original parameters led

to halo-like inhomogeneities of the ZnO layer on the substrate in the vicinity of the Hall bar as well as on the Hall bar itself. While the underlying reasons remain to be unclear, it was possible to largely eliminate these issues by employing the development procedure, baking step, and Al_2O_3 base layer described above [159]. Similar base layers were previously used for the deposition of ZnO on PMMA [127]. Furthermore, acetone was not used in the final development process. Samples immersed in acetone during the development process had shown even more pronounced inhomogeneities [159]. It is known that structures fabricated from IP-S swell in acetone [162], which may cause outgassing during ALD, interfering with the deposition process. Nevertheless, small inhomogeneities have remained.

6.2 Measurement setup

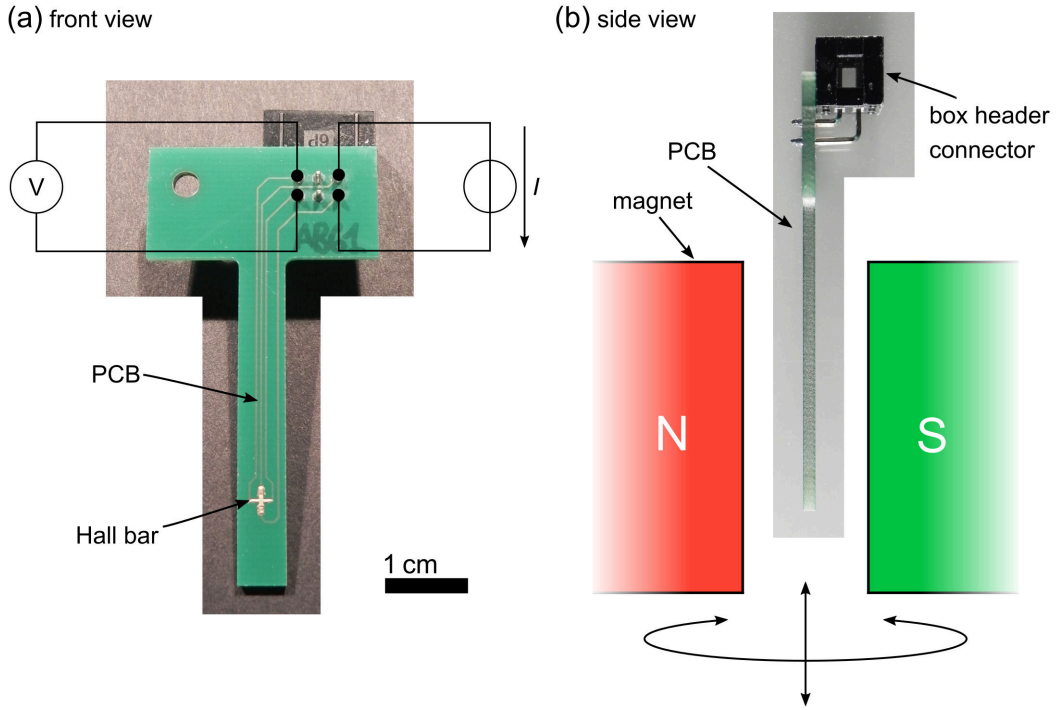

Figure 6.2: Two photographs of a Hall-bar device illustrating the measurement procedure. (a) Front view of the Hall-bar device with schematically indicated measurement electronics for imposing the current flow and measuring the transversal voltage. The electrical connection to the sample is made via a box-header connector on the back of the PCB. (b) Side view showing the Hall-bar device in the gap of the permanent magnet. Using stepper motors, the magnet can be rotated and moved vertically. The lower part of the PCB has a width of 6 mm, which is smaller than the gap size of the magnet (15 mm) and, therefore, allows for a rotation of the magnet without prior movement to a lower position.

Following fabrication of the Hall-bar devices, I have characterized them by performing Hall measurements. A corresponding illustration is shown in Figure 6.2. For convenience, I have used a modified version of the setup described in section 5.2. Most conventional Hall measurement setups would

be suitable as well.

In contrast to the previously used setup, the electrical contact is not made using probe tips but via an electrical connector. As in the previous experiments, I am employing a permanent magnet with a flux density of $\pm 0.83\,\mathrm{T}$ and a gap size of 15 mm. Prior to the measurements, the sample is positioned such that the Hall bar is in the center of the gap. Using stepper motors, the magnet can be rotated and moved vertically. A rotation of 180° is used to invert the magnetic field. In contrast to the probe station based experiments and due to the narrow shape of the PCB, this rotation can be performed without a previous movement of the magnet to a lower position, compare section 5.2. As a consequence, the inversion can be performed much faster, which is beneficial as the signal-to-noise ratio is limited by $1/f$-noise. The vertical movement can be employed for magnetic-field dependent measurements by varying the position of the Hall bar relatively to the magnet. A source-measurement unit (B2901A, Keysight Technologies Inc.) is used to impose a constant current flow and measure the corresponding transversal voltage. A switch system, see section 5.2, facilitates the measurement of I-V-curves for each pair of contacts prior to the actual Hall measurements. A personal computer is used for data acquisition and analysis, and for controlling the source-measurement unit, stepper motors, and switch system.

6.3 Investigating the role of unit cell orientation

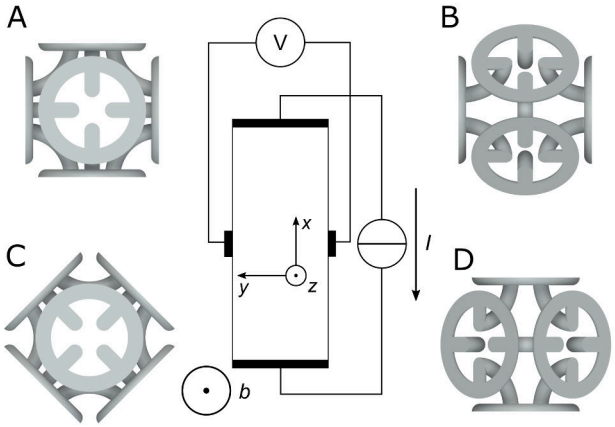

Figure 6.3: Schematic illustration of the four experimentally realized unit-cell orientations of the single-constituent chainmail-like metamaterial with respect to the Hall bar and, neglecting the influence of the contacts, the directions of macroscopic current flow ($\hat{x}$), magnetic field ($\hat{z}$) and macroscopic Hall electric field ($\hat{y}$). Adapted from [159].

In order to demonstrate the usefulness of the new approach, I have used it for further experimental characterization of the single-component chainmail-inspired metamaterial, see sections 3.2 and 5.3, which exhibits a sign-inversion of the effective Hall coefficient. The following summary of the experiments follows one of my previous publications [159].

As discussed in section 3.2, the chainmail-like metamaterials have cubic symmetry, which theoretically guarantees an isotropic effective Hall tensor, i.e., the effective Hall tensor reduces to an effective Hall coefficient, see also [14]. In the limit of infinitely many unit cells, Hall bars with different orientations of the chainmail-inspired unit cell should, therefore, behave identically.

In order to study the effect of unit cell orientation experimentally, I have fabricated metamaterial Hall-bar devices with four out of the infinitely many possible orientations. These four orientations (A-D) are schematically shown

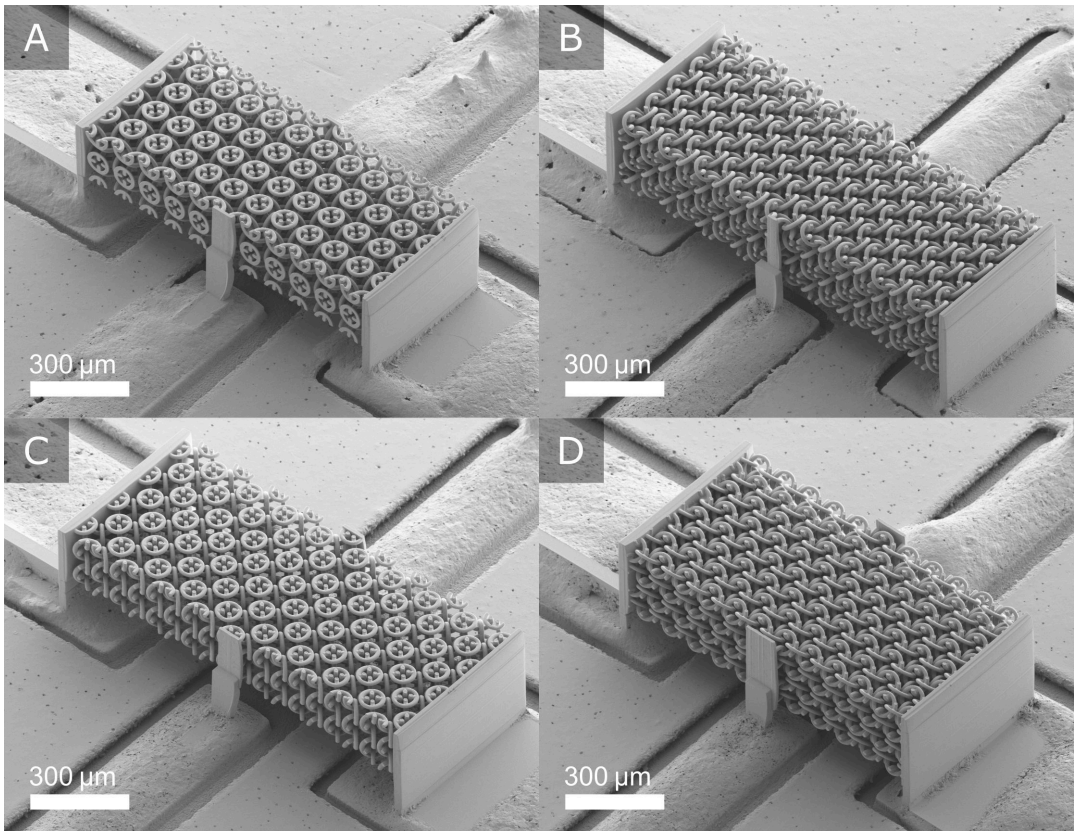

Figure 6.4: Scanning electron micrographs of experimentally realized metamaterial Hall-bar devices corresponding to the four unit cell orientations (A-D) which are shown in Figure 6.3. Design parameters of the chainmail-like metamaterial are, compare Figure 5.3, $a = 104\,\mu\text{m}$, $R = 36\,\mu\text{m}$, $r = 6\,\mu\text{m}$, $d = -20\,\mu\text{m}$. The Hall-bar dimensions for each of the orientations (A-D) are listed in Table 6.1. Adapted from [159].

in Figure 6.3. Scanning electron micrographs of corresponding metamaterial Hall-bar devices are shown in Figure 6.4. In case A, corresponding to the orientation that was chosen for the probe-station based experiments, see section 5.3, the directions of macroscopic current flow, magnetic field and effective Hall electric field are along the principal directions of the cubic unit cell. For the three other orientations (B-D), two of these three quantities are along face diagonals of the cubic unit cell. For each of the four orientations, the outer dimensions of the Hall bar, L_x, L_y, and L_z, which are listed in

	A	B	C	D
L_x/a	11	$9\sqrt{2}$	$9\sqrt{2}$	11
L_y/a	5	5	$4\sqrt{2}$	$4\sqrt{2}$
L_z/a	2	$2\sqrt{2}$	2	$2\sqrt{2}$

Table 6.1: Metamaterial Hall-bar dimensions, L_x, L_y, and L_z, in units of the lattice constant, a, for the four different unit cell orientations (A-D). Adapted from [159].

Table 6.1, and the contact dimensions are slightly different.

Furthermore, the termination of the metamaterial inevitably depends on the unit-cell orientation. As the ALD process coats all surfaces, the outer surfaces of the material are coated as well. As a consequence, I have chosen the termination such that the influence of the conductive coating on the outer surface becomes comparably small. Following fabrication, I have performed Hall measurements for each of the samples and determined the corresponding effective Hall coefficient.

Prior to the actual Hall measurements, the quality of the contacts was assessed by measuring I-V curves for each pair of contacts. The resistance between different contacts, estimated via a linear fit to the data, is about $2\,\mathrm{k}\Omega$. As already discussed, Ohmic contacts are usually desired, but not strictly necessary. For the probe-station based experiments, I have used Ti/Au bilayers to make contact to the ZnO films. Here, the contact is formed via the electrically conducting epoxy resin, which leads to deviations from the ideal Ohmic behavior. For the current-injection contacts and the pick-up contacts, the relative deviations from the linear fits are less than 1% and 17%, respectively [159].

Hall measurements are performed similarly to the probe-station based measurements by imposing a constant current flow, I, and measuring the transversal voltage, U_y, at a magnetic field of $b_z = \pm 0.83\,\mathrm{T}$. During each measurement, the magnetic field is inverted repeatedly by rotating the permanent magnet by 180°, which results in raw data as those shown in Figure 6.5. The Hall voltage, U_H, is inferred from the differences in transversal voltage for the two magnetic field orientations. Such measurements are repeated for

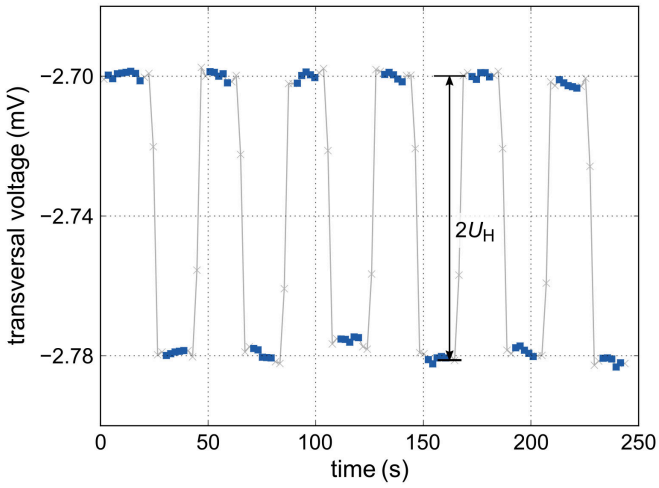

Figure 6.5: Measured transversal voltage versus time for one of the metamaterial Hall-bar devices (unit-cell orientation A, Gen. I) at a current flow of $I = 0.5\,\mathrm{mA}$ and a magnetic field of $|b_z| = 0.83\,\mathrm{T}$. During the measurement, the magnetic field is inverted several times which results in a square-wave like pattern. The Hall voltage is inferred from the height of this pattern, i.e., from the differences in transversal voltage for the two magnetic field orientations. Parameters of the chainmail-like metamaterial are as in Figure 6.4. Adapted from [159].

different values of the electric current, I. The resulting Hall voltage versus current for each of the four different orientations is shown in Figure 6.6. The Hall resistance, R_H, is extracted from a fit assuming a proportional behavior. For each of the structures, the effective Hall coefficient of the metamaterial is then estimated as $A^*_\mathrm{H} = R_\mathrm{H} L_z / b_z$. For the four unit cell orientations (A-D) and two nominally identical generations of samples, the resulting effective Hall coefficients are shown in Table 6.2. The Hall coefficient of the bare films, $A^0_\mathrm{H} = -3.02 \cdot 10^{-7}\,\mathrm{m^3\,A^{-1}\,s^{-1}}$ [159], was determined via van-der-Pauw measurements on square-shaped ($10\,\mathrm{mm} \times 10\,\mathrm{mm}$) glass substrates. Electrical contact was made in the corners of the samples, using the electrically conducting epoxy resin.

As expected, the results consistently show a sign-inversion of the effective Hall coefficient. Furthermore, the values of the effective Hall coefficient for

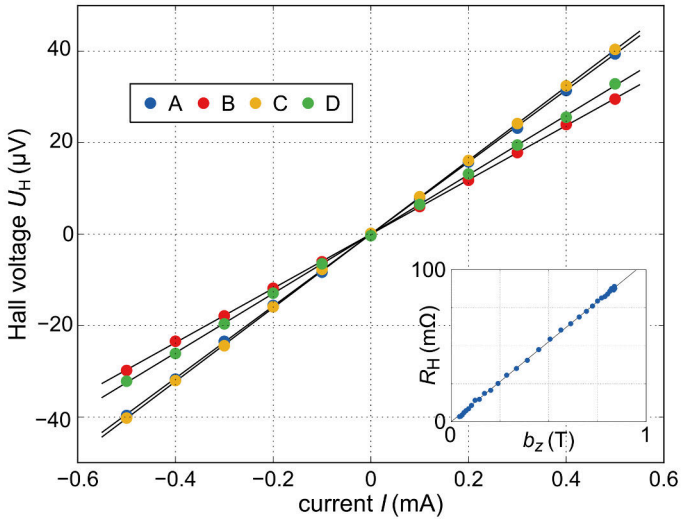

Figure 6.6: Hall voltage as a function of the imposed current flow for four different Hall-bar devices corresponding to the the four different unit cell orientations (A-D, Gen. I), compare Figure 6.3. Each of the dots correspond to a measurement as the one shown in Figure 6.5. The straight black lines correspond to fits assuming a proportional behavior. The Hall resistances of two of the samples (A, C) are larger than those of the other two samples (B, D) due to different sample thicknesses, compare Table 6.1. Parameters are as in Figure 6.4. The inset shows the magnetic-field dependence of the Hall resistance for one of the samples (case A). The corresponding measurement was carried out by varying the position of the magnet with respect to the sample. Adapted from [159].

	A	B	C	D
A_H^*/A_H^0 (Gen. I)	−65	−70	−67	−76
A_H^*/A_H^0 (Gen. II)	−74	−67	−58	−68

Table 6.2: Effective Hall coefficients for the four different unit cells orientations (A-D) and two different nominally identical sample generations (Gen. I/Gen. II). Parameters are as in Figure 6.4. Adapted from [159].

the four different unit cell orientations are very similar, scattering by less than ±13% [159], which is in good agreement with the expected isotropic behavior. The remaining variations are likely due to the finite number of

unit cells, different contact sizes, and different surface terminations. Furthermore, as mentioned in section 5.3, the elongated shape of the voxel leads to slightly ellipsoidal cross sections of the cylinder and tori, which affects each of the four orientations to a different extent. Deviations between nominally identical samples are likely caused by the ALD process. Again, one can compare the experimental results to corresponding numerical calculations. Assuming an infinitely extended medium, i.e., using periodic boundary conditions, these calculations were performed as described in section 3.1. For the design parameters given in Figure 6.4, the calculations yield an effective Hall coefficient of $A_{\mathrm{H}}^{*} = -100 A_{\mathrm{H}}^{0}$ [159], which is somewhat larger than the experimentally determined value. This deviation is at least partially caused by the finite voxel size, which leads to slightly larger values of the radius r, causing the experimentally determined effective Hall coefficient to be smaller.

In summary, the results are consistent with an isotropic effective material behavior and clearly show a sign-inverted effective Hall coefficient. They are in agreement with theory, in which the isotropic behavior follows from the cubic symmetry of the structure, and corresponding numerical calculations.

7 Chapter 7
Conclusions & Outlook

In the scope of this thesis, I have studied the Hall effect in three-dimensional metamaterials for weak magnetic fields. In the following, I will summarize my results and give a brief outlook.

In chapter 2, I have introduced the classical Hall effect. Following a short discussion on how symmetry affects the tensorial material properties of a crystal, I have shown, using Onsager's principle, that the influence of a weak magnetic field on the conductivity of a material can be described by a rank-two tensor, the so-called Hall tensor. Subsequently, I have introduced metamaterials, which are artificial composites with effective properties that go beyond those of their constituent materials and that are determined by a specifically chosen structure. The chapter concludes with an introduction to the concept of Hall metamaterials, which are metamaterials that are used to tailor the effective behavior of conductive materials in weak magnetic fields, i.e., that are used to tailor the effective Hall tensor.

The theoretical aspects of three-dimensional Hall metamaterials were discussed in chapter 3. First, I have given a previously known derivation for the effective Hall tensor that is based on a solution of the conductivity problem for zero magnetic field. Based on this equation and corresponding numerical calculations, I have discussed how one can realize different effective Hall tensors. I have separately discussed isotropic and anisotropic effective Hall tensors.

In the isotropic case, the Hall tensor has only a single independent component, i.e., it reduces to the Hall coefficient. Interestingly, in three dimensions,

the effective Hall coefficient can be sign-inverted with respect to the Hall coefficients of the constituent materials. Following a discussion of the first metamaterial exhibiting such a sign-inversion, which was proposed by Briane and Milton and was inspired by medieval chainmail, I have discussed how the sign-inversion can be obtained in single-constituent porous structures. An intuitive interpretation of the sign-inversion was given and the relation to so-called anti-Hall bars was explained. Subsequently, a hollow version of the material, which is the geometry that corresponds to the experimental realization, was presented. By adjusting two geometry parameters of this structure, one can realize any arbitrary effective Hall coefficient, sign-inverted or not. For every value of the effective Hall coefficient, the corresponding values of the geometry parameters are given by a simple mapping.

Furthermore, I have introduced a second single-constituent porous metamaterial with a sign-inverted effective Hall coefficient that is based on a simple building block that inverts a local Hall voltage. Several such building blocks were combined in order to arrive at a unit cell of an isotropic effective material, which can be seen as a network of Hall voltage sources.

Subsequently, I have considered the general case of anisotropic Hall tensors. First, I have discussed the decomposition of a Hall tensor into a symmetric and an antisymmetric tensor and have given corresponding interpretations. Notably, in a long metamaterial Hall bar, off-diagonal components of the Hall tensor give rise to a Hall electric parallel to the magnetic field, which leads to a corresponding Hall voltage, the so-called parallel Hall voltage. Following a description of the first metamaterial with an antisymmetric effective Hall tensor, which had been proposed by Briane and Milton, I presented a similar single-constituent porous metamaterial. Thereafter, I discussed, how in a related structure with lower symmetry, one can adjust the angle between the macroscopic and the magnetic field. Via two geometry parameters, one can realize any orientation of the macroscopic Hall electric field in the plane perpendicular to the direction of current flow, which is reflected in a corresponding behavior of two Hall voltages, the conventional orthogonal Hall voltage and the parallel Hall voltage. Again, a hollow version corresponding to the experimental realization was presented. A simple model that describes the metamaterial as a network of voltage sources was used to derive an equation for the components of the effective Hall tensor.

Thereafter, I have given a short discussion of bounds on the effective Hall tensor. As shown by Briane and Milton, the effective Hall tensor is bounded by the contrast of conductivities of the constituent materials. In an extension of their work, I have shown that the effective Hall mobility is bounded by twice the largest Hall mobility among its constituent materials.

Furthermore, I have shown how one can treat non-trivial distributions of the magnetic permeability. On the basis of numerical calculations, I have demonstrated that one can use structures made from a highly-permeable material to obtain a sign-inverted effective Hall coefficient. Moreover, I have shown that, using magnetic permeability distributions, effective material properties can be realized that exceed the bound on the effective Hall mobility.

On the experimental side, three-dimensional Hall metamaterials were fabricated on the microscale. The fabrication was performed in several steps. 3D DLW was used to fabricate electrically-insulating polymer templates. ALD was used to coat these polymer templates with thin conformal films of n-type ZnO. EB-PVD was used to deposit thin metal layers that form Ohmic contacts.

An introduction to these methods was given in chapter 4. Following a general discussion of 3D DLW, I have focused on several challenges that occur during the fabrication of structures with feature sizes that are large as compared to the size of a voxel. In the subsequent summary of the fundamentals of ALD, I have described the deposition of ZnO from DEZn and water using a thermal ALD process. Separate sections were dedicated to the the properties of ALD-deposited ZnO films and to the mechanisms underlying the film growth on polymers.

In chapter 5, I have presented my experimental results on three-dimensional Hall metamaterials that were obtained using a magneto-electric probe station. In the first section of the chapter, I have discussed the details of the fabrication process. Subsequently, I have described the measurement setup. Contact to the metamaterial Hall bar samples was made using four tungsten probe tips. Measurements were performed using a source-measurement unit and a permanent magnet. Experimental results for two different metamateri-

als were discussed.

First, I presented experimental results on the chainmail-like isotropic metamaterial exhibiting a sign-inversion of the effective Hall coefficient. By performing measurements on corresponding metamaterial Hall bars, I have been able to demonstrate this sign-inversion experimentally for the first time. Moreover, the experimental results show that the effective Hall coefficient can be tuned continuously by adjusting a geometry parameter.

Second, I presented experimental results on the anisotropic metamaterial that enables control over the orientation of the Hall electric field in the plane perpendicular to the direction of current flow. Two aspects are important. First, the results provide clear evidence for the parallel Hall effect. Second, the control over the orientation of the Hall electric field was demonstrated experimentally by realizing all four sign combinations of the two Hall voltages, the orthogonal and the parallel Hall voltage.

In chapter 6, I have discussed how such metamaterial microstructures can be contacted in a permanent way on printed circuit boards. This fabrication approach significantly simplifies the measurement procedure. Furthermore, it is an important step towards potential applications, for example, towards sensors for the circulation of magnetic fields. Using this approach, I have studied the chainmail-like metamaterial in further detail. By investigating metamaterial Hall bars corresponding to different orientations of the unit cell, I was able to demonstrate experimentally that, in agreement with theory, the microstructure effectively acts like an isotropic material.

There are, however, many open questions. For example, whether any arbitrary effective Hall tensor is realizable using, for example, metamaterials made from a single isotropic constituent material is yet to be answered. Certainly, it would be desirable to have a simple recipe that yields a microstructure for a given effective Hall tensor. Furthermore, it would be interesting to extend the analysis to stronger magnetic fields. Corresponding previous results by Bergman and coworkers, who found a very strong anisotropic magnetoresistance for arrays of cylindrical or spherical inclusions, suggest that there is plenty to explore.

Bibliography

[1] E. H. Hall, "On a New Action of the Magnet on Electric Currents", Am. J. Math. **2**, 287–292 (1879) (Cited on pages 3, 19).

[2] J. C. Maxwell, *A Treatise on Electricity and Magnetism*, Vol. 2 (Clarendon Press, Oxford, 1873) (Cited on page 3).

[3] E. H. Hall, "On the New Action of Magnetism on a Permanent Electric Current", Am. J. Sci. **20**, 161–186 (1880) (Cited on page 3).

[4] P. Ripka, *Magnetic Sensors and Magnetometers* (Artech House, Boston, London, 2001) (Cited on pages 3, 83).

[5] K. Reif, *Sensoren im Kraftfahrzeug* (Springer Vieweg, Wiesbaden, 2010) (Cited on page 4).

[6] S. G. Corrion, S. B. Gentry, and B. K. Blackburn, *Seat belt buckle with Hall effect locking indicator and method of use*, US5742986A, 1997 (Cited on page 4).

[7] G. W. Milton, *The Theory of Composites* (Cambridge University Press, Cambridge, 2002) (Cited on pages 8, 32–35, 37, 42–44).

[8] M. Cardona and P. Yu, *Fundamentals of Semiconductors* (Springer-Verlag, Berlin, Heidelberg, 2005) (Cited on pages 10, 13, 20).

[9] R. S. Popovic, *Hall Effect Devices* (IOP Publishing, Bristol, 2004) (Cited on pages 12–16, 20, 83).

[10] L. J. van der Pauw, "A method of measuring specific resistivity and Hall effect of discs of arbitrary shape", Philips Res. Rep. **13**, 1–9 (1958) (Cited on page 14).

[11] *ASTM Standard F76-08, Standard Test Methods for Measuring Resistivity and Hall Coefficient and Determining Hall Mobility in Single-Crystal Semiconductors* (ASTM International, West Conshohocken, 2008) (Cited on pages 14, 16).

[12] H.-J. Lippmann and F. Kuhrt, "Der Geometrieeinfluss auf den Halleffekt bei rechteckigen Halbleiterplatten", Z. Naturforsch. A **13**, 474–483 (1958) (Cited on page 14).

[13] J. Haeusler, "Die Geometriefunktion vierelektrodiger Hallgeneratoren", Electr. Eng. **52**, 11–19 (1968) (Cited on page 14).

[14] C. Kern, G. W. Milton, M. Kadic, and M. Wegener, "Theory of the Hall effect in three-dimensional metamaterials", New J. Phys. **20**, 083034 (2018) (Cited on pages 17, 29, 31, 42, 45, 46, 50–61, 65–69, 71, 75, 77–85, 135).

[15] R. G. Mani and K. von Klitzing, "Hall effect under null current conditions", Appl. Phys. Lett. **64**, 1262–1264 (1994) (Cited on pages 17, 18, 56).

[16] A. Gibson, M. Kimmitt, and A. Walker, "Photon drag in germanium", Appl. Phys. Lett. **17**, 75–77 (1970) (Cited on page 19).

[17] A. F. Gibson and M. F. Kimmitt, "Photon Drag Detection", in Infrared and Millimeter Waves, Vol. 3, edited by K. J. Button (1980), pp. 181–217 (Cited on pages 19, 20).

[18] M. Wegener, *Extreme Nonlinear Optics: An Introduction* (Springer-Verlag, Berlin, Heidelberg, 2005) (Cited on page 19).

[19] H. M. Barlow, "The Hall Effect and its Application to Microwave Power Measurement", Proc. IRE **46**, 1411–1413 (1958) (Cited on page 19).

[20] T. C. Harman and J. M. Honig, *Thermoelectric and Thermomagnetic Effects and Applications* (McGraw-Hill, New York, 1967) (Cited on page 20).

[21] H. J. Goldsmid, *Introduction to Thermoelectricity* (Springer-Verlag, Berlin, Heidelberg, 2010) (Cited on page 20).

[22] A. v. Ettingshausen and W. Nernst, "Ueber das Auftreten electromotorischer Kräfte in Metallplatten, welche von einem Wärmestrome durchflossen werden und sich im magnetischen Felde befinden", Ann. Phys. (Leipzig) **265**, 343–347 (1886) (Cited on page 20).

[23] K. v. Klitzing, G. Dorda, and M. Pepper, "New Method for High-Accuracy Determination of the Fine-Structure Constant Based on Quantized Hall Resistance", Phys. Rev. Lett. **45**, 494 (1980) (Cited on page 20).

[24] H. Ibach and H. Lüth, *Festkörperphysik: Einführung in die Grundlagen* (Springer-Verlag, Berlin, Heidelberg, 2009) (Cited on page 21).

[25] *SI Brochure: The International System of Units (SI) [8th edition, 2006; updated in 2014]* (Bureau International des Poids et Mesures, Sèvres, 2014) (Cited on page 21).

[26] D. C. Tsui, H. L. Störmer, and A. C. Gossard, "Two-Dimensional Magnetotransport in the Extreme Quantum Limit", Phys. Rev. Lett. **48**, 1559 (1982) (Cited on page 21).

[27] J. F. Nye, *Physical Properties of Crystals: Their Representation by Tensors and Matrices* (Clarendon Press, Oxford, 1985) (Cited on pages 22–24, 26–28, 63).

[28] C. Bradley and A. Cracknell, *The Mathematical Theory of Symmetry in Solids: Representation Theory for Point Groups and Space Groups* (Clarendon Press, Oxford, 1972) (Cited on pages 25, 26).

[29] G. F. Koster, *Space Groups and Their Representations* (Academic Press, New York, 1957) (Cited on pages 25, 26).

[30] N. W. Ashcroft and N. D. Mermin, *Solid State Physics* (Rinehart and Winston, New York, 1976) (Cited on page 25).

[31] T. Hahn, ed., *International Tables for Crystallography, Volume A: Space-group symmetry* (International Union of Crystallography, 2006) (Cited on pages 25, 26).

[32] F. Seitz, "On the Reduction of Space Groups", Ann. Math., 17–28 (1936) (Cited on page 25).

[33] A. Authier, ed., *International Tables for Crystallography, Volume D: Physical properties of crystals* (International Union of Crystallography, 2006) (Cited on pages 27, 28).

[34] L. Onsager, "Reciprocal Relations in Irreversible Processes. I.", Phys. Rev. **37**, 405 (1931) (Cited on page 29).

[35] L. D. Landau and E. M. Lifshitz, *Statistical Physics, Part 1*, §120 (Pergamon Press, Oxford, 1980) (Cited on page 29).

[36] L. D. Landau and E. M. Lifshitz, *Electrodynamics of Continuous Media*, §22 (Pergamon Press, Oxford, 1984) (Cited on pages 29, 31).

[37] M. Briane and G. W. Milton, "An Antisymmetric Effective Hall Matrix", SIAM J. Appl. Math. **70**, 1810–1820 (2010) (Cited on pages 29, 31, 37, 42, 44, 64, 65).

[38] S. A. Tretyakov, "A personal view on the origins and developments of the metamaterial concept", J. Opt. **19**, 013002 (2017) (Cited on page 32).

[39] G. W. Milton, "Analytic materials", Proc. Royal Soc. A **472** (2016) (Cited on pages 32, 34).

[40] J. Brown, "Artificial dielectrics having refractive indices less than unity", Proc. IEE - Part IV **100**, 51–62 (1953) (Cited on page 32).

[41] R. Lakes, "Cellular solid structures with unbounded thermal expansion", J. Mater. Sci. Lett. **15**, 475–477 (1996) (Cited on page 33).

[42] R. Gatt and J. N. Grima, "Negative compressibility", Phys. Status Solidi RRL **2**, 236–238 (2008) (Cited on page 33).

[43] J. Qu, M. Kadic, A. Naber, and M. Wegener, "Micro-Structured Two-Component 3D Metamaterials with Negative Thermal-Expansion Coefficient from Positive Constituents", Sci. Rep. **7**, 40643 (2017) (Cited on page 33).

[44] J. Qu, M. Kadic, and M. Wegener, "Poroelastic metamaterials with negative effective static compressibility", Appl. Phys. Lett. **110**, 171901 (2017) (Cited on page 33).

[45] J. Qu, A. Gerber, F. Mayer, M. Kadic, and M. Wegener, "Experiments on Metamaterials with Negative Effective Static Compressibility", Phys. Rev. X **7**, 041060 (2017) (Cited on page 33).

[46] A. N. Lagarkov, V. N. Semenenko, V. A. Chistyaev, D. E. Ryabov, S. A. Tretyakov, and C. R. Simovski, "Resonance Properties of Bi-Helix Media at Microwaves", Electromagnetics **17**, 213–237 (1997) (Cited on page 33).

[47] J. B. Pendry, A. J. Holden, D. J. Robbins, and W. J. Stewart, "Magnetism from conductors and enhanced nonlinear phenomena", IEEE Trans. Microw. Theory Tech. **47**, 2075–2084 (1999) (Cited on page 33).

[48] J. Mei, Z. Liu, W. Wen, and P. Sheng, "Effective Mass Density of Fluid-Solid Composites", Phys. Rev. Lett. **96**, 024301 (2006) (Cited on page 33).

[49] G. Batchelor, "Transport Properties of Two-Phase Materials with Random Structure", Annu. Rev. Fluid Mech. **6**, 227–255 (1974) (Cited on page 34).

[50] M. Kadic, T. Bückmann, R. Schittny, and M. Wegener, "Experiments on cloaking in optics, thermodynamics and mechanics", Philos. Trans. Royal Soc. A **373**, 20140357 (2015) (Cited on page 34).

[51] S. Mannherz, A. Niemeyer, F. Mayer, C. Kern, and M. Wegener, "On the limits of laminates in diffusive optics", Opt. Express **26**, 34274–34287 (2018) (Cited on page 35).

[52] R. Schittny, "Cloaking in Heat Conduction and Light Diffusion", PhD thesis (Institute of Applied Physics, Karlsruhe Institute of Technology, 2015) (Cited on page 35).

[53] D. J. Bergman and O. Levy, "Thermoelectric properties of a composite medium", J. Appl. Phys. **70**, 6821–6833 (1991) (Cited on page 35).

[54] W. Shockley and H. J. Queisser, "Detailed Balance Limit of Efficiency of *p-n* Junction Solar Cells", J. Appl. Phys. **32**, 510–519 (1961) (Cited on page 36).

[55] M. Briane and G. W. Milton, "Homogenization of the Three-dimensional Hall Effect and Change of Sign of the Hall Coefficient", Arch. Rational Mech. Anal. **193**, 715–736 (2009) (Cited on pages 37, 42, 49, 51, 52).

[56] Y. Grabovsky, *Composite Materials; Mathematical theory and exact relations* (IOP Publishing, Bristol, 2016) (Cited on page 37).

[57] H. J. Juretschke, R. Landauer, and J. Swanson, "Hall Effect and Conductivity in Porous Media", J. Appl. Phys. **27**, 838–839 (1956) (Cited on page 37).

[58] B. I. Shklovskii, "Critical behavior of the Hall coefficient near the percolation threshold", Sov. Phys. JETP **45**, 152 (1977) (Cited on page 38).

[59] J. Straley, "Conductivity anisotropy and the Hall effect in inhomogeneous conductors near the percolation threshold", J. Phys. C. **13**, 4335 (1980) (Cited on page 38).

[60] D. J. Bergman, Y. Kantor, D. Stroud, and I. Webman, "Critical Behavior of the Low-Field Hall Conductivity at a Percolation Threshold", Phys. Rev. Lett. **50**, 1512 (1983) (Cited on page 38).

[61] M. Briane and G. W. Milton, "Giant Hall Effect in Composites", Multiscale Model. Simul. **7**, 1405–1427 (2009) (Cited on pages 38, 75).

[62] M. Briane, D. Manceau, and G. Milton, "Homogenization of the two-dimensional Hall effect", J. Math. Anal. Appl. **339**, 1468–1484 (2008) (Cited on pages 38, 48).

[63] M. Rohde and H. Micklitz, "Critical behavior of the Hall conductivity near the percolation threshold in granular Sn:Ar mixtures", Phys. Rev. B **36**, 7289 (1987) (Cited on page 38).

[64] U. Dai, A. Palevski, and G. Deutscher, "Hall effect in a three-dimensional percolation system", Phys. Rev. B **36**, 790–792 (1987) (Cited on page 38).

[65] D. J. Bergman and Y. M. Strelniker, "Calculation of strong-field magnetoresistance in some periodic composites", Phys. Rev. B **49**, 16256 (1994) (Cited on page 38).

[66] Y. M. Strelniker and D. J. Bergman, "Theory of magnetotransport in a composite medium with periodic microstructure for arbitrary magnetic fields", Phys. Rev. B **50**, 14001 (1994) (Cited on page 38).

[67] M. Tornow, D. Weiss, K. v. Klitzing, K. Eberl, D. J. Bergman, and Y. M. Strelniker, "Anisotropic Magnetoresistance of a Classical Antidot Array", Phys. Rev. Lett. **77**, 147 (1996) (Cited on page 38).

[68] F. Murat and L. Tartar, "H-Convergence", in *Topics in the Mathematical Modelling of Composite Materials*, edited by A. Cherkaev and R. Kohn (Birkhäuser, Boston, 2018), pp. 21–43 (Cited on page 42).

[69] D. J. Bergman, "Self-duality and the low field Hall effect in 2D and 3D metal-insulator composites", in *Percolation Structures and Processes*, edited by G. Deutscher, R. Zallen, and J. Adler (Israel Physical Society, Jerusalem, 1983), pp. 297–321 (Cited on pages 43, 44).

[70] T. J. R. Hughes, *The Finite Element Method: Linear Static and Dynamic Finite Element Analysis* (Prentice-Hall, Englewood Cliffs, 1987) (Cited on page 45).

[71] M. Kadic, R. Schittny, T. Bückmann, C. Kern, and M. Wegener, "Hall-Effect Sign Inversion in a Realizable 3D Metamaterial", Phys. Rev. X **5**, 021030 (2015) (Cited on pages 45, 52, 53, 56).

[72] C. Kern, M. Kadic, and M. Wegener, "Parallel Hall effect from three-dimensional single-component metamaterials", Appl. Phys. Lett. **107**, 132103 (2015) (Cited on pages 45, 62, 68, 122).

[73] C. Kern, M. Kadic, and M. Wegener, "Experimental Evidence for Sign Reversal of the Hall Coefficient in Three-Dimensional Metamaterials", Phys. Rev. Lett. **118**, 016601 (2017) (Cited on pages 45, 55, 110, 116–121).

[74] G. Alessandrini and V. Nesi, "Univalent σ-Harmonic Mappings", Arch. Rational Mech. Anal. **158**, 155–171 (2001) (Cited on page 48).

[75] M. Briane, G. W. Milton, and V. Nesi, "Change of Sign of the Corrector's Determinant for Homogenization in Three-Dimensional Conductivity", Arch. Rational Mech. Anal. **173**, 133–150 (2004) (Cited on pages 48–50).

[76] R. Wilson, *Four Colors Suffice: How the Map Problem Was Solved* (Princeton University Press, Princeton, 2003) (Cited on page 49).

[77] M. Briane, M. Kadic, C. Kern, G. Milton, M. Wegener, and D. Whyte, "Surprises Regarding the Hall Effect: An Extraordinary Story Involving an Artist, Mathematicians, and Physicists", SIAM News **50**, 1 (2017) (Cited on pages 49, 50).

[78] R. G. Mani, "Hall sign reversal in certain metamaterials", Physics Today **70**, 13 (2017) (Cited on page 56).

[79] J. Oswald, "Comment on 'Experimental Evidence for Sign Reversal of the Hall Coefficient in Three-Dimensional Metamaterials'", Phys. Rev. Lett. **120**, 149701 (2018) (Cited on page 56).

[80] M. Wegener, M. Kadic, and C. Kern, "Hall-effect metamaterials and 'anti-Hall bars'", Phys. Today **70**, 14 (2017) (Cited on page 56).

[81] C. Kern, M. Kadic, and M. Wegener, "Kern, Kadic, and Wegener Reply", Phys. Rev. Lett. **120**, 149702 (2018) (Cited on page 56).

[82] C. Kern, V. Schuster, M. Kadic, and M. Wegener, "Experiments on the Parallel Hall Effect in Three-Dimensional Metamaterials", Phys. Rev. Applied **7**, 044001 (2017) (Cited on pages 68, 70, 72, 73, 110, 122, 124, 125).

[83] C. Navau, J. Prat-Camps, O. Romero-Isart, J. I. Cirac, and A. Sanchez, "Long-Distance Transfer and Routing of Static Magnetic Fields", Phys. Rev. Lett. **112**, 253901 (2014) (Cited on page 77).

[84] C. N. LaFratta, J. T. Fourkas, T. Baldacchini, and R. A. Farrer, "Multiphoton Fabrication", Angew. Chem. Int. Ed. **46**, 6238–6258 (2007) (Cited on page 88).

[85] T. Baldacchini, ed., *Three-Dimensional Microfabrication Using Two-Photon Polymerization: Fundamentals, Technology, and Applications* (William Andrew, Norwich, 2015) (Cited on page 88).

[86] S. Maruo, O. Nakamura, and S. Kawata, "Three-dimensional microfabrication with two-photon-absorbed photopolymerization", Opt. Lett. **22**, 132–134 (1997) (Cited on page 88).

[87] W. Denk, J. H. Strickler, and W. W. Webb, "Two-photon laser scanning fluorescence microscopy", Science **248**, 73–76 (1990) (Cited on page 88).

[88] G. v. Freymann, A. Ledermann, M. Thiel, I. Staude, S. Essig, K. Busch, and M. Wegener, "Three-Dimensional Nanostructures for Photonics", Adv. Funct. Mater. **20**, 1038–1052 (2010) (Cited on page 88).

[89] T. Gissibl, S. Thiele, A. Herkommer, and H. Giessen, "Two-photon direct laser writing of ultracompact multi-lens objectives", Nat. Photonics **10**, 554 (2016) (Cited on page 88).

[90] A. Ovsianikov, S. Schlie, A. Ngezahayo, A. Haverich, and B. N. Chichkov, "Two-photon polymerization technique for microfabrication of CAD-designed 3D scaffolds from commercially available photosensitive materials", J. Tissue Eng. Regen. Med. **1**, 443–449 (2007) (Cited on page 88).

[91] F. Klein, T. Striebel, J. Fischer, Z. Jiang, C. M. Franz, G. von Freymann, M. Wegener, and M. Bastmeyer, "Elastic Fully Three-dimensional Microstructure Scaffolds for Cell Force Measurements", Adv. Mater. **22**, 868–871 (2010) (Cited on page 88).

[92] T. Bückmann, N. Stenger, M. Kadic, J. Kaschke, A. Frölich, T. Kennerknecht, C. Eberl, M. Thiel, and M. Wegener, "Tailored 3D Mechanical Metamaterials Made by Dip-in Direct-Laser-Writing Optical Lithography", Adv. Mater. **24**, 2710–2714 (2012) (Cited on pages 88, 91).

[93] H. Ito, "Chemical amplification resists: Inception, implementation in device manufacture, and new developments", J. Polym. Sci. A **41**, 3863–3870 (2003) (Cited on page 89).

[94] M. Deubel, G. Von Freymann, M. Wegener, S. Pereira, K. Busch, and C. M. Soukoulis, "Direct laser writing of three-dimensional photonic-crystal templates for telecommunications", Nat. Mater. **3**, 444 (2004) (Cited on page 89).

[95] M. Göppert-Mayer, "Über Elementarakte mit zwei Quantensprüngen", Ann. Phys. (Leipzig) **401**, 273–294 (1931) (Cited on page 89).

[96] M. Thiel, J. Fischer, G. Von Freymann, and M. Wegener, "Direct laser writing of three-dimensional submicron structures using a continuous-wave laser at 532 nm", Appl. Phys. Lett. **97**, 221102 (2010) (Cited on page 89).

[97] J. Fischer, "Three-dimensional optical lithography beyond the diffraction limit", PhD thesis (Institute of Applied Physics, Karlsruhe Institute of Technology, 2012) (Cited on pages 89, 90).

[98] A. Wickberg, A. Abass, H.-H. Hsiao, C. Rockstuhl, and M. Wegener, "Second-Harmonic Generation by 3D Laminate Metacrystals", unpublished, 2019 (Cited on page 90).

[99] S. W. Hell and J. Wichmann, "Breaking the diffraction resolution limit by stimulated emission: stimulated-emission-depletion fluorescence microscopy", Opt. Lett. **19**, 780–782 (1994) (Cited on page 90).

[100] M. Thiel, M. Decker, M. Deubel, M. Wegener, S. Linden, and G. von Freymann, "Polarization Stop Bands in Chiral Polymeric Three-Dimensional Photonic Crystals", Adv. Mater. **19**, 207–210 (2007) (Cited on page 90).

[101] J. Qu, "Doppelinversionsprozess zur Herstellung dreidimensionaler optischer Metamaterialien", Master's Thesis (Institute of Applied Physics, Karlsruhe Institute of Technology, 2015) (Cited on page 91).

[102] A. Münchinger, "3D Cubic Buckling Mechanical Metamaterials", Master's Thesis (Institute of Applied Physics, Karlsruhe Institute of Technology, 2017) (Cited on page 93).

[103] E. H. Waller and G. von Freymann, "Spatio-Temporal Proximity Characteristics in 3D μ-Printing via Multi-Photon Absorption", Polymers **8**, 297 (2016) (Cited on page 93).

[104] M. M. Zieger, P. Müller, E. Blasco, C. Petit, V. Hahn, L. Michalek, H. Mutlu, M. Wegener, and C. Barner-Kowollik, "A Subtractive Photoresist Platform for Micro- and Macroscopic 3D Printed Structures", Adv. Funct. Mater., 1801405 (2018) (Cited on pages 94, 95).

[105] S. Jayanthi, M. Keefe, and E. P. Gargiulo, "Studies in Stereolithography: Influence of Process Parameters on Curl Distortion in Photopolymer Models", in 1994 International Solid Freeform Fabrication Symposium (University of Texas, Austin, 1994), pp. 250–258 (Cited on page 95).

[106] T.-M. Wang, J.-T. Xi, and Y. Jin, "A model research for prototype warp deformation in the FDM process", Int. J. Adv. Manuf. Technol. **33**, 1087–1096 (2007) (Cited on page 95).

[107] R. L. Puurunen, "A Short History of Atomic Layer Deposition: Tuomo Suntola's Atomic Layer Epitaxy", Chem. Vap. Deposition **20**, 332–344 (2014) (Cited on page 96).

[108] N. Pinna and M. Knez, eds., *Atomic Layer Deposition of Nanostructured Materials* (Wiley-VCH Verlag, Weinheim, 2012) (Cited on pages 96, 97).

[109] C. S. Hwang, ed., *Atomic Layer Deposition for Semiconductors* (Springer, New York, 2014) (Cited on page 96).

[110] O. Sneh, R. B. Clark-Phelps, A. R. Londergan, J. Winkler, and T. E. Seidel, "Thin film atomic layer deposition equipment for semiconductor processing", Thin Solid Films **402**, 248–261 (2002) (Cited on page 96).

[111] R. Doering and Y. Nishi, eds., *Handbook of Semiconductor Manufacturing Technology* (CRC Press, Boca Raton, 2007) (Cited on page 96).

[112] H. Kim, H.-B.-R. Lee, and W.-J. Maeng, "Applications of atomic layer deposition to nanofabrication and emerging nanodevices", Thin Solid Films **517**, 2563–2580 (2009) (Cited on page 96).

[113] S. M. George, "Atomic Layer Deposition: An Overview", Chem. Rev. **110**, 111–131 (2009) (Cited on pages 96, 97, 99, 101).

[114] J. W. Elam, N. P. Dasgupta, and F. B. Prinz, "ALD for clean energy conversion, utilization, and storage", MRS Bull. **36**, 899–906 (2011) (Cited on page 96).

[115] R. W. Johnson, A. Hultqvist, and S. F. Bent, "A brief review of atomic layer deposition: from fundamentals to applications", Mater. Today **17**, 236–246 (2014) (Cited on page 96).

[116] P. F. Carcia, R. McLean, M. Reilly, M. Groner, and S. George, "Ca test of Al_2O_3 gas diffusion barriers grown by atomic layer deposition on polymers", Appl. Phys. Lett. **89**, 031915 (2006) (Cited on page 96).

[117] H. C. Guo, E. Ye, Z. Li, M.-Y. Han, and X. J. Loh, "Recent progress of atomic layer deposition on polymeric materials", Mater. Sci. Eng. C. **70**, 1182–1191 (2017) (Cited on pages 96, 104, 105).

[118] D. Jang, L. R. Meza, F. Greer, and J. R. Greer, "Fabrication and deformation of three-dimensional hollow ceramic nanostructures", Nat. Mater. **12**, 893 (2013) (Cited on page 96).

[119] A. Frölich, J. Fischer, T. Zebrowski, K. Busch, and M. Wegener, "Titania Woodpiles with Complete Three-Dimensional Photonic Bandgaps in the Visible", Adv. Mater. **25**, 3588–3592 (2013) (Cited on page 96).

[120] A. Frölich, "On tailored three-dimensional optical materials by atomic layer deposition", PhD thesis (Institute of Applied Physics, Karlsruhe Institute of Technology, 2013) (Cited on pages 98, 99).

[121] J. Fischer, "Verstärkte Erzeugung der zweiten Harmonischen in einem nichtlinearen ABC-Nanolaminat", Master's Thesis (Institute of Applied Physics, Karlsruhe Institute of Technology, 2013) (Cited on page 98).

[122] T. Tynell and M. Karppinen, "Atomic layer deposition of ZnO: a review", Semicond. Sci. Technol. **29**, 043001 (2014) (Cited on pages 97, 99–102).

[123] R. L. Puurunen, "Surface chemistry of atomic layer deposition: A case study for the trimethylaluminum/water process", J. Appl. Phys. **97**, 9 (2005) (Cited on pages 97, 100, 101).

[124] J. Meier, "Entwicklung eines Verfahrens zur On-Chip-Kontaktierung von leitfähigen dreidimensionalen Metamaterialien", Bachelor's Thesis (Institute of Applied Physics, Karlsruhe Institute of Technology, 2016) (Cited on pages 99, 129).

[125] E. B. Yousfi, J. Fouache, and D. Lincot, "Study of atomic layer epitaxy of zinc oxide by in-situ quartz crystal microgravimetry", Appl. Surf. Sci. **153**, 223–234 (2000) (Cited on page 99).

[126] E. Guziewicz, M. Godlewski, L. Wachnicki, T. Krajewski, G. Luka, S. Gieraltowska, R. Jakiela, A. Stonert, W. Lisowski, M. Krawczyk, et al., "ALD grown zinc oxide with controllable electrical properties", Semicond. Sci. Technol. **27**, 074011 (2012) (Cited on pages 100, 102, 103).

[127] M. Napari, J. Malm, R. Lehto, J. Julin, K. Arstila, T. Sajavaara, and M. Lahtinen, "Nucleation and growth of ZnO on PMMA by low-temperature atomic layer deposition", J. Vac. Sci. Technol. A **33**, 01A128 (2015) (Cited on pages 100, 106, 132).

[128] H. Morkoç and Ü. Özgür, *Zinc Oxide: Fundamentals, Materials and Device Technology* (Wiley-VCH Verlag, Weinheim, 2008) (Cited on pages 101, 102).

[129] A. Janotti and C. G. Van de Walle, "Fundamentals of zinc oxide as a semiconductor", Rep. Prog. Phys. **72**, 126501 (2009) (Cited on page 101).

[130] D. Reynolds, D. C. Look, B. Jogai, C. Litton, G. Cantwell, and W. Harsch, "Valence-band ordering in ZnO", Phys. Rev. B **60**, 2340 (1999) (Cited on page 101).

[131] C. Klingshirn, R. Hauschild, H. Priller, J. Zeller, M. Decker, and H. Kalt, "ZnO rediscovered–once again!?", in *Advances in Spectroscopy for Lasers and Sensing*, edited by B. Di Bartolo and O. Forte (Springer, Dordrecht, 2006), pp. 277–293 (Cited on pages 101, 102).

[132] S.-Y. Pung, K.-L. Choy, X. Hou, and C. Shan, "Preferential growth of ZnO thin films by the atomic layer deposition technique", Nanotechnology **19**, 435609 (2008) (Cited on page 101).

[133] H. Mohseni and T. Scharf, "Atomic layer deposition of $ZnO/Al_2O_3/ZrO_2$ nanolaminates for improved thermal and wear resistance in carbon-carbon composites", J. Vac. Sci. Technol. A **30**, 01A149 (2012) (Cited on page 101).

[134] A. Wickberg, C. Kieninger, C. Sürgers, S. Schlabach, X. Mu, C. Koos, and M. Wegener, "Second-Harmonic Generation from ZnO/Al_2O_3 Nanolaminate Optical Metamaterials Grown by Atomic-Layer Deposition", Adv. Opt. Mater. **4**, 1203–1208 (2016) (Cited on page 101).

[135] C. G. Van de Walle, "Hydrogen as a Cause of Doping in Zinc Oxide", Phys. Rev. Lett. **85**, 1012 (2000) (Cited on page 101).

[136] C. G. Van de Walle, "Defect analysis and engineering in ZnO", Physica B **308**, 899–903 (2001) (Cited on page 101).

[137] A. Frölich and M. Wegener, "Spectroscopic characterization of highly doped ZnO films grown by atomic-layer deposition for three-dimensional infrared metamaterials", Opt. Mater. Express **1**, 883–889 (2011) (Cited on page 102).

[138] J. Ramanujam and U. P. Singh, "Copper indium gallium selenide based solar cells – a review", Energy Environ. Sci. **10**, 1306–1319 (2017) (Cited on page 102).

[139] P. Jackson, D. Hariskos, E. Lotter, S. Paetel, R. Wuerz, R. Menner, W. Wischmann, and M. Powalla, "New world record efficiency for Cu(In,Ga)Se_2 thin-film solar cells beyond 20%", Prog. Photovolt. Res. Appl **19**, 894–897 (2011) (Cited on page 102).

[140] J. C. Fan, K. Sreekanth, Z. Xie, S. Chang, and K. V. Rao, "p-Type ZnO materials: Theory, growth, properties and devices", Prog. Mater. Sci. **58**, 874–985 (2013) (Cited on page 102).

[141] D. C. Look, D. C. Reynolds, J. Sizelove, R. Jones, C. W. Litton, G. Cantwell, and W. Harsch, "Electrical properties of bulk ZnO", Solid State Commun. **105**, 399–401 (1998) (Cited on page 102).

[142] K. Ellmer, A. Klein, and B. Rech, eds., *Transparent Conductive Zinc Oxide: Basics and Applications in Thin Film Solar Cells* (Springer-Verlag, Berlin, Heidelberg, 2008) (Cited on page 102).

[143] N. Huby, G. Tallarida, M. Kutrzeba, S. Ferrari, E. Guziewicz, M. Godlewski, et al., "New selector based on zinc oxide grown by low temperature atomic layer deposition for vertically stacked non-volatile memory devices", Microelectron. Eng. **85**, 2442–2444 (2008) (Cited on pages 103, 107).

[144] G. Luka, T. Krajewski, L. Wachnicki, B. Witkowski, E. Lusakowska, W. Paszkowicz, E. Guziewicz, and M. Godlewski, "Transparent and conductive undoped zinc oxide thin films grown by atomic layer deposition", Phys. Status Solidi A **207**, 1568–1571 (2010) (Cited on page 103).

[145] C. Wilson, R. Grubbs, and S. George, "Nucleation and Growth during Al_2O_3 Atomic Layer Deposition on Polymers", Chem. Mater. **17**, 5625–5634 (2005) (Cited on page 104).

[146] J. C. Spagnola, B. Gong, S. A. Arvidson, J. S. Jur, S. A. Khan, and G. N. Parsons, "Surface and sub-surface reactions during low temperature aluminium oxide atomic layer deposition on fiber-forming polymers", J. Mater. Chem. **20**, 4213–4222 (2010) (Cited on page 104).

[147] G. N. Parsons, S. E. Atanasov, E. C. Dandley, C. K. Devine, B. Gong, J. S. Jur, K. Lee, C. J. Oldham, Q. Peng, J. C. Spagnola, et al., "Mechanisms and reactions during atomic layer deposition on polymers", Coord. Chem. Rev. **257**, 3323–3331 (2013) (Cited on pages 104, 105).

[148] A. Mackus, A. Bol, and W. Kessels, "The use of atomic layer deposition in advanced nanopatterning", Nanoscale **6**, 10941–10960 (2014) (Cited on page 105).

[149] A. Sinha, D. W. Hess, and C. L. Henderson, "Area-Selective ALD of Titanium Dioxide Using Lithographically Defined Poly(methyl methacrylate) Films", J. Electrochem. Soc. **153**, G465–G469 (2006) (Cited on page 105).

[150] E. Färm, M. Kemell, M. Ritala, and M. Leskelä, "Selective-Area Atomic Layer Deposition Using Poly(methyl methacrylate) Films as Mask Layers", J. Phys. Chem. C **112**, 15791–15795 (2008) (Cited on page 105).

[151] A. S. Quick, A. de los Santos Pereira, M. Bruns, T. Bückmann, C. Rodriguez-Emmenegger, M. Wegener, and C. Barner-Kowollik, "Rapid Thiol-Yne-Mediated Fabrication and Dual Postfunctionalization of Micro-Resolved 3D Mesostructures", Adv. Funct. Mater. **25**, 3735–3744 (2015) (Cited on page 106).

[152] J. E. Mahan, *Physical Vapor Deposition of Thin Films* (John Wiley & Sons, New York, 2000) (Cited on page 107).

[153] D. M. Mattox, *Handbook of Physical Vapor Deposition (PVD) Processing* (William Andrew, Norwich, 2010) (Cited on page 107).

[154] R. Ghodssi and P. Lin, eds., *MEMS Materials and Processes Handbook*, Vol. 1 (Springer, New York, 2011) (Cited on page 107).

[155] G. J. Dolan, "Offset masks for lift-off photoprocessing", Appl. Phys. Lett. **31**, 337–339 (1977) (Cited on page 107).

[156] J.-J. Chen, S. Jang, T. Anderson, F. Ren, Y. Li, H.-S. Kim, B. Gila, D. Norton, and S. Pearton, "Low specific contact resistance Ti/Au contacts on ZnO", Appl. Phys. Lett. **88**, 122107 (2006) (Cited on page 107).

[157] L. J. Brillson and Y. Lu, "ZnO Schottky barriers and Ohmic contacts", J. Appl. Phys. **109**, 8 (2011) (Cited on page 107).

[158] *Thin Film Evaporation Guide, 2017 Revision* (Vacuum Engineering & Materials (VEM), 2017) (Cited on page 108).

[159] C. Kern and M. Wegener, "Three-dimensional metamaterial Hall-bar devices", Phys. Rev. Mater. **3**, 015204 (2019) (Cited on pages 116, 128, 130, 132, 135–140).

[160] V. Schuster, "Experimente an Metamaterialien mit Parallelem Hall-effekt", Master's Thesis (Institute of Applied Physics, Karlsruhe Institute of Technology, 2016) (Cited on page 122).

[161] M. J. Biercuk, D. J. Monsma, C. M. Marcus, J. S. Becker, and R. G. Gordon, "Low-temperature atomic-layer-deposition lift-off method for microelectronic and nanoelectronic applications", Appl. Phys. Lett. **83**, 2405–2407 (2003) (Cited on page 129).

[162] A. Quick, private communication, 2018 (Cited on page 132).

Acknowledgments

It is a great pleasure to express my gratitude to all of those without whom this work would not have been possible.

First and most of all, I would like to thank Prof. Dr. Martin Wegener for the opportunity to work on this exciting and challenging topic. I am very thankful for his guidance and support throughout my time in his group. Next, I would like to thank Prof. Dr. Jörg Schmalian, who kindly agreed to act as a second reviewer.

I am immensely grateful to Prof. Dr. Graeme Milton, with whom I had the opportunity to explore the underlying theory of Hall metamaterials. Prof. Dr. Muamer Kadic is gratefully acknowledged for many fruitful discussions. His exhaustive expertise on numerical calculations and the software package COMSOL has been very helpful.

I am very much indebted to Andreas Wickberg, with whom I shared countless hours working on the atomic-layer deposition setup. Martin Schumann, Andreas Wickberg, Tobias Frenzel, and Vincent Hahn are gratefully acknowledged for taking the scanning electron micrographs of my samples. Furthermore, I would like to thank Jurana Hetterich and Adrian Mertens for their assistance with the ellipsometry measurements.

I am thankful that I had the opportunity to supervise the bachelor's thesis of Jessica Meier and the master's theses of Vittoria Schuster and Julian Köpfler. I have very much enjoyed our joint research.

Furthermore, my thanks go to my collaborators, with whom I shared the pleasure of working on a number of projects that are not part of this thesis, namely to Wadood Haq, Zheqin Dong, Larissa Kohler, Kevin Edelmann, and Vibhuti Rai.

Moreover, I am thankful to all former and present members of our group, who have created a very productive and enjoyable atmosphere. Spending time with them has been a lot of fun.

I would also like to thank all of those who have worked in the background. I am very grateful to our technician, Johann Westhauser, and to Michael Hippe, Helmut Lay, and Werner Gilde from the electronics workshop. Frank Landhäuser and the whole staff of the mechanical workshop are acknowledged for their brilliant work and support. Furthermore, the secretaries Ursula Mösle, Claudia Alaya, and Monika Brenkmann are thanked for their administrative support.

Finally, I would like to thank Maja Capek, Tobias Frenzel, Annemarie Huschitt, Julian Köpfler, Frederik Mayer, Jessica Meier, Alexander Münchinger, and Alfred Seiler for proof-reading this thesis.